University of Sydney
&
University of Venice

Cotutelle

Doctoral Thesis

Phase-behaviour of Janus Dumbbell Liquids and Assemblies by Monte Carlo Techniques

Author:
Patrick Ignatius O'Toole

Supervisors:
Dr. Toby Hudson
Prof. Achille Giacometti

A thesis submitted in fulfilment of the requirements
for the degree of Doctor of Philosophy

in the

Theory Group
School of Chemistry
&
Soft Matter Group
Department of Molecular Sciences and Nanosystems

March 2016

Declaration of Authorship

I, Patrick Ignatius O'TOOLE, declare that this thesis titled, 'Phase-behaviour of Janus Dumbbell Liquids and Assemblies by Monte Carlo Techniques' and the work presented in it are my own. I confirm that:

- This work was done wholly or mainly while in candidature for a research degree at this University.
- Where any part of this thesis has previously been submitted for a degree or any other qualification at this University or any other institution, this has been clearly stated.
- Where I have consulted the published work of others, this is always clearly attributed.
- Where I have quoted from the work of others, the source is always given. With the exception of such quotations, this thesis is entirely my own work, except where stated.
- I have acknowledged all main sources of help.
- Where the thesis is based on work done by myself jointly with others, I have made clear exactly what was done by others and what I have contributed myself.

Signed:

Date:

“Whereof one can not speak, thereof one must be silent.”

Ludwig Wittgenstein

UNIVERSITY OF SYDNEY
&
UNIVERSITY OF VENICE

Abstract

Faculty of Science
School of Chemistry
&
Department of Molecular Sciences and Nanosystems

Doctor of Philosophy

Phase-behaviour of Janus Dumbbell Liquids and Assemblies by Monte Carlo Techniques

by Patrick Ignatius O'Toole

This thesis summarises a theoretical investigation into the phase behaviour of model 'Janus' dumbbell systems composed of two tangent spherical sub-particles, one possessing a hard-sphere potential and the other a square-well potential. The relationship between shape and interaction anisotropy is explored via varying the particle properties over two orthogonal pathways from reference systems to the target system to elucidate the effects of increasing particle interaction and shape anisotropy on the fluid properties at a range of state-points. Three different simulation techniques are employed to variously study the gas-liquid properties, self-assembled structures, and compression behaviour. The reference systems involved are the hard-sphere model, the square-well model, and the square-well dumbbell, each forming an extremum of the parameter space. A parameter, α is developed to control the size ratio between the interaction sites. The parameterisation developed herein allows the particles to be tuned over the full range of diameter ratios to explore from a pure hard-sphere system at $\alpha = 0$, to a pure square-well system at $\alpha = 2$, with the region between $0 < \alpha < 2$ characterising the heterogeneous Janus dumbbell. Variegated phase behaviour is observed over the range of α. Gas-liquid critical phenomena is observed, in general, for the more isotropic particle descriptions where the particle possesses an attractive portion. As the interaction profile becomes more anisotropic the system properties change drastically. Phase diagrams are computed via collation of gas-liquid phase separation data, calculated via Successive Umbrella Sampling with histogram re-weighting, along with Simulated Annealing simulations in the Canonical ensemble, both of which employ an implementation of the Aggregation-Volume-Bias Monte Carlo intra-box swap move algorithm. The development of self-assembled phases that perturb gas-liquid critical phenomena is observed until the critical point becomes metastable with respect to the formation of bilayer structures where the diameter of the purely repulsive interaction site is similar to the attractive site. Bilayer structures in this region are observed to tolerate significant curvature until the two interaction sites are equal in size ($\alpha = 1$). In the intervening regime ($1 < \alpha < 1.3$) several topologically different structures are observed including: vesicles, tubes, gyroids and other bi-continuous structures. Where the diameters are equal only micelles are observed at low density which eventually form lamellar sheets at higher densities. Where the attractive site is smaller than the repulsive site, the systems are observed to display up to seven structurally differentiable behaviours controlled by α and the state-point, including: a monomer gas, micelles, platelets, strips, strip networks, sponges, and lamellar structures. The location of these structures is identified on phase diagrams at each α studied.

Acknowledgements

Firstly, I would like to thank my parents, Susan and Brian, my brothers and sisters, Lilly, Jimmy, Andy, and Jules, whose unquestioning support and encouragement throughout my career as a student are the main reason I am here. Secondly, I would like to thank my dear friends and contemporaries Emily, Mitchell, and Stephen for companionship, advice, and coffee breaks over the past four years, though we are now all in different places I'm sure we will be lifelong friends. Thirdly I would like to thank the other transient inhabitants of both room 209C and my office in Venice for random musings and putting up with me on a day to day basis. Fourthly I would like to thank the Australian Government Department of Education and Training and The Co-operlink Grant Scheme between Australia and Italy for all of the funding each of those sources has provided such that I may pursue my interests in regards to the subject matter contained in this document, as well as providing the means for me to live in Venice sporadically over the past four years. I would also like to thank the University of Sydney and the University of Venice Ca' Foscari for accepting me into a PhD program and providing the resources required of this kind of endeavour. I would also like to thank Professor Peter Harrowell for granting me access to the idiosyncratic computer cluster Silica, as well as providing a source of statistical physics humour, on his transient visits to room 209C. Lastly I save my deepest thanks for my supervisory team, Dr Toby Hudson and Professor Achille Giacometti, for all their support, suggestions, insight, and reviews of the manuscript fragments that eventually lead to the formation of this document.

Contents

List of Figures

List of Tables

Symbols

σ	characteristic length	dimensionless
ε	characteristic energy	dimensionless
λ	interaction range	dimensionless
ω	angular frequency	rads^{-1}

Chapter 1

Introduction

A central challenge involved in the modelling of complex matter is that of generating simple models that capture the observed behaviours of a target system. This often proceeds by one of two very different methodologies. One is to concieve a model of a particular system as accurately as possible and iteratively remove degrees of freedom in order to see which minimal combination yields a sufficient description of the system properties. The other method is to build from basic notions of particle interactions and *add* complexity, in the hope that eventually the model returns such complex behaviour. This thesis catalogues an investigation in the latter style, and attempts to arrive at general principles applicable to particle systems across the meso-scopic lengthscales for the targeted class of particle.

1.1 Meso-scale Materials and "Bottom-up" Synthesis

Particles with sub-micron ($< 10^{-6}\ m$ or $1\ \mu m$) primary length scale demonstrate exotic material properties. These phenomena render the meso-scopic length scales a fecund and yet largely unexplored realm. Reliably organising matter at these scales presents a formidable challenge to science. Photo-lithography is heretofore the most employed method for micro-fabrication of patterning for application in small scale electromechanical systems. Photo-lithographic eximer processes rely on ultraviolet (UV) radiation on the order of 2×10^{-7} m, restricting the minimum critical dimension to approximately 50 nm. In the future developing materials that traverse these length scales will not be performed by means of a 'top-down' approach. Considerable attention has been paid to the study of 'bottom-up' approaches to material manufacture. These 'bottom-up' approaches rely upon the phenomenon of self-assembly[1]. Self-assembly can be described

---

[1] Known in antiquity as *soft*-lithography [2].

as the autonomous organisation of particulate matter into patterns or structures [3]. Matter displays varied self-assembly phenomena across many length-scales. Our species is only now learning how to exploit these phenomena to incorporate materials organised via this route into functional materials.

1.2 Wrangling the Parameter Space and Cataloguing

The set of investigations studied here explores the relationship between interaction anisotropy and particle geometry, and attempts to arrive at generally applicable design principles for aggregated structures with targeted geometric properties. The development of general design principles facilitates the material scientist, chemist, or engineer with a catalogue of structures with which to compose some functional material. Control over adduct aggregation — understanding the thermodynamic and kinetic factors involved in driving a system to a particular state — is crucial. The study of materials has historically relied upon serendipity as a driver of discovery, but much less of explanation. An engineer who wishes to design a new material, for example a surface with special properties, must develop her design with the materials available. A newly developing field of innovative research is nano-particle (NP) design. The authors of [4] identify (at least) eight different "anisotropy dimensions" for colloidal particulate matter. This combinatorial anisotropy space includes: interaction surface coverage or patchiness; aspect ratio; faceting; pattern quantisation; branching; chemical ordering; shape gradient; and surface roughness. Given this large space of anisotropy dimensions, the concept of a library that catalogues the space of NPs according not only to their individual properties but also the properties of their assemblies appears desirable. Filling out the annexes of a structural library[2] that catalogues the phase space of NP aggregates is imperative to the future of materials research, not least if humans are to incorporate design elements into small-scale functional architecture development. In the future it may be possible through the use of such libraries to employ an artificial intelligence to compose new materials without the need for costly and wasteful experimentation. For a library of this type to function it must not only categorise the structural diversity of particles and their assemblies, but also contain maps for synthetic routes to obtain both the NP and its assemblies. The current work is concerned with combining some aspects of the anisotropy space: patchiness and shape gradient (and incidently aspect ratio). This is achieved by considering amphiphiles composed of two separate interaction sites.

---

[2] These exist already for crystal structures composed of atomic building blocks: International Crystal Structure Database (ICSD); Cambridge Crystallographic Data Centre (CCDC) and the Cambridge Structural Database (CSD); American Mineralogist Crystal Structure Database (AMCSD); Crystallographic and Crystallochemical Database for Minerals and their Structural Analogues (CCDMSA); For synthetic stategies and structure-property relationships one must be a little more assiduous in tracking them down, however.

1.3 Amphiphiles

We consider an amphiphile as a particle which possesses two regions of differing *philos*. This is by no means a meaningless distinction, since the origin of such properties will influence the behaviour of a system composed of them based on their interaction profiles. Nature makes vast use of the behaviours of amphiphilic materials and achieves great control over aggregate structure and bulk phase behaviour. When performed by humans, even in the simplest experiments, influencing self-organisation can be tricky — balancing subtle differences in enthalpic and entropic factors driving aggregation between competing structures can often lead to undesired outcomes. Understanding the properties of amphiphiles, particles[3] with some inherent duality in their interaction profile, has attracted much attention in the past few decades in an effort to understand their function in biological systems, exploit their peculiar properties in bio-molecular theraputics [5, 6], and — at least for colloids — realise their potential for application in magnetic [7–10], opto-electronic [11–13], catalytic, and multi-functional [14] technologies. Due in part to this interaction duality, amphiphiles tend to exhibit interesting assembly properties at interfaces, giving rise to the moniker *surfactant* — ***surf**ace-**act**ive-**a**ge**nt***. This ability to be at once soluble in immiscible fluids offers an interesting avenue for controlling the orientation of particles and the topology of an interface [15]. Control of interfacial topology is of utmost importance in biological systems, where the function of membrane surface proteins depends sensitively on their orientation and interactions with the intra-membrane hydrophobic layer, and its interaction with the folded protein's properties. Folding processes of linear peptide chains has been observed to depend strongly on contributions to their structural properties from collecting hydrophobic residues together to lower their interfacial energy with intra-cellular media [16]. The function of enzyme active sites often proceeds via precise selective localisation of chemical species, controlled sensitively by intercalation of specific spatial arrangements of hydrophobic residues to bind reactant ligands. While nature makes such vast, varied, and precise use of amphiphiles in biological systems, our understanding of the interplay between kinetic and thermodynamic control factors is lacking. In spite of this general lack of comprehensive understanding, strong theoretical foundations for the thermodynamics of amphiphile aggregation and self-assembly properties has been the focus of much scientific study[4].

---

[3] Including molecular species, polymeric colloids, and micro- and nano- colloidal systems.

[4] Even in antiquity the behaviour of oils dispersed on water, recorded in cuneiform on stone tablets recovered from 18th centrury BCE Babylonia digs, soothsaying rituals involving the strange figures appearing in oil films dispersed on water would belie omens of varying fortune. One primordial, yet more scientific, experiment performed by Benjamin Franklin on a pond in Clapham Commons, dispersing a small measure of olive oil on the pond, allowed him to calculate the approximate thickness of the layer formed, where also he noticed it had a 'calming' effect on the surface.

1.4 Early Thermodynamics of Amphiphiles

Early studies of the thermodynamics of amphiphile self-assembly focus on packing as strongly determinant of structure [17]. Delicate analysis of particle shape and interaction properties lead to strongly predictive theoretical models for the internal structure of aggregates and their surface morphologies. For the most part these early studies consider the amphiphile as possessing flexible internal degrees of freedom: a somewhat rigid hydrophilic head-group, and a flexible hydrophobic chain. The model developed in [17] employs a dimensionless 'packing-parameter', $v/a_0 l$. Here v is the volume of the amphiphile, a_0 is the equilibrium head group surface area given the surface topology (held constant, which places a limitation on the modelling of certain interfacial topologies), and l the hydrophobe chain length[5], and an elaboration on the packing behaviour can be found in Chapter 6.

Here it is poignant to delineate the water soluble "hydrophile" and sparingly water soluble "hydrophobe" portions as simply *solvophile* and *solvophobe* so as not to vex the reader with a litany of questions about what solvent is to be considered as the bulk and what co-solvent, if indeed there is one, is to be considered as the minor fraction. This is of course not a trivial distinction to make, not least of importance with the flexibility of constituent solvphilic or solvophobic moieties, the choice of solvent(s). Of course, the origin of any solvophilicity is important in studying any particular system, yet complicates matters by adding additional parameters to be rationalised and optimised. In the case of amphiphiles with internal degrees of freedom assembly proceeds by partitioning of the solvophobic regions together to minimise the surface area interacting with the solvent. In biological systems, delicate control over the composition of the solvophobe chains and solvophile head groups influences the aggregation behaviour which can lead to microsegregation of particular species of amphiphiles [18]. This property, of great importance to the function of trans-membrane protein complexes [19], implies a strong size-shape relationship controlling the dynamics of amphiphile aggregation.

1.5 Janus Particles

In a somewhat trite rhetorical mode of adding metaphor to the physics of interaction anisotropic colloidal particles, yet in another way a very appropriate moniker — the Roman god of transition, facing both toward the past and the future, his facets adorning doorways and thresholds in ancient Rome — a class of particle called the *Janus* particle forms the primordial basis for the study of patchiness across many length scales.

---

[5] There is an obvious parallel to be draw between the packing parameter and the parameterisation of the sphere sizes developed in this work, a "dictionary" can be found in **??**.

First appearing to term amphiphile glass beads [20], the term has since found liberal application to particles with various modes of interaction anisotropy. A Janus particle is one that possesses a patch. The boundary of this patch delineates two regions over which the particle possesses different interaction profiles. If this class of particle are to be used as building blocks for meso-scale technologies, or at larger scales as interface stabilising agents as in a Pickering emulsion, controlling the particle properties of the shape-interaction profile is important [21]. Synthetic approaches to study this type of particle have been developed over the past three decades and can be applied to synthesise particles anywhere from μm to nm range [22, 23]. Spherical Janus particles have been the subject of intense scrutiny via experiment [21, 24–28] and via simulation and theory [29–35]. When modelling this type of particle the type of interaction is often neglected, so as to be general and concentrate on the geometry of aggregates and the overall phase scenario. The patches treated as ‘sticky’ and ‘hard’ — or more specifically, with an attractive patch and a non-attractive one. Single patch Janus particles possess several interesting phase scenarios. The authors of [35] compute the gas-liquid phase diagram of one-patch Janus spheres varying the patch size (where χ describes the surface coverage fraction as defined by the Kern-Frenkel model [36]) on the interval $\chi \in [0.5, 1.0]$ — to find that increasing the patch size to 50% coverage (referred to as the Janus limit) leads to an anomalous ‘re-entrant’ gas in the gas-liquid binodal. Due to the presence of highly stable micelle and vesicle formation comprised of specific numbers of particles in the low temperature gas, the coexistence region under the gas-liquid critical point is squeezed, leading to a dense gas of weakly interacting micelles and vesicles coexisting with liquid [32]. This intriguing behaviour leads to a negative slope of the gas-liquid coexistence curve in the pressure-temperature plane, a phenomenon more familiar with coexisting solid and liquid water. This kind of directionally specific interaction is clearly strongly determinant of interesting—potentially useful—material properties. Indeed, Pierre de Gennes in his Nobel Prize acceptance speech entitled ‘Soft Matter’ mused upon what size exclusion effects the hard-core of a Janus particle might have on the phase behaviour [37][6].

We develop this literature by including an aspect of shape anisotropy to the existing framework to explore the structural diversity brought by separating the interaction sites onto two different loci. This class of particle has been studied fairly extensively in experiment [15, 21, 23, 38–52] and by theoretical methods [53]. Simulation work on this sub-class of dumbbell shaped Janus particle have taken different routes [54, 55]. Early work in which the authors referred to the particles as ‘peanut-shaped’ nano-particles [54], in which Virtual Move Monte Carlo (VMMC) — a method to approximate the dynamical evolution of particle systems according to potential energy gradients [56] —

---

[6] identifying that ‘leaky’ membranes may find useful technological application.

simulations are performed to investigate self-assembled structures formed in the 'peanut-space', where both the inter-nuclear distance is varied and the relative size of the lobes. Kinetic phase diagrams demonstrate the presence of both simple structures rationable via simple packing arguments, and complex hierarchical self-assembly pathways to a range of different structures, including spherical and non-spherical micellar aggregates, bilayers, faceted polyhedra, and crystalline clusters.

More recent work on the self-assembly products performed long Vanilla Monte Carlo[7] (VMC) simulations employing the Kern-Frenkel potential, with long simulations lengths (approximately 70 million MC cycles) at interaction strengths of $\beta\epsilon = -3.58$, which the authors argue is sufficient to observe self-assembly [55, 57]. The authors investigate the effect of the sphere separation, parametrised as $l = 2d(\sigma_s + \sigma_h)$, where σ_s and σ_h are the diameters of square-well (SW) and hard-sphere (HS) lobes, on the structure of aggregates with sphere size ratio $q = \sigma_h/\sigma_s$ at system volume fractions below $\phi < 0.20$ over $0.95 \leqslant q \leqslant 1.25$.

Where $q = 0.95$, the SW lobe is larger than the HS, on varying l from near zero to 0.5, isotropic liquid droplets, followed by bilayers form which at $l \gtrsim 0.3$ and low density can curl to form vesicle structures. For $q = 1.035$, upon increasing l from near zero to 0.50, where the the particle is more recognisable as a dumbbell shape, the system undergoes structuring from spherical micelles at $l \approx 0.05$, which elongate between $0.05 < l < 0.2$, form vesicles where $l \approx 0.2$ and finally form bilayers for $l > 0.2$. Where the hard sphere portion is larger, where $q = 1.25$, where the HS lobe nearly eclipses the whole square-well, such that the "dumbbell" resembles a one patch sphere (with a small attractive lump), while spherical and elongated micelles are observed, the formation of vesicles does not occur.

Thermodynamic calculations that focus on the equilibrium orientation of amphiphile particles at an interface identify that aspect ratio and surface wetability play an important role, with small aspect ratios and large wetability gradients favouring perpendicular orientations of the long axis to an oil-water interface [15], a result familiar to conventional amphiphile research. In the study of a related system, prolate ellipsoidal amphiphiles adsorbed on curved oil-water interfacial topologies studied via dissipative particle dynamics [58], indicates that liquid-crystalline ordering of the adsorbed particles with varying surface coverage depends upon the patch size and the aspect ratio.

These findings indicate that as the patch approaches a coverage factor $\chi \approx 0.5$ that the formation of layered structures dominates, and that the site separation or aspect ratio, has a strong influence on the topology of structures that form. This is an important

---

[7] The term *vanilla* is used here to distinguish Monte Carlo employing conventional roto-translation moves from more *exotic* move algorithms.

point: the geometry of aggregate structures composed of Janus type colloids depends sensitively on the surface coverage of the different interaction profiles, the distance between the two *philos*, and the packing constraints imposed by the excluded volume of the particle core.

An attempt to address three issues follows. Firstly, we begin with a dumbbell shaped particle, defined by two tangent spheres of equal diameter, each surrounded by a SW potential. We then *tune* the strength of the interaction on one site until only the bare repulsive core remains. This final configuration we refer to as the Janus limit for tangent dumbbells. In the case of spherical particles varying patch coverage drastically alters the phase behaviour (see, for example [35]). The variation in the relative interaction strength is analogous to this. Along the site interaction coordinate we analyse the variation in gas-liquid critical phenomena and compute phase diagrams cataloguing the system behaviour, and where appropriate describe the microscopic structure of the fluid and any assemblies encountered. This is addressed in Chapter 4. From this point (the Janus limit) we employ a size ratio parameter to account for the difference in diameter between the two (still tangent sphere) interaction sites, which we refer to as the heterogeneous Janus dumbbell. We start at the maximum of the size ratio parameter and explore the fluid phase behaviour. We compute gas-liquid phase separation binodals where liquid critical phenomena occurs and estimate critical points, and identify regions where gas-liquid critical behaviour is no longer observed. This analysis is discussed in Chapter 5. Where the structure of condensates varies from that of typical isotropic liquids we categorise and attempt to rationalise their structure. This analysis is performed in Chapter 6. Finally, in Chapter 7 we present phase diagrams summarising the findings of the previous two chapters.

Chapter 2

Modelling

This chapter shall discuss the specific rules that the investigation follows, outline the rationale for particular choices made in parameterisation of the target systems, and develop some methods for addressing the questions outlined at the end of Chapter 1. We extend a model of particle interactions and rules of 'motion' to describe the thermodynamic properties of particle systems. To this end we invoke a conception of statistical mechanics such that a finite system can be explored at some constant set of macro-parameters to obtain bulk properties and observables in the thermodynamic limit. In order to apply this methodology we express the problem in the language of classical statistical thermodynamics, but before we do this we need to describe a microscopic depiction of particle interactions, the particle geometry, and interaction parameters such that we can traverse the parameter space(s) systematically.

2.1 Defining the System

2.1.1 Parameterisation

Since we are trying to understand the phase behaviour of Janus dumbbells, we define a set of parameters that account for both the characteristic system properties, as well as the size ratio of our particles and the interaction properties located on each sphere. To do this we first introduce the dimensionless characteristic system parameters.

Reduced Units

Before describing the particles in detail we first describe two fundamental quantities, using which we define all other properties of the system. Properties defined in terms of these parameters are described as *reduced* and avoid the potential embarrassment of running essentially duplicate calculations on particle systems that can be described similarly by folding in factors proportional to these quantities specific to each system. The first is the characteristic length scale parameter σ. All lengths are expressed in terms of this characteristic length parameter and it is set to unit value. The second is the characteristic energy scale parameter, ε, also set to unit value. Using these reducing parameters we can write down a set of reduced units, for example the density, temperature, energy and pressure can all be re-expressed in term of these:

$$\boldsymbol{\rho}^* = \rho\sigma^3, \qquad \mathbf{T}^* = k_B T/\varepsilon, \qquad \mathbf{E}^* = \mathrm{E}/\varepsilon, \qquad \mathbf{p}^* = \mathbf{p}\sigma^3/\varepsilon \tag{2.1}$$

A Janus dumbbell (JD) is here defined as composed of two tangent spherical sub-particles: one h sub-particle possessing a hard-sphere (HS) interaction, and another s sub-particle containing a square-well (SW) interaction. The full potential between particles i and j, V is defined as

$$V(r_{ij}) \equiv V_{SW}(r_{ss}) + V_{HS}(r_{hh}) + V_{HS}(r_{sh}) + V_{HS}(r_{hs}). \tag{2.2}$$

where the potential is defined over each pair of sites on each particle such that

$$V_s(r_{ss}) \begin{cases} \infty & r_{ss} < \sigma_s \\ -\varepsilon & \sigma_s \leqslant r_{ss} \leqslant \sigma_s + \lambda\sigma_s \\ 0 & r_{ss} > \sigma_s + \lambda\sigma_s \end{cases}, \qquad V_h(r_{ab}) = \begin{cases} \infty & r_{ab} < (\sigma_a + \sigma_b)/2 \\ 0 & r_{ab} > (\sigma_a + \sigma_b)/2 \end{cases}. \tag{2.3}$$

where interaction sites a, $b \in \{s, h\}$, along with the corresponding particle diameters. The particles therefore most simply, where $\sigma_s = \sigma_h$, take the form denoted in panel d) of Figure 2.1.

2.1.2 Pathways

There are in principle an infinite number of ways of transforming particles, however circuitous the route may be. In practice one is limited by the mathematical tools for performing the transformation and imagination. Bearing in mind that one also must consider the practicality of the transformation. Defining quantities in terms of a set of fundamental reduced quantities also facilitates the comparison of metrics across the range of parametrisation. The first such quantity is the size asymmetry parameter.

2.1.3 Size Asymmetry - α

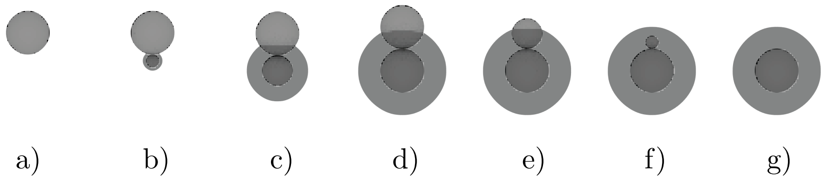

FIGURE 2.1: Sketch of the particle at different points in the α space: a) pure HS; b) $\alpha = 0.25$, such that $\sigma_h = 1$ and $\sigma_s = 0.25$; c) $\alpha = 2/3$; d) the Janus dumbbell where $\alpha = 1.0$; e) $\alpha = 4/3$, where $\sigma_s = 1$ and $\sigma_h = 2/3$; f) $\alpha = 7/4$, where $\sigma_s = 1$ and $\sigma_h = 1/4$; g) pure SW. The shaded regions denote the range of the interaction of each s sub-particle.

Since we would like to model systems of particles composed of tangent-sphere dumbbells we define two diameters, σ_s and σ_h that account for the size of each sphere. These are defined in terms of the characteristic length and a size ratio parameter. In order to account for the diameter ratio between each of the constituent spheres of a dumbbell we define a parameter $\alpha \in [0, 2]$, that modifies the sphere diameters σ_s and σ_h such that

$$\sigma_s = \begin{cases} \alpha\sigma & \alpha \leqslant 1 \\ \sigma & \alpha \geqslant 1 \end{cases}, \qquad \sigma_h = \begin{cases} \sigma & \alpha \leqslant 1 \\ (2-\alpha)\sigma & \alpha \geqslant 1 \end{cases}. \tag{2.4}$$

It should be fairly obvious that this particular formulation avoids the problem of a divergent sphere diameter[1], were one to take a simple diameter ratio as in some the literature [54, 55] which study essentially similar systems are wont to do. Defining the particle diameter ratio in this way also allows smooth deformation of the particle across the parameter space such that at each extreme the model returns the behaviour of a system of particles of diameter σ, but with the properties of the potential defined on that sphere.

---

[1] A serious problem for simulation, where numerical quantities are maintained close to unit value to mitigate the problem of machine representation: overflow and underflow, and floating point precision. Not to mention the volume of the box of an extremely large sphere in a box of size length $\mathbf{L} \propto \sigma_{Large}$, yielding all sorts of problems for comparing similar states across ensembles.

2.2 Reference Systems

Given that the target particle systems incorporate not just size asymmetry but also interaction anisotropy we are left with a choice of what kind of interaction we wish to place on each sphere. The approach outlined here is a distinctly different and simpler approach to that of Janus spheres and other Janus type dumbbells which employ the Kern-Frenkel model [29, 30, 32, 35, 36, 55, 59]. While there is a veritable zoo of interaction potentials, ranging from the what can be best described as *primitive* to what can be best described as *approximate*, we settle on a primitive choice. Due to the large swathes of parameter space to traverse ideally one would choose as simple, or cheap to compute, a potential as possible, yet the lack of solid justification for *just any* interaction model still warrants a brief discussion of the particular choice settled upon.

2.2.1 Approximate (primitive) potentials

Hard-sphere

The hard-sphere (HS) potential forms the basis of the aptly named *hard-core* thermodynamics. For pure systems it is a single parameter system, the particle diameter σ, in reduced units parameter free. A surprising result from early statistical physics simulations of this most rudimentary particle model — the pure hard-sphere — was that its phase behaviour included a phase transition between a continuously deformable fluid to a crystal structure via a first-order process [60]. This was a sort of proof of concept that demonstrated how only rather simple conceptions of particle interactions are required to mimic what was thought to be as complex a processes as a phase transition, and in this case that only a hard-core was required to stabilise a crystal. Crystallisation of hard-spheres is a purely entropy driven process. The structure which forms at low system density is one which maximises the *free-volume* around each particle. For mono-disperse spheres a maximum packing fraction of $\pi/3\sqrt{2} \approx 0.74048$ is achieved by both *face-centred cubic* (FCC), or *hexagonal close-packed* (HCP) structures. The global thermodynamic minimum is achieved by the FCC structure, but only by a very slim margin [61]. At lower densities, it is possible to form a *jammed* structure analogous to a glass [62], though the process by which this occurs, and the nature of the transition is still an open problem.

Since we are not specifically interested in crystal formation in the present study, the HS potential offers us little in the way of reference, having no source of interaction it can not display any gas-liquid phase separation behaviour or low density assembly properties and can be treated as a special, but ultimately useless, extremum of the parameter space.

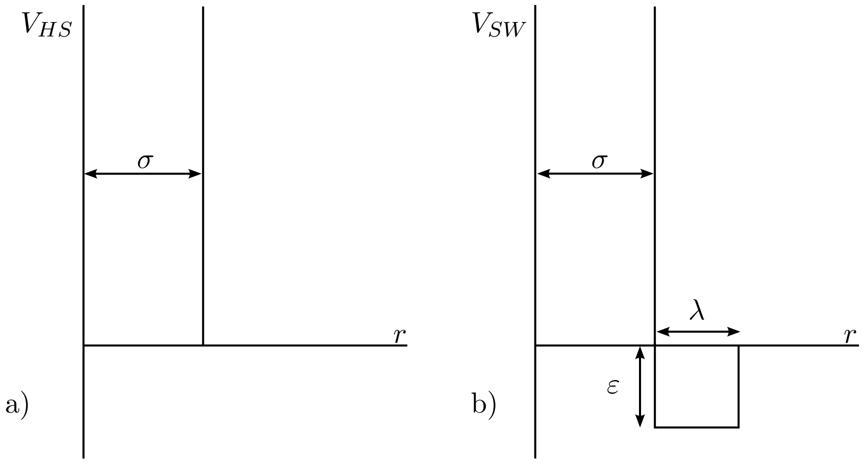

Figure 2.2: Sketch of the a) HS and b) square well potentials demonstrating the parameter make-up of each.

Square-well

At the other end of the α parameter space the model returns a sphero-symmetric surrounded by a square-well SW potential. The SW potential is the simplest to incorporate a form of attraction. In spite of its simplicity, like the hard sphere, is able to demonstrate remarkably diverse phase-behaviour. It is the simplest model to display all of the properties of classical matter, *i.e.* a crystallisation on cooling, and a gas-liquid phase separation at sufficiently high temperature. The primitive square-well potential is therefore probably most readily conceived as a first-order approximation to a van der Waals interaction and is a simple addition to the hard-core model: a well of finite length, λ, with a depth, ε. In general it is a three parameter system: σ, λ, and ϵ; and for pure systems in reduced units it has only a single parameter, the interaction range, denoted here as λ, the others: ε and σ can be factored out simply.

2.2.2 Interaction Range - $\boldsymbol{\lambda}$

The dependence of the gas-fluid phase-separation behaviour of a system comprised of particles interacting via the SW potential is well-studied in the literature. An erudite discussion of the gas-liquid phase diagrams can be found in [1, 63–65]. Here are collected a brief recollection of the findings from [1], restricted to those within the purview of the current study, see Figure 2.3. Where the interaction range is large ($\lambda = 1.0$) the bonding interaction tolerates large interparticle separation leading to a comparatively high temperature gas-liquid binodal which is narrow and eccentric, rationable via a mean-field style theories. In contrast, for short interaction ranges ($\lambda < 0.25$) the gas-liquid critical point becomes meta-stable with respect to the formation of a crystal. It

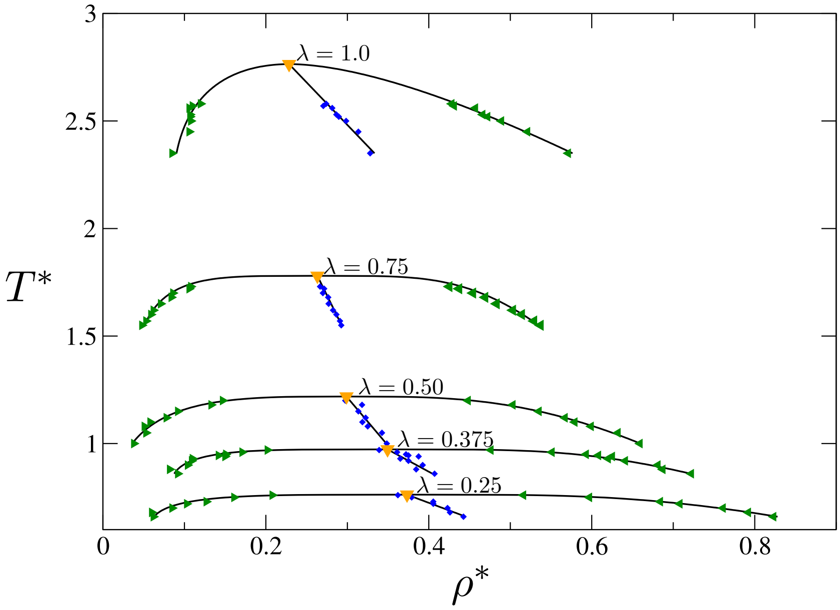

FIGURE 2.3: Binodal gas-liquid coexistence curves as obtained by Gibbs Ensemble simulations of the SW fluid with variable interaction range. Fitting was performed using Equation 5.4 and Equation 5.4. On reducing λ the liquid density branch shoots off to increasingly higher densities where $T^* < T_c^*(\lambda)$.

is clear that theoretical studies of particle systems incorporating SW potentials ought to tread the intermediate λ to avoid these two undesirable extrema.

2.2.3 Choosing λ

In order to reduce the parameter space to traverse, we have chosen the interaction range $\lambda = 0.5$. This is somewhat hard to justify. The van der Waals interaction, to which the SW potential conceivably comprises a first-order approximation, at molecular scales is on the order of the Bohr radius of atomic species. Where particle length-scales are larger, say for colloidal systems (between nm and μm) interaction ranges can vary between 100 % and 0.1 % as a proportion the particle size, depending upon the origin of the interaction. Given that we wish to capture behaviour at meso-scopic length-scales, an intermediate potential range is employed. In theoretical terms, as identified in Section 2.2.2, we identify that for the SW potential the interaction range where conventional gas-liquid phase separation is observed lies in the interaction range $\lambda \in [0.25, 1.0]$. Where $\lambda \approx \sigma$, the behaviour of the square-well fluid can be modelled by a mean field approximation, on decreasing λ, a region of conventional gas-liquid phase separation is returned by the model until the critical point becomes meta-stable for $\lambda < 0.25$. Given these considerations, the interaction range of $\lambda = 0.5$, should give us a reasonable "in between" behaviour.

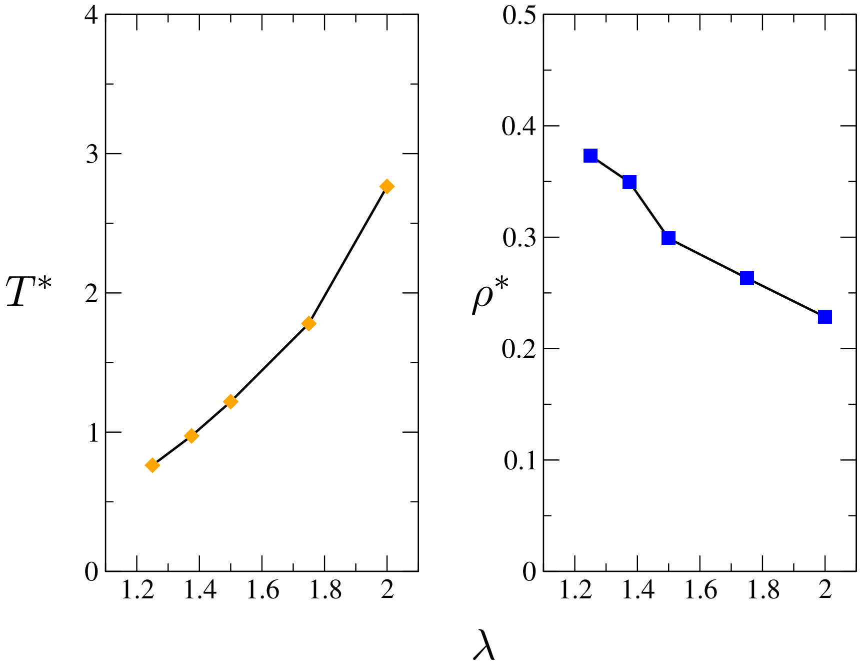

FIGURE 2.4: Binodal gas-liquid coexistence curves as obtained from [1] by Gibbs Ensemble simulation of the variable interaction range λ SW fluid.

2.2.4 Solvent Interaction

In what is likely to be received as a glaring omission from the parameterisation outlined above is the question of solvent. It is clear that for amphiphiles, appropriate solvent-amphiphile interactions are strongly determinant of both the aggregation properties of the amphiphile, as well as the topology of any interface that forms [17]. Here since we wish to reduce our parameter space, it is useful to neglect certain aspects which can be considered indirectly. In this case solvent interactions are treated indirectly via the potential definition such that aggregation is driven by the anisotropic ‘stickiness’ on one end of the particle. It will be demonstrated later that in spite of a lack of even an implicit solvent that the aggregation properties of these model colloid amphiphiles demonstrates a diverse array of phase behaviours determined by the outlined parameterisation.

Chapter 3

Methods

This chapter discusses the Monte Carlo method and the thermodynamic basis upon which the simulation of particle systems is built. We proceed by developing the mathematical machinery that underpins the simulation approach. After defining the form of thermodynamic averages to be calculated we move onto algorithm design and then on to the specific metrics involved in characterising the systems encountered. An implementation of the Aggregation Volume Bias Monte Carlo [66, 67] is implemented, to our knowledge for the first time, on this particular class of particle. The code developed in this work is released under GNU GPLv3 subject to the appropriate citations via GitHub from user name 2mote.

Each configuration of a particle system containing **N** identical particles is assigned a 3**N** dimensional state vector $\vec{\mathbf{r}}_i$, defining a unique point in a configuration space $\mathcal{M}$. We refer to these $\vec{\mathbf{r}}_i$ as microstates. The set $\{\vec{\mathbf{r}}\}$ defines a volume in $\mathcal{M}$. $\mathcal{M}$ describes all of the possible ways of constructing the system. We assign a weight-factor, $\mathbf{W}(\vec{\mathbf{r}}_i)$, to each microstate to quantify the probability of finding the system in a configuration $\vec{\mathbf{r}}_i$ in the chosen ensemble.

The Canonical Ensemble

In the Canonical ensemble, at constant number of particles, N; volume, V; and temperature, T: for the i^{th} microstate, the corresponding weight factor is

$$\mathbf{W}_{NVT}(\vec{\mathbf{r}}_{\mathbf{i}}) = e^{-\beta\mathcal{U}(\vec{\mathbf{r}})}, \tag{3.1}$$

where $\mathcal{U}(\vec{\mathbf{r}})$ is the value of the potential for a given configuration where the state vector, $\vec{\mathbf{r}}$, takes the values of the particle position vectors, $\vec{\mathbf{r}}$, and β is the inverse Boltzmann temperature, $\beta = 1/k_B T$. The corresponding thermodynamic potential is the Helmholtz free energy,

$$\mathcal{A} \equiv \mathcal{U} - T\mathcal{S}, \tag{3.2}$$

where $\mathcal{S}$ is the system entropy.

The Isothermal-Isobaric Ensemble

A related ensemble is the Isobaric-Isothermal ensemble with constant number of particles and temperature, but imposing a pressure, P, and allowing the system volume, V, to fluctuate, the weighting factor is defined as

$$\mathbf{W}_{NPT}(\vec{\mathbf{r}}_{\mathbf{i}}) = e^{-\beta[\mathcal{U}(\vec{\mathbf{r}})+\mathbf{p}V]}, \tag{3.3}$$

which contains a term accounting for the system pressure, $\mathbf{p}$. The corresponding thermodynamic potential, the Gibbs free energy, $\mathcal{G}$, related to the Helmholtz free energy by

$$\mathcal{G} = \mathcal{A} + \mathbf{p}V \tag{3.4}$$

includes a term accounting for the pressure and volume. Given this formulation, the probability of observing the system in a given microstate is the value of that microstate's weight in ratio to the sum total weight of all possible microstates in the ensemble of choice, I.e.

$$\mathbf{P}(\vec{\mathbf{r}}_i) = \frac{\mathbf{W}(\vec{\mathbf{r}}_i)}{\sum_i \mathbf{W}(\vec{\mathbf{r}}_i)}. \tag{3.5}$$

It is useful to reformulate the sum in the denominator of Equation 3.5 in terms of the classical partition function,

$$\mathcal{Z} = \mathbf{c} \iint \mathrm{d}\vec{\mathbf{q}}\mathrm{d}\vec{\mathbf{p}} e^{-\beta\mathcal{H}(\vec{\mathbf{r}},\vec{\mathbf{p}})} \tag{3.6}$$

Where $\mathcal{H}(\vec{\mathbf{r}}, \vec{\mathbf{p}})$ is the system Hamiltonian that expresses the total energy of an isolated system as a sum of kinetic energy, $\mathcal{K}$, as function of momenta, $\vec{\mathbf{p}}$, and potential energy, $\mathcal{V}$, as a function of coordinates, $\vec{\mathbf{r}}$, and $\mathbf{c}$ is a proportionality constant that ensures that the sum over quantum states converges to the classical partition function in the limit $\hbar \rightarrow 0$ [68]. Since $\mathcal{K}$ is a function of only the momenta, its evaluation can be carried out analytically and we can re-express the configurational portion of the partition function, substituting the potential function from Equation 3.1 for the Hamiltonian, yielding for the canonical ensemble

$$\mathcal{Z}_{NVT} = \mathbf{c}_V \int \mathrm{d}\vec{\mathbf{r}} e^{-\beta \mathcal{U}(\vec{\mathbf{r}})}. \tag{3.7}$$

where $\mathbf{c}_V$ is a constant that ensures the partition function is a dimensionless quantity. The Helmholtz free-energy can then be expressed as

$$\mathcal{A} = -k_B T \ln \mathcal{Z}_{NVT} \tag{3.8}$$

Likewise we can do so for the Isobaric-Isothermal ensemble except re-expressing the coordinates, $\vec{\mathbf{r}}$, as *scaled* coordinates $\vec{\mathbf{s}} \in [0,1]$, modified by the length of the container (assuming a cubic volume), $\mathrm{L} = V^{1/3}$,

$$\vec{\mathbf{r}} = \mathrm{L}\vec{\mathbf{s}}, \tag{3.9}$$

utilising Equation 3.3, and using $\ln V$ as the integration variable over the volume [69], the partition function becomes

$$\mathcal{Z}_{NPT} = \mathbf{c}_P \int \mathrm{d}(\ln V) V^{N+1} e^{-\beta \mathbf{p} V} \int \mathrm{d}\vec{\mathbf{s}}\, e^{-\beta \mathcal{U}(\vec{\mathbf{s}};\mathrm{L})}. \tag{3.10}$$

The Gibbs free-energy can then also be re-expressed in terms of the corresponding partition function,

$$\mathcal{G} = -k_B T \ln \mathcal{Z}_{NPT}. \tag{3.11}$$

The space $\mathcal{M}$ can be decomposed into its composite sub-spaces corresponding to different regions of the phase space. For example, a system of atoms interacting through dispersion forces alone can be observed in phase ω. Restricting the evaluation of $\mathcal{Z}$ to only those configurations that contribute to the phase ω, such that

$$\mathcal{Z}_\omega = \int_\omega \mathrm{d}\vec{\mathbf{q}}_\omega\, e^{-\beta \mathcal{U}(\vec{\mathbf{q}})_\omega}. \tag{3.12}$$

Those configurations of non-zero weight factor are of interest since they correspond to ways of constructing the system with non-vanishing weight factor. Minimising the thermodynamic potentials in each of these subspaces allows us to observe quantities of interest in that phase to aid in describing these systems in detail.

3.0.5 The Grand-Canonical Ensemble

The previous two ensembles hold both the number of particles and the temperature constant. Each are employed to study averages of the form in Equation 3.15, but are unsuitable for studying properties of the system directly related to the partition function, which in turn are related to the effective volume in configuration space accessible to the system at some collection of state parameters [68]. Quantities of this sort include $\mathcal{G}$ or $\mathcal{A}$, and entropy $\mathcal{S}$ and cannot be measured directly using Metropolis sampling [68]. One can use Metropolis sampling to calculate differences in these quantities and the Grand-Canonical (GC) ensemble makes use of this fact. The GC ensemble connects the simulation cell of system size N to a reservoir of ideal gas particles, in a similar way to that employed in the NPT ensemble, of size M, and takes the limit of an infinitely larger ideal gas reservoir, i.e. $M/N \to \infty$, yielding the GC partition function

$$\mathcal{Q}_{\mu VT} \equiv \sum_{N=0}^{\infty} \frac{e^{\beta\mu N} V^N}{\Lambda^3 N!} \int \vec{\mathbf{s}}\, e^{-\beta\mathcal{U}(\vec{\mathbf{s}})}, \tag{3.13}$$

where, since the volume of the simulation cell volume is proportional to the ideal gas reservoir volume, the integral is in terms of the scaled coordinates $\vec{\mathbf{s}}$, and the leading sum quantifies a conversion factor from the chemical potential of the ideal gas, since the chemical potential is related to the number density ρ,

$$\mu_i = \beta^{-1} \ln \Lambda^3 \rho \tag{3.14}$$

Chemical Potential

An interesting difference between the Grand-Canonical (GC) ensemble and that of the Canonical (NVT) or Isobaric-Isothermal (NPT) ensembles, is that rather than minimising the free energy, as one is wont to do in the the former two ensembles, simulating in the GC ensemble entails imposing the free energy, since $\mu_i = \mathcal{G}/N_i$, i.e. the chemical potential of the i^{th} component proportional to $\mathcal{G}$ by N. This is a mixed blessing, since we have an inverse method of controlling the phase-space we explore, and yet we don't know *a priori* what the value of $\mathcal{G}/N$ should be. It is apposite to have well characterised and reliable reference system(s)[1].

3.1 Monte Carlo

Integrals of large dimensionality, such as those outlined in the previous section cannot be solved effectively by simple quadrature. Due to the portion of time such an approach would expend on evaluating the integrand in regions of the configuration space possessing vanishing weight factor it would render solution by hand of this type of problem only tractable for the smallest systems or the fewest number of degrees of freedom. This problem is greatly exacerbated by the potential energy function we have chosen, by rendering any configuration that yields an overlap between particle core diameters with a zero weight factor. Numerical methods for exploring the potential energy landscape for complex particle systems are applied. The Monte Carlo (MC) approach takes its root in the dawn of modern computing machines as one of the earliest methods of number crunching for the numerical study of diffusion processes involved in nuclear reactions of fissionable materials on the earliest computers. The name *Monte Carlo*, suggested by Nicholas Metropolis, ostensibly[2] deriving from its vast use of pseudo-random number generation. The method itself is extremely flexible and can be applied to problems in fields as diverse as the physical sciences, engineering, computer graphics, artificial intelligence, and even finance. We make use of MC techniques here to solve integrals of large dimensionality in a systematic manner.

We are interested in exploring $\mathcal{M}$ to obtain information relating to regions with high probability and thus in need of a rational method of doing so. At the outset it should be fairly intuitive that not all choices of values for the set of particle configurations $\vec{\mathbf{r}} = \{\vec{r}_1, \vec{r}_2, \ldots \vec{r}_i\}$, for $i \in [1, \mathbf{N}]$, will possess a non-vanishing weigh factor. We develop a method of generating $\vec{\mathbf{r}}$ such that we ensure those generated states are from regions of the configuration space with non-zero weight.

Averages

We want to measure observable quantities that are averages over phase space. A formulation of such an average, making use of the partition function in a given ensemble for a space capturing phase ω, the partition function $\mathcal{Z}_\omega$ from Equation 3.12, we have

---

[1] A modestly thorough analysis of the square-well reference system can be found in Section 2.2.1

[2] Though anyone who takes an interest in the development of computing machines might surmise that the project file name Monte Carlo actually derived from a spendthrift uncle of Stanislav Ulam who notoriously borrowed money from relatives since he “just had to” visit a particular Monegasque town.

$$\langle \mathbf{A} \rangle_\omega = \frac{\int_\omega \mathrm{d}\vec{\mathbf{r}}_\omega \, e^{-\beta \mathcal{U}(\vec{\mathbf{r}})_\omega} \mathbf{A}(\vec{\mathbf{r}})}{\int_\omega \mathrm{d}\vec{\mathbf{r}}_\omega \, e^{-\beta \mathcal{U}(\vec{\mathbf{r}})_\omega}}, \tag{3.15}$$

where $\langle ... \rangle$ denotes an average over the generated states in the configuration space of the ensemble and the quantity $\mathbf{A}(\vec{\mathbf{q}})$, is some function of the particle coordinates $\vec{\mathbf{r}}$. We want to know the ratio of two integrals [68]. To this end we employ the Metropolis method [70] to sample from points in the configuration space, ensuring detailed balance — that the probability moving between microstates does not change with the evolution of the system — and that the system satisfies the ergodic hypothesis, the average over the ensemble of states generated by the Metropolis method will converge to the correct value.

3.1.1 Algorithm Design

Simulation of particle systems is a fairly routine procedure with many modern codes developed with specific aspects of the simulation technique in mind. For more specialised or exquisite types of simulation, code is often inherited with all of the foibles and shortcuts and poor code practices (which everyone has, no matter their experience, fondness for particular ways of performing certain tasks or the reliance on ‘classic’ languages that should have been laid to rest decades ago). The process of writing code from scratch is a rewarding, even if frustrating process. Though the link between that modelled and that which it is modelled upon may be tenuous at best. With all this in mind, this section will describe some “tricks of the trade” that make the simulation approach not only manageable conceptually to a non-coder, but will also attempt to give the Reader a deeper understanding of how these structures can be used to make a simulation very efficient. The language of choice for the Author is ANSI C, using the C99 standard. All non-standard libraries employed are listed in the subsection in which they are used.

The bones of a Monte Carlo algorithm is very simple and proceeds as follows:

Algorithm 1 A Monte Carlo code

```
Prepare the system in a beginning configuration., $\vec{\mathbf{r}}$,
Define END condition
while not END do
    Generate a trial configuration, $\vec{\mathbf{r}}'$,
    Conditionally accept the new configuration
    Sample
    if END then:
        break
```

MC simulations are run for some number of iterations over moves of each particle. One move of each particle is here termed a Monte Carlo Sweep (MCS). Which particle is moved is chosen stochastically such that on average one trial move of each particle is attempted in each sweep. There are many ways in which one may end a simulation. Conventionally, an MC simulation comes to an end after a predetermined number of MCSs. Here we employ an automated ending condition. Several metrics are monitored over the course of a simulation. For example, if we are trying to optimise the system energy we can monitor the fluctuations in the energy metric, define a tolerance value (some small number of multiples of the standard error of the mean (SEM) within a sampling block), and wait until the average value remains approximately constant. In the MC simulations employed here we optimise four quantities before engaging in equilibrium sampling. These quantities are firstly the system energy, since we expect clustering in our systems we also monitor the the average number of monomers, the average size of a cluster, the largest cluster, and the average number of clusters, only when all of these values are constant to within three SEM, do we commence equilibrium sampling for a prescribed number of samples. In this way simulations can be run and left until they have completed.

(*pseudo*-)Random Numbers

All algorithms in this section are based upon — or measuring of something proportional to — the stochastic evolution of the system. This requires a source of pseudo-random numbers. The Mersenne Twister (MT) algorithm is employed here. MT has a period of $2^{19937} - 1$ 623-dimensional equidistribution up to 32-bit accuracy [71]. A wrapper containing modifications to the original algorithm is used that generates signed and unsigned floats and integers, as well as varying bit-depth

3.1.2 Representation of Particles

Firstly the fundamental actor in these simulations is the particle. Since we study the behaviour of tangent-sphere Janus dumbbells we can decompose our particle position vector $\vec{r_i}$ into its sub-particles, $\vec{r}_{i_s}$ and $\vec{r}_{i_h}$. We can then decompose those into their vector components:

$$\vec{r_i} = \begin{cases} \vec{r}_{i_s} = \{x_{i_s},\, y_{i_s},\, z_{i_s}\} \\ \vec{r}_{i_h} = \{x_{i_h},\, y_{i_h},\, z_{i_h}\} \end{cases} \tag{3.16}$$

To each particle a unit vector $\vec{u} \equiv \{u_x,\ u_y,\ u_z\}$ is assigned that describes orientation of the particle. This unit vector is located on the square-well sphere and points in the direction of the hard-sphere component. Defining the particles in this way implies some properties in both the way it can be represented in memory and the way new configurations of a single particle are generated.

Structures

Making use of 'structures' in C is very useful. Since being defined as the *union* of 3 different components, namely the *sticky* sphere, the *hard* sphere, and the *orientation* unit vector, the rather minimalist structure that represents each particle is shown in listing 3.1 below.

```
typedef struct particle {                // structure for particles
    double sw[3];                        // square well component
    double hs[3];                        // hard sphere component
    double u[3];                         // unit vector for orientations
};
```

Listing 3.1: Particle representation

Declaring arrays of N particles can then be achieved simply by writing `particle array[N]`, and individual sub-particle elements accessed by using the dot (`.`) operator, say for the y component of the hard-sphere sub-particle of particle index 563, y_{563_h}, setting it to 5.6375874672,

```
array[563].hs[1] = 5.6375874672;
```

Listing 3.2: Accessing particle structure sub-particle vector components

Representing the particles in this way also allows them to be passed as either whole arrays or as single particles to functions that act on them. This is advantageous since often a potential evaluation may be performed on a particle structure which is not yet in the array that contains the others (for example, if we are simulating in the GC ensemble).

3.1.3 Moves

The types of particle moves we employ are conventional rotations and translations. In both cases the move is carried out following the same logical flow which is outlined in Algorithm 2

Algorithm 2 Logic for moves of arbitrary type

```
    Select seed: $i$,
    Calculate energy of old state: for $i$, $U_o$
    Save $i$ coordinates: to $x_{i,o}$
    Generate new position: for $x_{i,n}$
    Calculate energy of new state: for $i$, $U_n$
    Calculate Difference in energy: $\Delta U = U_n - U_o$
    if $genrand() < e^{-\beta \Delta U}$ then:
        Accept.
        Update position: set $x_i = x_n$
    else:
        Reject.
        Set $x_i = x_o$
```

Displacements

Displacements are generated by updating the current position of the selected particle. A displacement vector, $\vec{\Delta}$, is generated. This vector is chosen from a cube with unit side length and has x, y, and z components modified by the floating point step size parameter `dmax`. New positions are generated by adding a vector of length defined by the interval (0, $\sqrt{3}$`dmax`) and updating the position of the hard-core sub-sphere according to the new position, where the `hs` component's position is related by the unit vector modified by the parameter `sigmix`[3], so for the i^{th} particle:

```
for (int ax = 0; ax ⩽ 2; ax++) {
        array[i].sw[ax] += (genrand_real()-0.5) * dmax;
        array[i].hs[ax] = array[i].sw[ax] + array[i].u[ax] * sigmix;
}
```

Listing 3.3: Generating new displacements

This implies that the hard-sphere portion of the dumbbell just tags along for pure translation moves as a passive entity. This approach is distinct from other approaches for molecular rotations where the centroid, or centre of mass is rotated and the constituent points constructed anew. The value of `dmax` is variable only during the equilibration portion of a given simulation. Its value is begun at a small value (typically 0.1) and allowed to grow or shrink depending upon the acceptance rate of moves. The method of modifying the step size parameter(s) is described in more detail below.

---

[3] `sigmix`$= (\sigma_s + \sigma_h)/2$.

Rotations

Rotations are generated by modifying the unit vector, $\vec{u}$, describing the orientation of the particle by assigning a small rotation to a stochastically chosen axis. During this move the square-well component remains fixed and only the hard-sphere component moves. New orientation vectors are generated in the following way, making use of another step size maximum `rmax` and applying a rotation matrix method, for rotation, R, about an axis $x, y, or z$, by angle θ, where $\alpha = \sin\theta$ and $\beta = \cos\theta$:

$$R_x(\theta) = \begin{bmatrix} 1 & 0 & 0 \\ 0 & \beta & \alpha \\ 0 & -\alpha & \beta \end{bmatrix}, \quad R_y(\theta) = \begin{bmatrix} \beta & 0 & -\alpha \\ 0 & 1 & 0 \\ \alpha & 0 & \beta \end{bmatrix}, \quad R_z(\theta) = \begin{bmatrix} \beta & \alpha & 0 \\ -\alpha & \beta & 0 \\ 0 & 0 & 1 \end{bmatrix}. \tag{3.17}$$

Here

Volume Moves

Volume moves are perfromed by random walk in $\ln V$, either by keeping the cell geometry unaltered, I.e. forcing the cell to remain cubic, or by relaxing the aspect ratio constraint and allowing the simulation to decide the box geometry. In the case where the box lengths are all individually variable, the random walk in the volume is performed in the log of the box length space, L_a, where $a \in x, y, z$

Modifying Step-size Maxima

Step size maxima are allowed to vary during the equilibration section of each simulation. The values of `dmax` and `rmax` are linked to the efficiency of the simulation by means of the acceptance rates. These quantities are varied—on the fly—such that the acceptance rates for each type of move are maintained around 0.4, or 40%. In contrast the value `vmax` is pegged to the acceptance rate maintaining the acceptance rate of 20%, which is sufficient to sample the volume space efficiently. Once the equilibration stage of the simulation has ended these values are fixed to their most recent values.

3.1.4 Periodic Boundary Conditions

All simulations were carried out in boxes of side length L with periodic boundary conditions. In the two all Canonical ensemble simulations were carried out in static cubic boxes. Simulations in the Isothermal-Isobaric ensemble where the structure was expected to be lamellar were carried out in orthorhombic simulation cells with individually variable box dimensions, L_x, L_y and L_z. Simulating particle systems in this way allows us to calculate what is effectively an infinite system, providing two conditions are met: Firstly, that the system size (N) is large enough that certain intensive quantities do not change with increasing the simulation box size, extinguishing any finite size effects; and secondly, that any simulation prepared to meet the first condition be small enough that the problem to which the simulation is applied is tractable with current computing resources. A few methods for making simulations large enough to meet the first criteria extremely efficient and fast are outlined in the following few sub-sections.

3.1.5 System Energy

The fundamental quantity that we wish to optimise to achieve a set of equilibrium configurations is the system energy. Due to the fact that our interaction potential is *discrete* and *discontinuous* by definition this makes for some simple methods of calculating the energy efficiently. For each particle there are two interaction sites. this implies that for each pair (between particles a and b of particles we must calculate four interactions: one square-well interaction between sub-particles $a_s \leftrightarrow b_s$; and three hard sphere interactions $a_h \leftrightarrow b_h$, $a_s \leftrightarrow b_h$, and $a_h \leftrightarrow b_s$. This problem then becomes that of finding the distance $d\vec{r}_{ab}$ between sites and updating the pair energy accordingly. This could be calculated by a generalisation of the Pythagorean right angle triangle theorem, which implies that a square root would be required to get the distance. In practice we calculate the squared distance between the particle and compare that to the square of the interaction range. This circumvents the requirement of employing the `sqrt()` function, which is notoriously slow and since we need to do this billions of times would be impractical.

Distance^2 and Bonds

Calculating the distance square is simple. All one must do is sum up the squared differences in position vectors that describe each particle's location in space. For particle a and b, for each site, since we have four sites and interactions, these distances squared are, for sites $w \in \{s, h\}$,

$$\mathrm{d}\vec{r}^{\,2}_{w:w} = (\vec{r}_{b_w} - \vec{r}_{a_w})^2 = (x_{b_w} - x_{a_w})^2 + (y_{b_w} - y_{a_w})^2 + (z_{b_w} - z_{a_w})^2, \tag{3.18}$$

There are now four critical lengths that these quantities are compared to in order to calculate the system energy they are σ_s^2, $(\sigma_s+\lambda\sigma_s)^2$, σ_h^2, and $((\sigma_s+\sigma_h)/2)^2$. If the squared length between s sub-particles is less than σ_s^2 an overlap has occurred and the interaction is of infinite energy. Any move that accomplishes this is immediately rejected, likewise with distances between h sub-particles and σ_h^2, and between s and h sub-particles and length $((\sigma_s + \sigma_h)/2)^2$. The penultimate distance is that between s sub-particles again, except where that length is greater than σ_s^2 and less than $(\sigma_s + \lambda\sigma_s)^2$ which has an interaction energy of $-\varepsilon$. Two particles that meet this condition are considered to be bonded, and contribute a unit of ε to the overall system energy. All other distances greater than the largest of the four aforementioned interaction ranges are considered too great to be interacting are defined to have no energy of interaction.

3.1.6 Speeding Up

Obviously calculating the interaction energy of a given particle that undergoes a move with all $N-1$ particles in the simulation box is a time consuming process and for discrete potentials is completely unnecessary. This problem is N-fold worse for situations where a whole system energy is required, such as simulations that sample the volume where all $N \times N$ particle interactions should be accounted for. A few methods of speeding up the calculation of particle interactions can be employed. The Author directs the Reader to texts concerning other space discretisation methods such as tree structures, which can suffer from slow lookup times depending on the way in which the space is partitioned. A powerful method is used here, the cell list, with a few specialisations (for example using pointers and linked lists, as well as considering each sub-particle as an individual particle and thus the same whole particle can be in two cells simultaneously).

Cell Lists

Cell lists are a form of space discretisation meta-structure whereby static cell structures which point to dynamic linked-lists are superimposed on the simulation box. This structure segments the space into small containers, optimally containing a single particle. Dividing the simulation space allows us to restrict the evaluation of particle interactions to the space immediately surrounding a given particle. In practice, however, the method requires that the cells be of a minimum size in order to ensure particles that have the potential to interact are not neglected, which in turn depends on the maximum particle interaction range. The simulation box is divided into $N_x \times N_y \times N_z$ individual cells of equal volume which is determined by taking the smallest possible number of boxes required to make cells that must be at least greater than the largest of the interaction ranges, by taking

```
cells_x = floor(boxX / cell_size);          // Smallest number of boxes
cell_size_x = boxX / cells_x;               // Actual box size in x
```

LISTING 3.4: Determining the cell dimensions. The actual box size in x is always greater than the desired `cell_size`, which in turn is always greater than the largest interaction range

Once the box dimensions are decided the cell structure can be declared and superimposed on the simulation box.

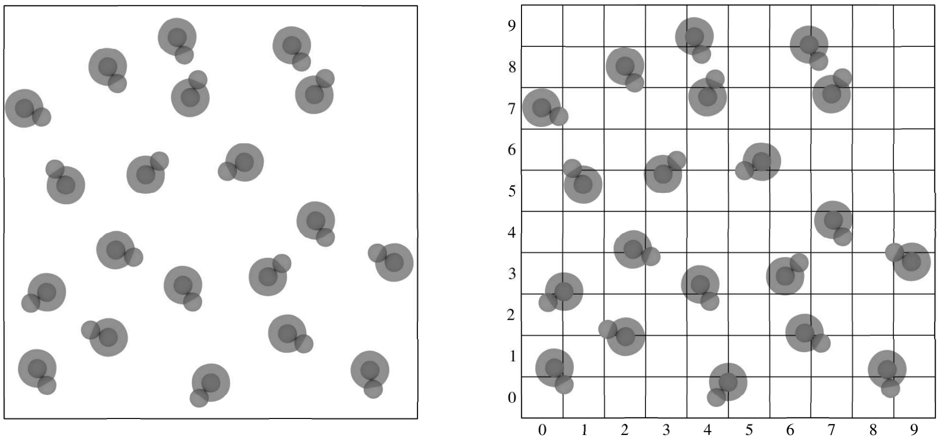

FIGURE 3.1: The two dimensional simulation box on the left is divided up into $N_x \times N_y$ cells, indexed from zero, on the right. Cells are at a minimum the size of the largest interaction length.

Each particle is assigned a list structure, containing the index of the particle and the particle sub-particle `type` which can be linked together to form the cell list:

```
typedef struct list {           // structure for cell contents
    int index;                  // index of the particle
    int type;                   // type of particle - hs=0, sw=1
    struct list *next;          // link to the next particle in the cell
};
```

LISTING 3.5: The linked list structure. Containing the particle's `index` and the sub-particle identifier `type`.

and finally pointed to by the cell list structure—a map of the cells, and a pointer to the first particle found in the cell—indexed by their cell address:

```
list* cell[cells_x][cells_y][cells_z];  // Cell list structure.
```

Listing 3.6: Generating the cell address pointer structure. A three dimensional array of pointers to linked lists.

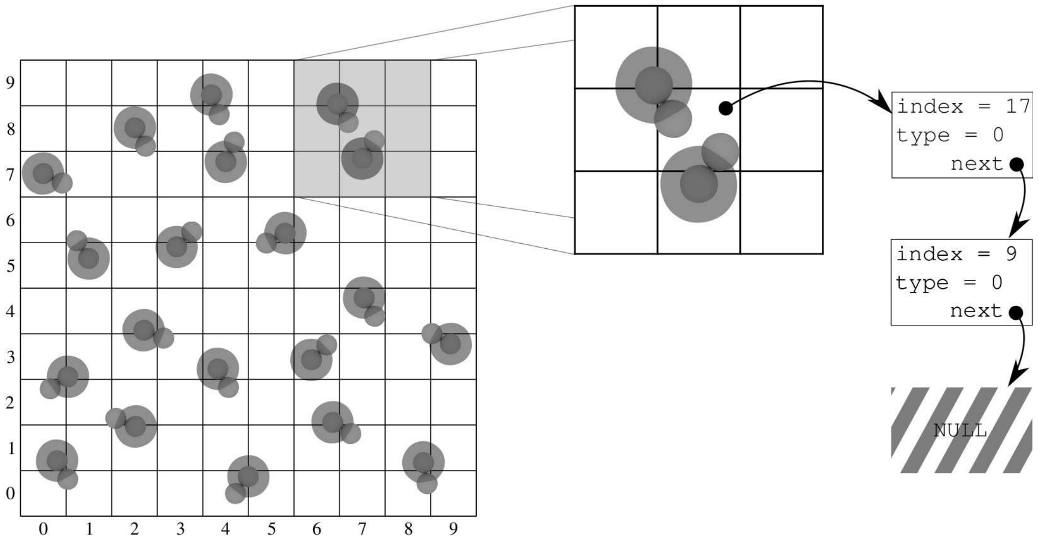

Figure 3.2: A two dimensional pictorial representation of the cell structure, the contents of the cell, and the linked list containing the particle identifiers.

The cell that a given particle is in is determined by the vector component in each of the three dimensions. For the x co-ordinate of particle i's s sub-particle, the corresponding x cell is (likewise for the other cell dimensions, with appropriate index and sub-particle):

```
i_sw_cell_x = floor(array[i].sw[0] / cell_size_x);
```

Listing 3.7: Cell occupancy. The cell's x coordinate for particle i's s sphere

Using this structure one needs to calculate $\mathrm{d}\vec{r}$ of only those particles in the cells surrounding a particle's host cell (including the host cell). In the two dimensional case in Figure 3.2 only contents of the surrounding 8 cells must be considered in assessing the potential, outside of this particle interactions can be neglected. In the limit of single occupancy, i.e. one sub-particle in each cell, the algorithm should in principle scale as $\mathcal{O}(n \log n)$. In practice, due to the cells being at lease the size of the largest interaction range, it is possible that more than one sub-particle occupy each cell (strictly speaking this is also true of 2D and 3D cells with side length σ whose diagonals are $\sqrt{2}\sigma$ and

$\sqrt{3}\sigma$) so the scaling will be slightly different, in either case the total system energy is computed more quickly than $\mathcal{O}(N^2)$.

3.2 Advanced methods

During the course of investigation of this class of particle it is variably observed that aggregation phenomena at finite temperature may be restricted by a kind of kinetic barrier to diffusive modes of the particles through the simulation cell. Given the move algorithms outlined in the previous section, the diffusive behaviour of a particle through the simulation cell is essentially a Wiener process. Where in the presence of strongly directional or discrete potentials (or both, as is the case in the present work), the diffusion of a particle across the cell can be suppressed A number of methods have been devised to circumnavigate this pathology here we employ the Aggregation Volume Bias Monte Carlo move algorithm.

3.2.1 Aggregation Volume Bias Monte Carlo

Aggregation Volume Bias Monte Carlo [66, 67] (AVBMC) is a non-local *intra*-box swap move whereby particles leap across the simulation box in such a way as to enhance the sampling of configurations which can be suppressed in schemes employing conventional roto-translation move algorithms. The suppression of diffusive modes of particles across the cell, a sort of kinetic bottleneck, can plague simulations of even simple particle systems that have any kind of shape or interaction anisotropy, or are strongly associating [66, 72]. The AVBMC algorithm is very simple to implement, yet extremely powerful as a method of avoiding this kinetic bottleneck in simulations where clustering of strongly interacting particles can prevent structural relaxation to equilibrium geometries. Implemented here is a single version of the move selection algorithm, taking heed of an extension to the first AVBMC “in the spirit” of the multiphase Gibbs ensemble [67] (referred to as AVBMC in the original paper), making use of two classes of acceptance condition for different outcomes of the move selection procedure. For a more thorough discussion of the method the reader is directed to [66, 67].

Bonding Volume

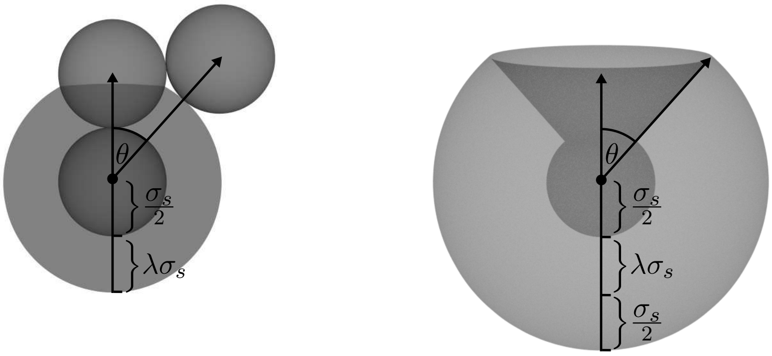

FIGURE 3.3: The *in* region of a particle for use with AVBMC. It is defined by the furthest distance away an s sub-particle can contribute to $\mathcal{U}$. The volume consists of a layer of a sphere of radius $\sigma_s + \lambda\sigma_s$ with a conical section subtracted as defined by angle from the nearest approach of a sticky sphere to the non-interacting sub-sphere.

In order to define the intra-box swap move at the core of the AVBMC algorithm, we must first define a volume around each particle that contains a space in which another particle can approach and be considered bound. This volume, v_{AVB}, is defined as

$$v_{AVB} = \frac{\pi}{6}\left[8(\sigma_s + \lambda\sigma_s)^3 - \sigma_s^3\right]\left(1 - \left(\frac{1}{2} - \frac{\sigma_s + \lambda\sigma_s}{2(\sigma_s + \sigma_h)}\right)\right), \tag{3.19}$$

which corresponds to the volume of a spherical-shell, minus a spherical cone segment with angle defined by the nearest approach of another sticky sub-particle to the hard-sphere component at the greatest distance that can still be considered bonded and thus whose centre lies at the boundary of the bonding volume in question. Figure 3.3 demonstrates this volume and its constituent parameter make-up for the case of $\alpha = 1.0$. Any sticky particle is considered to be in the *in* region of a given particle if its centre lies within this volume, and in the *out* region if without. Three different forms of acceptance condition are employed for each of the scenarios: *in*→*out*, *out*→*in*, and most importantly *in*→*in*.

Move Type Selection

The selection of the type of moves the AVBMC algorithm employs is performed by considering three particles, i , j, and k. The *in* and *out* regions of j are referred to as j_{in} and j_{out} and their volumes V_{in}^j and V_{out}^j, respectively. The move type selection proceeds according to the biasing probability, P_{bias}, which determines the direction of the move of i with respect to j i.e. toward j_{in}, $i \in V_{in}^j$, or with complementary probability $1 - P_{bias}$ toward j_{out}, $i \in V_{out}^j$. The second step depends upon the first: If we are moving i

to j_{in}, the second step determines the origin of i. With equal probabilities i is chosen from either the bonding region of k, k_{in}, or from j_{out} (which also contains k_{in}); If on the other hand we are moving i from a j_{in} configuration, the second step determines whether the destination of i is a k_{in} or a j_{out} configuration (which likewise contains k_{in}), with equal probabilities. If i is translated to or from a j_{out} configuration some accounting is required to determine whether the origin or destination (respectively) is in fact a k_{in} configuration, since as mentioned above, the volume V^j_{out} also contains k_{in} and so will determine type of move we are performing and thus the form of the acceptance condition.

Acceptance Conditions

The form of the acceptance condition depends upon the type of move we have generated. If the move type selection process results in an *in* → *out*, or *out* → *in*, the appropriate form of acceptance condition is one of the following two:

$$\mathbf{acc}(j_{in} \rightarrow j_{out}) = \mathbf{min}\left[1, \frac{P_{bias} V^j_{out} N^j_{in} e^{-\beta \Delta U}}{(1 - P_{bias}) V^j_{in} (N^j_{out} + 1)}\right], \tag{3.20}$$

$$\mathbf{acc}(j_{out} \rightarrow j_{in}) = \mathbf{min}\left[1, \frac{(1 - P_{bias}) V^j_{in} N^j_{out} e^{-\beta \Delta U}}{P_{bias} V^j_{out} (N^j_{in} + 1)}\right], \tag{3.21}$$

where $V^j_{in} = v_{_{AVB}}$, $V_{out} = V - V^j_{in} - V^k_{in}$ (where $V^j_{in} = V^k_{in}$ such that the factor is really $2v_{_{AVB}}$, yet the subscript maintained to denote the origin of this volume factor), N^j_{in} quantifies the number of bound neighbours of j i.e. the number of particles whose sticky sub-particle lie within the bonding region of j, and N^j_{out} all of those without (including k). The third case, *in* → *in*, has a slightly different form of the acceptance condition. For a move of particle i from j_{in} to k_{in} ($j_{in} \rightarrow k_{in}$) the following acceptance condition is used

$$\mathbf{acc}(j_{in} \rightarrow k_{in}) = \mathbf{min}\left[1, \frac{P_{bias} V^k_{in} N^j_{in} e^{-\beta \Delta U}}{(1 - P_{bias}) V^j_{in} (N^k_{in} + 1)}\right]. \tag{3.22}$$

And for $k_{in} \rightarrow j_{in}$, with complementary probability factor $(1 - P_{bias})$ featuring instead in the numerator,

$$\mathbf{acc}(k_{in} \rightarrow j_{in}) = \mathbf{min}\left[1, \frac{(1 - P_{bias}) V^j_{in} N^k_{in} e^{-\beta \Delta U}}{P_{bias} V^k_{in} (N^j_{in} + 1)}\right]. \tag{3.23}$$

The logic of the AVBMC is condensed below in Algorithm 3.

Algorithm 3 Logic for AVBMC moves

```
Select 2 particles: $j$ and $k$ such that $j \neq k$ and $V_j^{in} \cap V_k^{in} = 0$
if (genrand() $< P_{bias}$) then:
    if (genrand() $< \frac{1}{2}$) then: Select $i$ from $k_{in}$,
    else: Select $i$ from $j_{out}$,
    Translate $i$ to $j_{in}$.
else: Select $i$ from $j_{in}$,
    if (genrand() $< \frac{1}{2}$) then: Translate $i$ to $k_{in}$.
    else: Translate $i$ to $j_{out}$.
Determine move type.
Apply appropriate acceptance condition.
```

This algorithm still suffers some major flaws. Where monomer populations are depleted, say due to the region of configuration space a simulation is being run, moves which attempt to move a particle from an *out* configuration may be rejected with high probability. In the same scenario it is likely that all particles lie in fairly low lying energy configurations (for example in a liquid droplet) where the probability that one will select a relatively high energy particle to move to an *out* configuration is vanishingly small. In addition, with random selection of j and k, required for the balance condition, translating a particle from either an j_{out} or k_{in} to a j_{in} (or the opposite indices) where there is significant clustering will lead to rejections based on hard-core overlaps. This problem is exacerbated by the presence of the hard sphere portion, where its orientation is determined stochastically. This idiopathy leads to generally low acceptance rates of all AVB moves. In spite of this even a rapidly decreasing acceptance rate seems to be enough to edge the system toward equilibrium configurations at a much faster rate than only conventional roto-translations. This is due largely to the non-locality of the displacement moves. Since, in order to form a bond between any two particles across the box, with small `dmax` this process may take many steps, given also that discrete potentials offer no long range tendency to draw disparate particles near one another, a simulation may run its course without two particles ever meeting. The AVBMC algorithm therefore circumvents this diffusive barrier and so allows us to accept its low acceptance rate as an idiosyncrasy, rather than a pathology. Several innovative methods have been developed to mitigate this problem [73], none are implemented in the current study.

3.2.2 Simulated Annealing

Simulated annealing (SA) is a meta-heuristic optimisation process for achieving an approximation to a global optimum in a combinatorial parameter space [74, 75]. In principle the SA approach is more efficient than global optimisation techniques in certain cases. The process proceeds by slowly varying a system parameter over the course of a simulation in order to effect a thorough exploration of configurations around each point on the parameter trajectory to ultimately arrive at a good approximation to a global minimum. Though the technique can be applied to any particular thermodynamic parameter in principle, here we have varied temperature (as is implied by the term *annealing*), in order to approximate minima in the global free-energy landscape. The SA approach carries some caveats. There is no guarantee that a structure obtained via a single SA is a global minimum for the state point. In order to mitigate any mischief caused by this fact we can reduce the likelihood of having *fluked* a high energy structure (or a low energy one), where the system may have a series of low lying or degenerate structures to choose from, a cohort of SA simulations are run with different RNG seeds and an idea of the structural diversity, if indeed there is any, can be obtained.

3.2.3 Successive Umbrella Sampling

Successive Umbrella Sampling (SUS) extends a method for estimating free-energy estimation [76] whereby the range of states to be explored by the umbrella sampling procedure is restricted to windows of width ω, beginning at zero density and investigating windows one after the other such that the state space can be traversed without the need for a weight function as is the case with multicanonical approaches [77, 78]. A histogram $H_k[n]$ records the how often the simulation visits each state in the k^{th} window $[k\omega, (k+1)\omega]$. The left and right bins of each histogram, $H_{kr} = H_k[k\omega]$ and $H_{kl} = H_k[(k+1)\omega]$, and their ratios $r_k \equiv H_{kr}/H_{kl}$ can then be compiled to yield an unnormalised probability distribution

$$\frac{P[n]}{P[0]} = \frac{H_{0r}}{H_{0l}} \cdot \frac{H_{1r}}{H_{1l}} \cdots \frac{H_k[n]}{H_{kl}} = \prod_{i=1}^{k-1} r_i \cdot \frac{H_k[n]}{H_{kl}} \tag{3.24}$$

In the limit of small ω, *i.e.* $\omega = 2$, individual simulations can be run in parallel (providing the computational resources are available), such that if the space is distributed over N_{proc} processors the resultant speed up for an MC algorithm with scaling $\mathcal{O}(n \log n)$ will be proportional to $(\sum_{k=1}^{N_{max}} N \log N)/N_{proc}$. Separating the simulation space into separate individual simulations also has the effect of removing any bias associated with short simulations lengths usually used in SUS sampling that can offer configurations at higher density that have preserved structures from formed at lower densities.

Histogram Reweighing

Histogram reweighting is performed by segmenting the N space and the corresponding $P(N)$ into regions corresponding to the different phases encountered over N and identifying minima in the $P(N)$ which delineate regions of different phases, where $P(N)$ is comparatively large. After locating satisfactory minima in $P(N)$, the areas astride are compared to identify the direction which we must modify the distribution to yield equal areas (and thus equal volume of phase space). The process is carried out by multiplying the histogram by a factor of the chemical potential μ_f. Here we will switch our distribution to $P(\rho)$ (which implies dividing each N by the simulation cell volume V). [4] At each ρ_i, $P(\rho_i)$ is modified by multiplying by a power of μ_f according to

$$P'(\rho_i) = P(\rho_i)\mu_f^{\rho_i}, \tag{3.25}$$

with total area normalisation, and the reweighting process applied recursively until the compared regions are equal in area. The weight factor μ_f is modified by a single protocol, i.e. for coexisting phases ω and ψ, with areas in the $P(\rho)$ distribution A_ω and A_ψ and $\rho_\omega > \rho_\psi$

$$\mu_f = \begin{cases} (1+\delta)\mu_f & A_\omega < A_\psi \\ (1-\delta)\mu_f & A_\omega > A_\psi \end{cases}. \tag{3.26}$$

A non-zero μ_f indicates that $\mu \neq \mu_{coex}$. If, after the re-weighting process, the factor by which we modify the imposed μ at the outset of the simulations lies outside the tolerance range of $\mu_f \in (0.98, 1.02)$ the starting μ is scaled by a factor proportional to μ_f and the simulation set begun anew. In practice, the compilation of the histogram can run into issues associated with memory underflow, where successive multiplications of low histogram ratios over regions of the density space with diminishing probability, for example intermediate densities between highly probable regions. To mitigate this problem, the compilation and reweighting process can be performed in *log* space with the operations altered appropriately

---

[4] The process is identical if unmodified from the N space, with the exception that the index in Equation 3.25 is simply N.

3.3 Metrics

3.3.1 Cluster Analysis

A robust method for determining the properties of clusters is required in order to diagnose certain critical properties of the system. These include, but are not limited to, cluster size distributions, percolation loci, radii of gyration, and a host of metrics associated with cluster geometry. In order to study the clustering properties of our model systems we must first decide which particles belong to which clusters. This task begins with finding the bound neighbours for each particle then figuring out which particles are bonded to one another through this network of bonds. There are a few methods of achieving this task, all involve borrowing some ideas from graph theory. A graph is a mathematical structure to analyse pair-wise relationships between objects. A graph consists of nodes and edges.

Bonding Networks

Firstly a structure for each particle is defined that contains information about its immediate neighbours. We shall refer to these as nodes, their representation in code is in Listing 3.8 below,

```
typedef struct network {              // structure for networks
    int bonds;                        // How many neighbours
    int nets[MAXBONDS];               // node connectivity up to MAXBONDS
    int label;                        // current cluster label
    int counted;                      // has it been counted?
}node[N];
```

Listing 3.8: Node structure for traversing networks of bonds

Each particle's node `nets[]` array is populated with it's neighbours, the nodes to which the current node is bonded (by the criteria outlined in 3.1.5) making use of the cell list structure. Each time a new bond is found the `bonds` counter is incremented and the index entered into the corresponding entry in the `nets[]` array. Once all of a particle's neighbouring nodes have been identified, preformed over all N nodes such that the total connectivity is known, we can then traverse the system of nodes to *label* them with the appropriate cluster index.

Recursive Functions

The process of cluster labelling can be thought of in graph theoretic terms by performing a depth first search on a graph. This process can be achieved recursively or iteratively. Though the iterative method is in general faster, for graphs of relatively arbitrary connectivity, elegant iterative solutions require special attention. Though small problems can be solved with what essentially amounts to *magic*[5], the recursive versions are easier to write, implement, and have the benefit of leaving the details of traversing the network up to the order in which they appear in the node list, via the depth first search. For more details of performing the basic depth first search method the Author directs the Reader to a basic introduction text on graph theory of their choice. The particular function used here is detailed in Listing 3.9. Note the simplicity of the recursive function `rlabel()`, performing what is in fact a non-trivial task.

```
void rlabel(int N, int i, struct networks node[MAXPARTICLES], int bins[N]) {
    int j, n;
    for (n = 0; n < node[i].bonds; n++) {
        j = node[i].nets[n];
        if (bins[j] == 1) continue;
        bins[j] = 1;
        rlabel(N, j, node, bins);
    }
}
```

Listing 3.9: Recursive function for the labelling process: Function `rlabel()` compiles a list of nodes which all are all connected through the edges of the graph via recursion, once all connected nodes are traversed the array `bins[]` is returned and all of the nodes with corresponding '`true`' entries in `bins[]` are given the label `clustnum`.

Cost and Sampling Frequency

Recursive functions of this kind are computationally expensive, so analysis that makes use of these data cannot be performed every sweep. In fact it is unnecessary to do so for particle systems with slow rearrangement time scales since sampling too many adjacent microstates will not give us a good picture of the overall structural variation in phase. In order to mitigate the expense and ensure that long simulation times are not compounded large amounts of wall-time spent computing node connectivities or the like an austere approach to sampling cluster configurations is employed.

---

[5] http://stackoverflow.com/questions/2209860/how-does-this-work-weird-towers-of-hanoi-solution, this particular implementation makes use of bit-shifting and binary and/or operators, often fondly referred to by coders with the moniker in the text.

3.4 Metrics

In order to characterise phase transitions, cluster phases, and other self assembled structures, a range of distribution functions are employed.

3.4.1 Distribution Functions

Radial Distribution Functions

The radial distribution function can be calculated over a given ensemble by computing

$$\boldsymbol{g}(\mathbf{r}) = \frac{N(N-1)}{\rho^2 \mathcal{Z}_{NVT}} \int \mathrm{d}\mathbf{r}_3 \mathrm{d}\mathbf{r}_4 \ldots \mathrm{d}\mathbf{r}_N e^{-\beta \mathcal{V}(\mathbf{r}_1, \mathbf{r}_2, \ldots \mathbf{r}_N)} \tag{3.27}$$

In practice in computer simulation the following average is employed

$$\mathbf{g}(\mathbf{r}) = \rho^{-2} \langle \sum_i \sum_{j \neq i} \delta(\mathbf{r}_i) \delta(\mathbf{r}_j - \mathbf{r}) \rangle = \frac{V}{N^2} \langle \sum_i \sum_{j \neq i} \delta(\mathbf{r} - \mathbf{r}_{ij}) \rangle. \tag{3.28}$$

The radial distribution gives us information about the microscopic structure of our particle systems. In the case of dumbbell particles which contain two spherical sites per dumbbell, a site-wise analysis is performed. For each sample four separate distributions are compiled, $\mathbf{g}(\mathbf{r})_{ss}$ over the s sub-particle pairs, $\mathbf{g}(\mathbf{r})_{hh}$ over the h sub-particles, $\mathbf{g}(\mathbf{r})_{sh}$ over the s-h and h-s sub-particles, and $\mathbf{g}(\mathbf{r})_c$ over the centroids.

Structure Factors S(k)

Local Rotational Invariants

Local rotational invariants are calculated from spherical harmonics performed over groups of bonds of each particle. For each particle, i, the orientation of each of N_b bonds is analysed by finding to which spherical harmonic they belong via the angles θ_{ij} and ϕ_{ij},

$Y_{lm}(\theta_{ij}, \phi_{ij}) \equiv Y_{lm}(\hat{\mathbf{r}}_{ij})$

Average local orientation parameter $\bar{q}_{lm}$ for each i is obtained by averaging over each of N_b bonds that particle i makes,

$$\bar{q}_{lm}(i) \equiv \frac{1}{N_b(i)} \sum_{j=1}^{N_b(i)} Y_{lm}(\hat{\mathbf{r}_{ij}}), \tag{3.29}$$

Local invariants are then computed by summing over l,

$$q_l(i) \equiv \left[\frac{4\pi}{2l+1} \sum_{m=-l}^{l} |\bar{q}_{lm}(i)|^2 \right]^{1/2} \tag{3.30}$$

Bondwise distributions can then be compiled to investigate persistent local environments around each particle.

3.4.2 Sampling Cluster Properties

In any system where clustering occurs it is helpful to have some metrics to account for the properties of the clusters. Three main properties of clusters are targeted for optimisation before production sampling takes place. Averages of the three metrics monitored over each block are the number of clusters, $\langle N_c \rangle$, the number of monomers, $\langle N_{mono} \rangle$, the average cluster size $\langle N_s \rangle$, and the largest cluster. When these converge to stable

Size distributions

Cluster size distributions are computed by compiling histograms of the frequency of observations clusters of a certain size, then normalised to obtain a probability $P(N_s)$ of observing a cluster of size N_s.

Centroid & Centre of Mass

A deceptively tricky quantity to obtain of a given cluster is it centroid (or centre of mass, however we only treat the centroid since these particles do not have an explicit mass). In principle in a given set of co-ordinates, the centroid of a cluster can be calculated as the average position of all of the particles in a cluster. For a cluster of size N_s, the x component of the centroid of a finite cluster, C_x, in $\mathbb{R}^3$, is given by

$$\mathrm{C}_x = \frac{1}{N_s} \sum_{i=1}^{N_s} x_i. \tag{3.31}$$

In a non-periodic system this metric will yield a value consistent with its centroid. Simulations with periodic boundary conditions suffer a few pathologies, however, and it is important to locate and treat these cases specially. For clusters whose bonds straddle a boundary Equation 3.31 would yield a centroid around the centre of the box. This is obviously a failure that needs to be remedied. A method for circumnavigating this pathology is to think of each dimension as lying on the perimeter of a circle [79]. For each dimension, we take the co-ordinate of the i^{th} particle and apply a map, converting each of its Cartesian co-ordinates, say x, to an angle θ_i, by

$$\theta_i = \frac{2\pi x_i}{L_x} \tag{3.32}$$

We then calculate two more quantities, $\psi_i = \sin\theta_i$ and $\chi_i = \cos\theta_i$, where these co-ordinates in the $\psi - \chi$ plane lie on a circle of unit radius. The averages of these values for all N_s are computed and an average angle, $\bar{\theta}$, calculated by

$$\bar{\theta} = \tan^{-1}(-\psi, -\chi) + \pi \tag{3.33}$$

and the centre of mas then backed out by unfolding the map such that

$$x_C = L_x \frac{\bar{\theta}}{2\pi} \tag{3.34}$$

This form of centroid calculation still suffers from some issues, if a system happens to form a cluster that is continuous in all three dimensions, or has some tube-like character percolated in all three dimensions this method cannot appropriately choose a centre of mass. All following metrics rely upon a reliable calculation of the centroid of observed structures. Which means that clusters which span the length of the simulation box must be ignored from the collection of most of the following metrics. The way we have chosen to achieve this is to *provisionally* accept the assigned value of the centre of mass, use it to obtain a radius of gyration and only calculate the following metrics which are susceptible to errors concerning the centroid assignment where R_g is *less* than $L_{box}/2$. After obtaining this data over the system at a particular configuration one can then go ahead and calculate other more interesting properties.

3.4.3 Geometry

3.4.3.1 Gyration Radii

The radius of gyration is an important quantity to analyse for cluster forming particles. It relates cluster morphology to rheological properties and allows analysis of the fractal dimension — a measure of shape complexity — as well as offering a reasonable metric for approximating the percolation threshold over a given co-ordinate path. The average square radius of gyration is obtained as

$$R_g^2 = \frac{1}{N_s} \sum_{i=1}^{N_s} (r_i - \mathrm{C}_c)^2 \tag{3.35}$$

where N_s is the number of particles in the cluster and C_c is the corresponding centroid. For use in metrics involving the R_g a cluster-wise version can be obtained by omiting the ensemble average denoted by the angular brackets. Monitoring R_g with respect to L_{box} also allows crude estimation of the percolation locus, where $R_g^{max} \approx L_{box}/2$.

3.4.3.2 Dimensionality of Aggregate Systems

It is possible to carry out an analysis of the complexity of aggregates by use of a relation between the number of particles in a cluster N_s with the cluster radius of gyration R_g. The resulting relation can be expressed as a power law:

$$N_s = k_f \left(\frac{R_g}{\alpha_0} \right)^{D_f} . \tag{3.36}$$

Equation 3.36 gives a method to find what is usually called the Fractal Dimension, D_f. Plotting the logarithm of N_s against the logarithm of R_g can be fit linearly, to give the slope, D_f, and the fractal pre-factor k_f. The scaling factor α_0 is simply the average diameter of each monomer in the cluster calculated as $(\sigma_s + \sigma_h)/2$, but is not used to scale the data during processing, instead a unit of σ is factored out of R_g, the rest left to influence, k_f — a quantity related to the aggregate geometry, but as yet has no discernible meaning — via the intercept term $\mathbf{c} \propto k_f/\alpha_0^{D_f}$,

$$\frac{\mathbf{d} \log N_s}{\mathbf{d} \log R_g} = D_f \tag{3.37}$$

Immediately one ought to be able to recognise that linear clusters will have a D_f of ≈ 1, bilayer, or lamellar structures will have D_f of ≈ 2, approximately spherical clusters and branched networks will have a D_f of ≈ 3, presumably (but not necessarily) with different fractal pre-factor k_f. Where D_f takes integer values, perhaps with the exception of a branching network, the system can be rationally interpreted as having relatively simple geometry. Where D_f takes non-integer values, the geometry is more difficult to rationalise. Dimensionality close to integer values means the proximal dimension dominates. This means that a system that is composed of 1D strips that have some curvature in their long axis will have *fractional* D_f. If that curvature lies in 1 additional dimension, D_f lies in $(1, 2)$, if it lies in 2 additional dimensions, the cluster system will have $2 < D_f < 3$. A system that possesses some 2D structure that bends will have $2 < D_f < 3$. Though these structures may have non-integer D_f, this does not necessarily imply they are fractals in the sense most familiar to us.

Orientation

A global orientation order distribution is calculated over the system by taking the cosine of the angle between all $\vec{u}_i$ over all pairs ij over the whole system. This particular metric is employed to analyse the global alignment (parallel and anti-parallel) of the set $\{\vec{u}_i\}$ characteristic of a lamellar phase. It is defined as

$$P(u_i \cdot u_j) = \langle cos(\theta_{ij}) \rangle \tag{3.38}$$

Three interrelated metrics are employed to explore the variation in orientations with respect to the centroid and other members of a given cluster [55]. These metrics are employed to categorise finite clusters (i.e. non-percolated) observed over the α range. The metric $\mathcal{M}$ (Equation 3.39) quantifies the sphericity of a micellar aggregate, such that a cluster with $\mathcal{M} \approx 1$ has an approximately spherical shape. $\mathcal{M}$ is defined as

$$\mathcal{M} = \frac{1}{N_s} \sum_{i=1}^{N_s} \cos\theta_i, \tag{3.39}$$

where the cosine of θ_i is defined as the relative orientation of the dumbbell i's unit vector $\vec{u}_i$ to the vector connecting it to the centroid:

$$\cos\theta_i = \vec{u}_i \cdot \frac{C_c - \vec{r}_i}{|C_c - \vec{r}_i|}. \tag{3.40}$$

The metric $\mathcal{B}$ is defined as the average correlation of the orientations of $\vec{u}_i$ within a cluster. $\mathcal{B}$ is unity when all $\vec{u}_i$ are either parallel or anti-parallel and low with uncorrelated orientations, so gives us a measure of the planarity of a cluster:

$$\mathcal{B} = \frac{2}{N_s(N_s - 1)} \sum_{ij} (\vec{u}_i \cdot \vec{u}_j)^2, \tag{3.41}$$

And finally $\mathcal{V}$ defined also by the orientation of each $\vec{u}_i$ with respect to the vector joining it to the centroid, but is unit when each $\vec{u}_i$ are normal to the vector joining the centroid to the dumbbell:

$$\mathcal{V} = \frac{1}{N_s} \sum_{i=1}^{N_s} (1 - \sin\theta_i). \tag{3.42}$$

Metrics $\mathcal{M}$ and $\mathcal{V}$ can be split to categorise aggregates based upon where in the $\mathcal{MV}$ plane they lie [55]. The authors define borders delineating the geometry of aggregates: regions containing purely spherical micelles, where $\mathcal{M} \gtrsim 0.9$; and elongated micelles where $0.5 \lesssim \mathcal{M} \lesssim 0.9$; for all $\mathcal{V}$. Where $\mathcal{M} \lesssim 0.5$, the $\mathcal{V}$ space is split into three regions: where $\mathcal{V} \lesssim 0.3$, a region containing bilayers and elongated micelles exists; where $0.3 \lesssim \mathcal{V} \lesssim 0.5$ containing liquid droplets and faceted polyhedra; and $\mathcal{V} \gtrsim 0.5$ containing vesicles. These metrics will find application in Chapter 6 where the properties of self assembled structures are discussed.

Chapter 4

Dumbbells: Square-well to Janus with $\alpha = 1.0$

This chapter is paraphrased from a paper published in collaboration [57]. The contributors to the simulation work included myself (NPT simulations: Equations of state, Energy per particle; and metric calculations: radial distribution functions, orientation order parameter $P(\vec{u}_i \cdot \vec{u}_j)$, bond-wise distributions of rotationally invariant bond parameter q_6), and Gianmarco Munaò (SUS simulations: $P(N)$ and $P(\rho)$, calculations, critical parameter estimation, vapour-liquid phase diagrams, number of bonds per particle distributions, and structure factor determination). Achille Giacometti contributed results from a mean field approximation to the particle interaction to calculate variation in the critical temperature, T_c^*, with respect to the interaction energy, ε_h. The simulation method employed here does not make use of the AVBMC algorithm, only VMC simulations were perfromed.

4.1 Parameterisation

This chapter contains a study of prototype dumbbell colloids, in order to investigate how the interplay between steric effects, due to particle geometry, and the asymmetry in attractive interactions influences the overall appearance of the fluid phase diagram. A class of dumbbell models is studied, initially formed by two identical tangent hard spheres (i.e. $\sigma_s = \sigma_h = 1$), each surrounded by an attractive square-well with an interaction range fixed at half the hard-core diameter ($\lambda_s = \lambda_h = 0.5$). The interaction strength on one sphere is then reduced until only the bare hard-core repulsion remains. We document how the features of the gas-liquid phase separation depend sensitively on the interaction anisotropy, map the onset of self-assembled phases, characterise the assemblies, and identify the regions of the parameter space where ‘competition’ between self-assembled structures and conventional gas-liquid phase separation occurs.

Potential Definition

For the purposes of this investigation the potential is defined slightly differently to that defined in Equation 2.2. We again distinguish between the two interaction sites on sub-particles h and s except that now the h, sub-particle bears an attractive SW interaction. We are then able to *tune* the interaction strength on h to yield intermediate potential anisotropies along the ε_h parameter. The interaction distance parameter λ is fixed at 0.5 for both spheres and defined by Equation 2.1.1. The set of ε_h studied here are $\{1, 0.7, 0.5, 0.3, 0.2, 0.15, 0.10, 0.05, 0.025, 0\}$. Particular attention has been paid to the cases $\varepsilon_h = 0.5$, 0.1, and 0, as qualitatively representative of the diversity in observed phase behaviours.

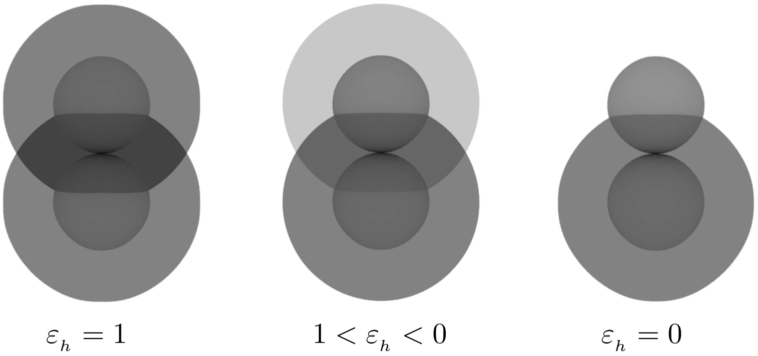

FIGURE 4.1: Variation in the appearance of dumbbell particle with ε_h on the interval [1,0]. The darker region around the equator where $\varepsilon > 0$ denotes a region where both potentials are active. As $\varepsilon_h \to 0$, the particle becomes more like the Janus dumbbell, possessing in increasingly asymmetric interaction potential.

4.2 SUS: Square-well Toward Janus

Selected density distribution probabilities $P(\rho)$, as obtained by SUS simulations, are reported in Figure 4.2 for several values of ε_h.Specifically, the probabilities correspond to the temperatures whereby $P(\rho)$ first displays a double-peak behaviour, providing indication on the position of critical points. In all simulations a box length of $L_{box} = 13.57\sigma$ is used except for $\varepsilon_h = 0.1$, for which $L_{box} = 20\sigma$. The gas-liquid coexistence curves are reported in Figure 4.3.

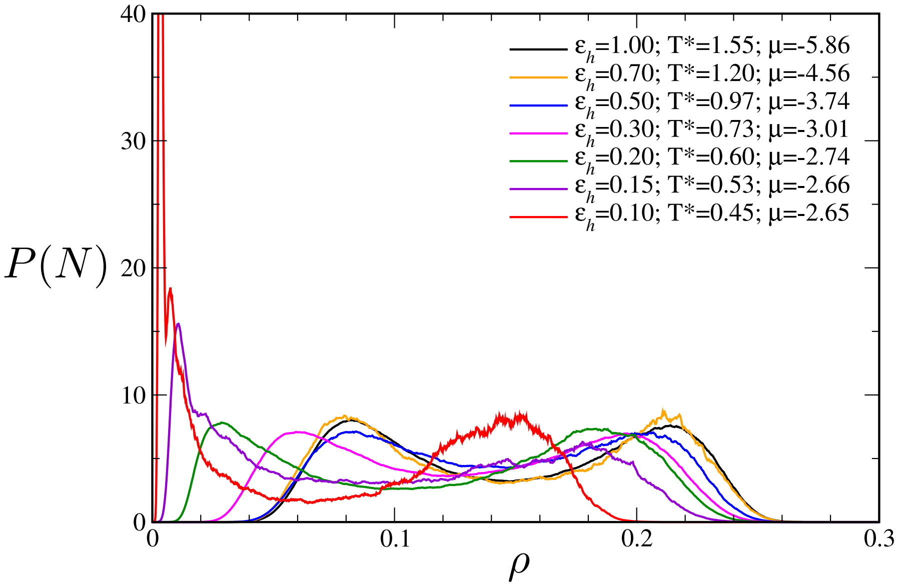

FIGURE 4.2: Probability of a given density $P(\rho^*)$ as a function of ρ^* obtained by SUS with histogram reweighting, just below the critical temperature for each value of ε_h. The corresponding ε_h, T^*, and μ inset.

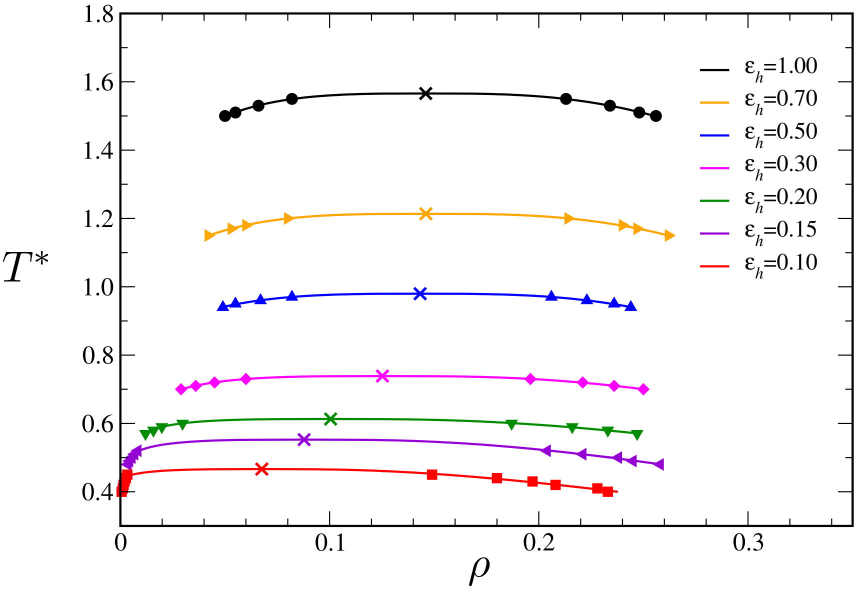

FIGURE 4.3: The binodal curves for each ε_h. The progression of the gas branch to increasingly lower densities at a greater rate than the liquid branch causes the binodal to appear skewed for $\varepsilon_h < 0.3$.

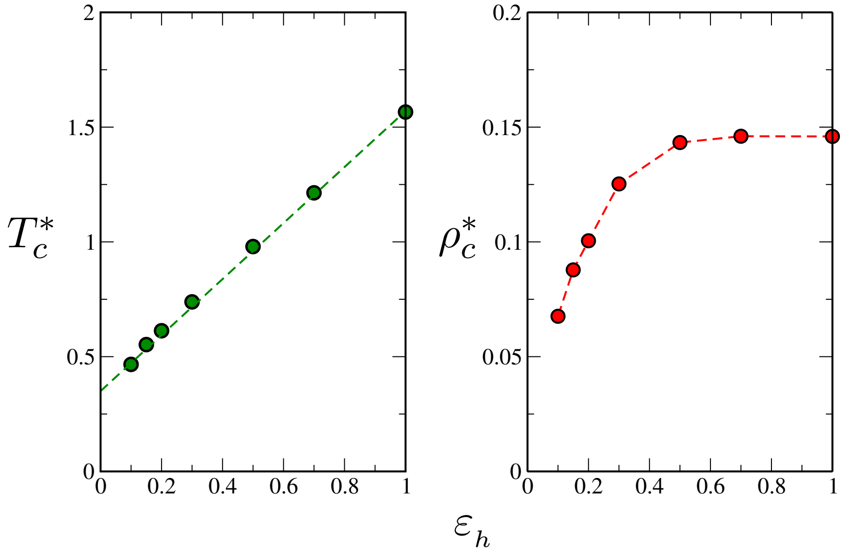

FIGURE 4.4: (a) The critical density ρ_c^* and (b) the critical temperature T_c^* as a function of ε_h. Extrapolating a linear fit to T_c^* indicates a approximate value for the Janus dumbbell of 0.35. The trend in ρ_c^* is less conclusive.

Critical parameters

Critical temperatures, T_c^*, and densities, ρ_c^*, as functions of ε_h, are shown in Figure 4.4. The critical temperature decreases approximately linearly with ε_h, . The critical density stays almost constant ($\rho_c^* \approx 0.15$) for high values of the interaction strength, with a rapid decrease for lower values, as signalled by the "knee" at $\varepsilon_h = 0.5$ Figure 4.3 documents how the observed decrease of ρ_c^* for $\varepsilon_h < 0.5$ is due to a progressive shift of the gas branch of the coexistence curve towards lower densities. This progression is not accompanied by a corresponding shift in the liquid branch. As a consequence, the binodal curve appears skewed, losing the symmetry observed for $\varepsilon_h \gtrsim 0.3$.

On a relatively large interval of ε_h values $\varepsilon_h > 0.1$ the system behaves as a standard "simple fluid" with a supercritical state at high temperatures giving way, on decreasing the temperature past the critical point, to typical gas-liquid phase separation. Figure 4.5 demonstrates this particular (conventional) scenario. Around $\varepsilon_h = 0.1$ the phase diagram changes. A focus on the properties of the system regarding the case $\varepsilon_h = 0.1$ is given in Figure 4.2. The probability distribution of the number of particles $P(N)$ at $T^* = 0.45$ and two different simulation box sizes. The two main peaks visible in the figure testify the existence of stable gas and liquid phases, with corresponding critical point at $T_c^* = 0.47$. Notice that the position of the gas peak in $P(N)$ is shifted toward extremely low values of N, indicating a rather low gas density. Beside the gas and liquid peaks, $P(N)$ in Figure 4.6 is now characterised by the appearance of a third peak (see also the magnification in the inset) which does not scale with the box size. This feature

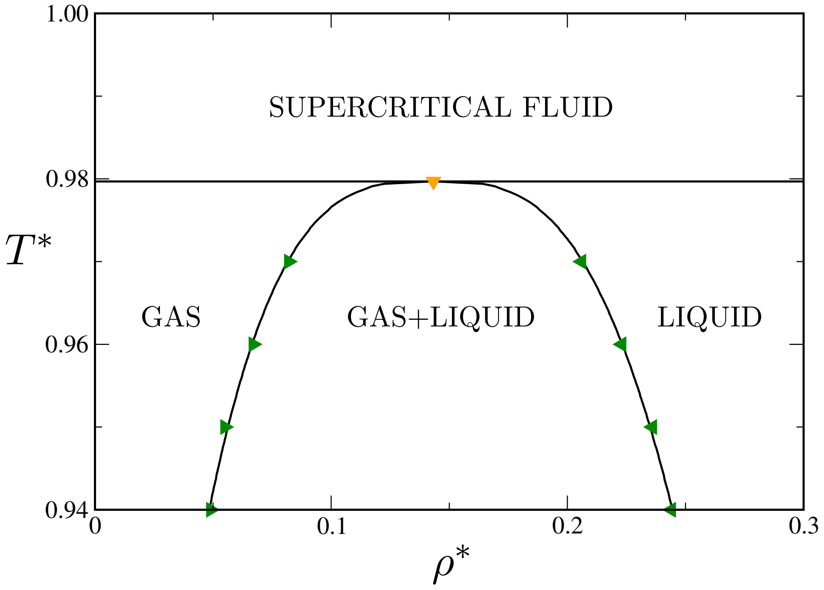

FIGURE 4.5: Conventional simple liquid phase diagram for ε_h with critical parameters $T^*_c \approx 0.9797$ and $\rho^*_c \approx 0.14327$ indicated by the orange triangle. The green triangles correspond to data-points obtained by SUS and the fitting (black line) quantifies the density of the co-existing gas and liquid.

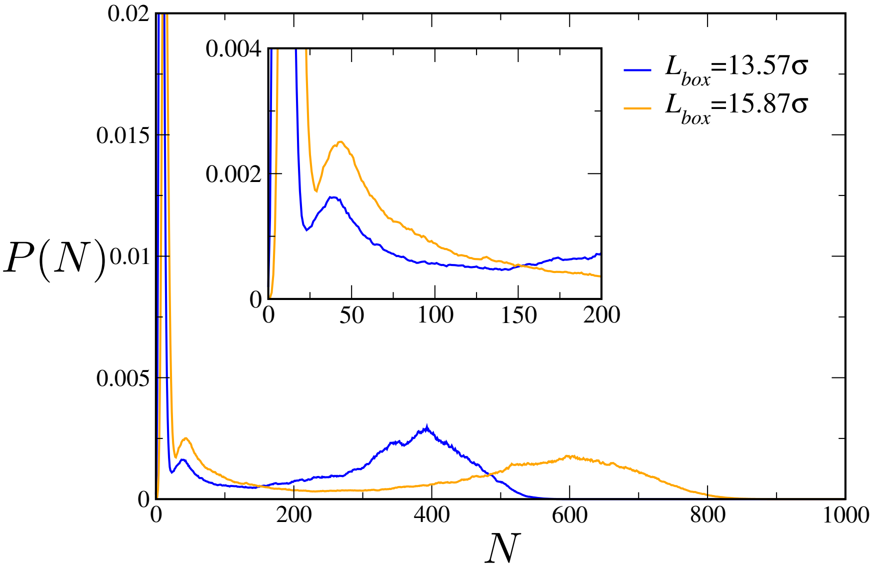

FIGURE 4.6: Accounting for finite-size effects. Two separate SUS simulations of particle systems with $\varepsilon_h = 0.1$ at $T^* = 0.45$ with different L_{box} lengths.

signals the presence of aggregates (micelles) in the low density regime of the fluid. Analysis of these configurations shows that micelles grow in the form of roughly spherical clusters of around ten particles.

The presence of spontaneously formed aggregates is observed over a temperature range extending down to the lowest temperature investigated for this case ($T^* = 0.36$), albeit

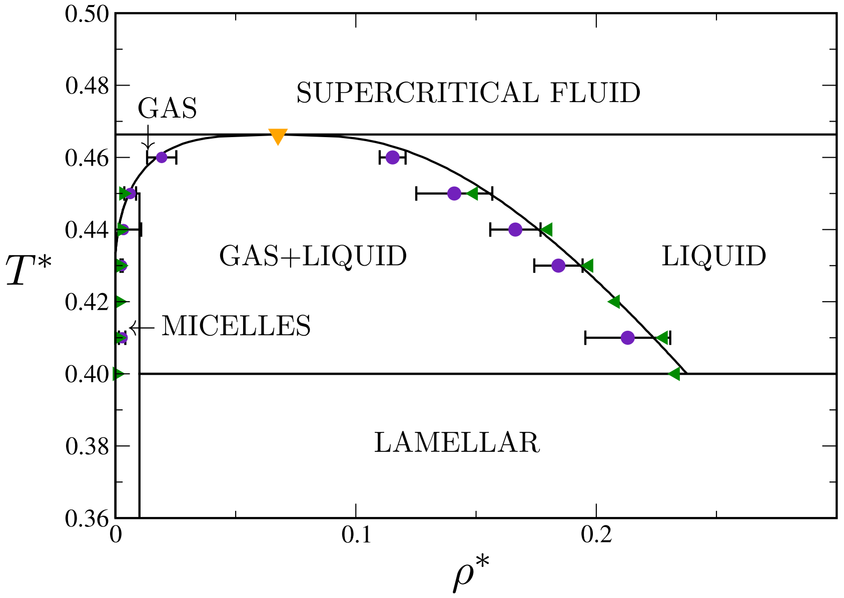

FIGURE 4.7: Unusual liquid phase diagram for $\varepsilon_h = 0.1$ with critical parameters $T_c^* \approx 0.4664$ and $\rho_c^* \approx 0.0676$ indicated by the large orange triangle atop the coexistence curve. The green triangles astride the co-existence region correspond to data-points obtained by SUS and the fitting (curved black line) obtained using the law of rectilinear diameters. The purple points correspond to points obtained from NPT simulations extrapolating the liquid and gas branches from equations of state to their corresponding approximate coexistence pressures via Maxwell construction.

confined to a narrow (low) density interval. When aggregation takes place, finite size effects become relevant and the SUS data is scrutinised assiduously. The micelle peak behaves rather strangely compared to liquid and gas peaks conventionally observed in SUS simulation. The micelle peak falls at the same number of particles independent of the simulation box size. When a larger simulation box is employed the positions of peaks corresponding to the gas and liquid phases in the $P(N)$ vs. N diagram shift, rendering their respective densities constant. By contrast, the micelle peak remains around the $N = 10$. Within a $P(\rho)$ vs. ρ representation, the gas and liquid peaks maintain the same positions, whereas the micelles peak shift toward lower densities (on increasing L_{box}). The formation of these micelles occurs at comparatively low temperature and low densities. At low temperatures ($T^* = 0.40$) and larger densities, visual inspection of system configurations reveals that molecules arrange into planar structures (lamellae) extending until the highest density value investigated (i.e. $\rho^* = 0.3$).

4.3 Isobaric - Isothermal Ensemble Study

The peculiar features emerging from the SUS simulations where interaction strength $\varepsilon_h \leqslant 0.1$ call for a more detailed analysis of structural and thermodynamic properties of the system. Monte Carlo simulations in the NPT ensemble are reported in Figure 4.8 for

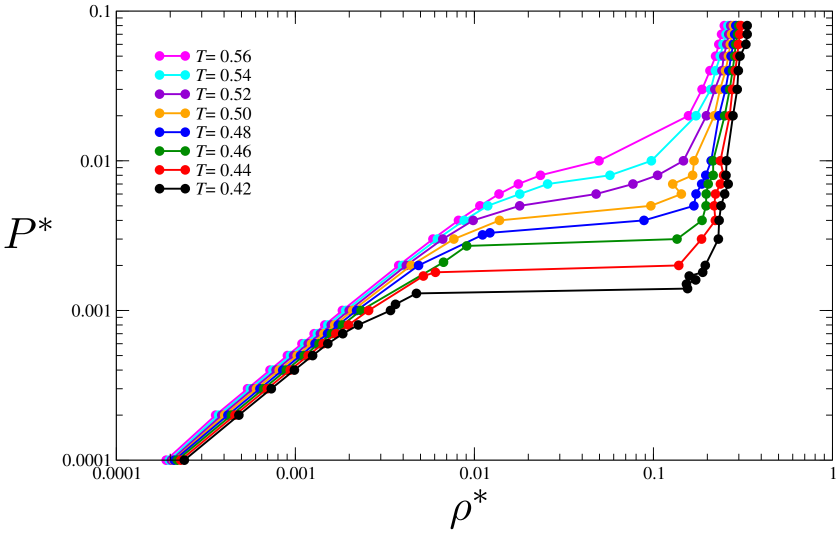

FIGURE 4.8: Equations of state in the P^*–ρ^* plane. A discontinuity in the density can be resolved from considering the slope of the EOS curve

several temperatures, the equation of state in the P^*–ρ^* plane. For $0.41 < T^* < 0.48$, sub-critical phenomena can be resolved, showing a discontinuity in the density, while for $T^* = 0.48$ a continuous transition is observed. The corresponding density discontinuity appears to reduce in magnitude upon increasing the temperature, until just below the estimated critical temperature $T^* \approx 0.4664$.

The energy per particle in Figure 4.9, observed for pressures where the density deviates markedly from ideality (for $T^* = 0.42$), but below the density transition, indicates the onset of a particle association process. The onset of a lamellar phase for $P^* > 0.06$ at $T^* < 0.41$ is seen here by a marginally lower energy per particle. In spite of having a comparatively low energy and the clustering process taking shape here, we have observed no anomalous behaviour akin to that of spherical Janus colloids, where, for instance, the gas-liquid coexistence curve turns out to be negatively sloped in the temperature-pressure plane [29, 35]. The condensation process occurs without hindrance from comparatively stable clusters, due to the fact that these latter do not take on well defined *hard* surface morphologies, i.e. with the strongly interacting spheres facing inward. This contrasts with the Janus sphere case, where the angular dependence of a favourable interaction (defined by the Kern-Frenkel potential) promotes the orientation of the hard interaction outward, effectively rendering each cluster-cluster interaction rigid enough to prevent cluster merging processes, until the system is dense enough to percolate and either form lamellae, or a liquid.

Coexistence densities (purple squares on Figure 4.7) are obtained by Maxwell construction on the equation of state data. Specifically, the slope of the ultimate three points from either side of the transition at the corresponding temperatures are calculated and

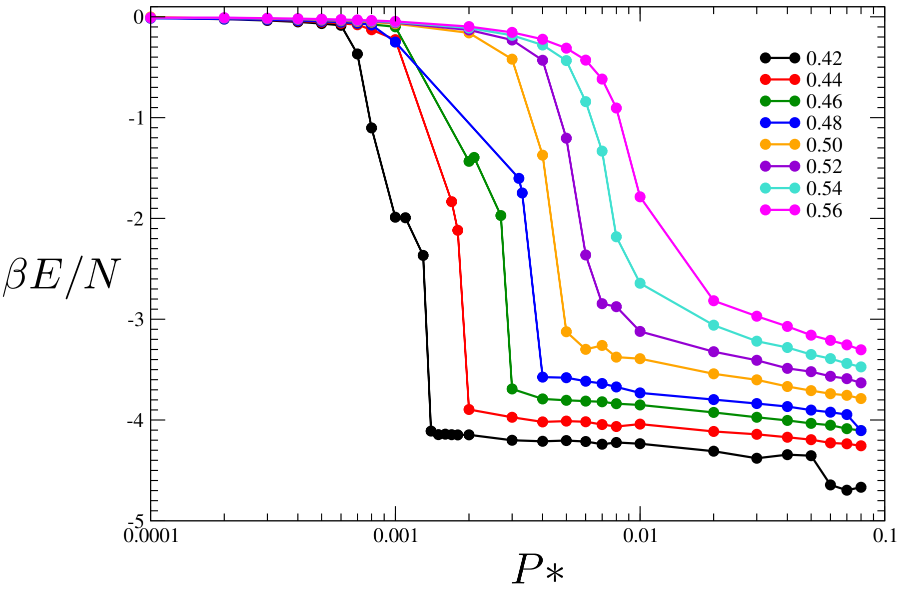

FIGURE 4.9

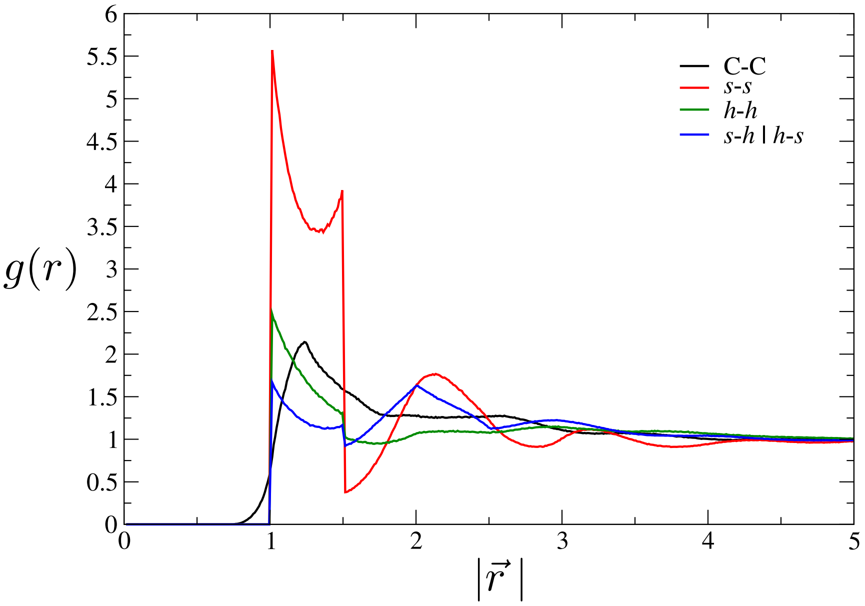

FIGURE 4.10: Site-site and centroid (C–C) radial distribution functions for a liquid approximately at the coexistence density at $T^* = 0.42$. Legend refers to interaction sites over which the distributions are calculated.

straight lines projected to a point where the pressure is equal. Error bars correspond to the average distance between density at the projected coexistence pressure and last MC data point on the respective gas and liquid branches with the projected point corresponding to the pressure of the final data point of the other side of the transition. As demonstrated, NPT estimates satisfactorily agree with SUS calculations.

4.3.1 Liquid Structure

Typical liquid site-site radial distribution functions $g(r)$, showing the preferential interaction of sites s–s and h–h are reported in Figure 4.10. The s–s peak shows a slight preference for bond lengths to occupy the inner-most and outer-most extents of the interaction range λ. The comparatively lower curve representing the h–h interaction can be attributed to the relative larger binding energy of the s–s interaction. The second, almost discontinuous peak of the h–h curve around $r = 2s$ would seemingly imply a preference for a significant proportion of the particles to be with sites h at 180 degrees to each other, as is expected for lamellar, sphero-symmetric vesicular aggregates.

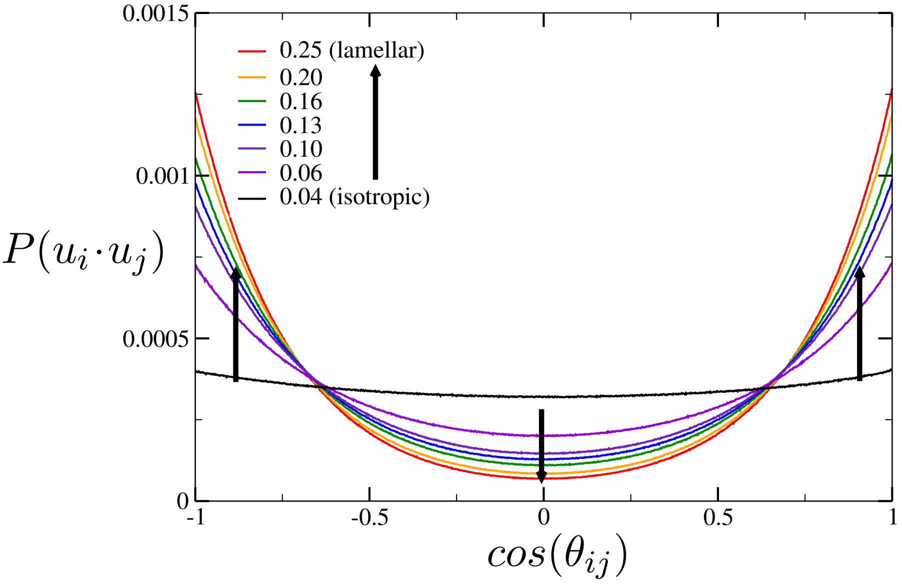

FIGURE 4.11: Probability of finding a pair of particles with $u_i \cdot u_j = cos(\theta_{ij})$, the progression to higher P^* (legend inset), and causes the distribution to indicate the alignment of particle unit vectors into either parallel or anti-parallel configurations as the system displays more lamellar character.

The orientational order parameter $P(u_i \cdot u_j)$ is shown in Figure 4.11. Data contained therein concern $P(u_i \cdot u_j)$ as calculated at $T^* = 0.42$ and increasing pressure; a normalisation factor has been employed to make the total integral under the curves unity, with 1024 bins for the distribution. As visible, where $0.04 < P^* < 0.06$ the system has already started to display lamellar character. Increasing the pressure causes the lamellar structure to become more defined and the distribution to appear increasingly quartic. No observation of a global alignment in the unit vectors was found for regions of the density space containing micelles. The reason for this is twofold: firstly, there is no correlation between the orientation of particles in different clusters as they do not communicate through a planarity imposed by adjacent lamellar structures; secondly, as the interaction potential does not have an angular component, the favourable energetic configuration between any two particles can be maintained without the requirement of a certain alignment; rather the two bonded particles have only a very small restricted space of mutual orientations (their comparatively hard components cannot themselves overlap).It is expected that a study of the radial dependence of $P(u_i \cdot u_j)$ (not carried out here) should allow the observation of some structure, as particles with distance $r \approx \langle D_m \rangle$ (where $\langle D_m \rangle$ is the average diameter of a micelle), will tend to have an opposing orientation leading to a strong peak around $\langle D_m \rangle$, and likely a weaker peak at $\langle r_c \rangle$, with $\langle r \rangle$ the average distance between clusters.

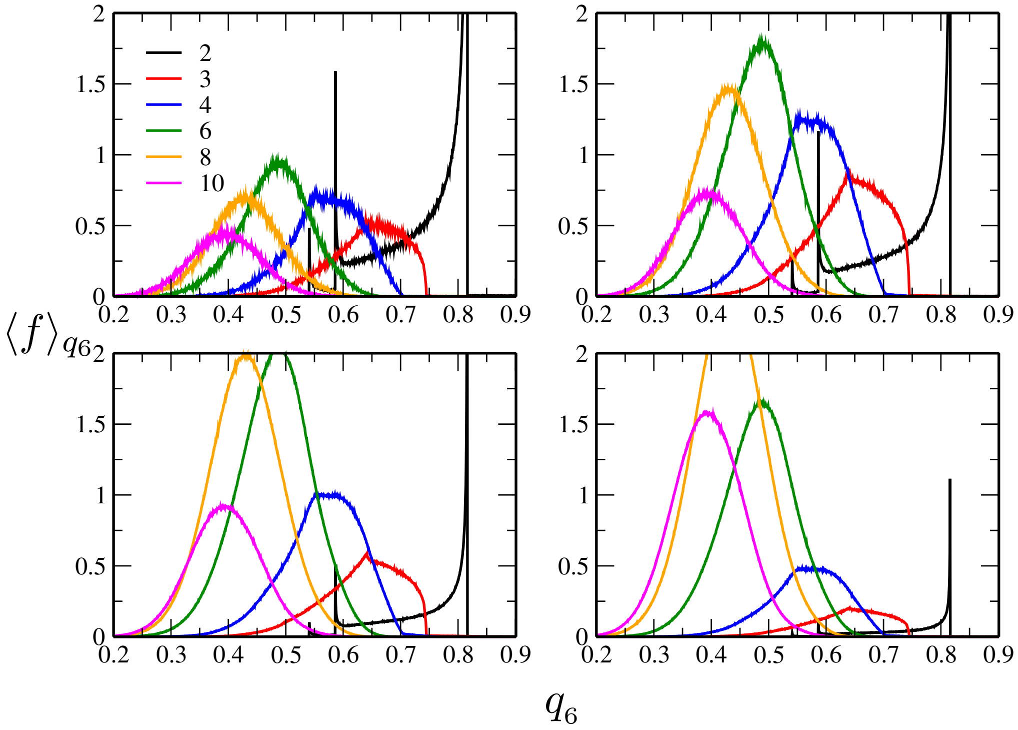

FIGURE 4.12: Distributions of local bond-orientation order parameter q_6. Left-most distributions obtained from $T^* = 0.42$ at $\rho^* = 0.001$ (top) and $\rho^* = 0.22$ (bottom). Right-most distributions obtained from $T^* = 0.46$ at $\rho^* = 0.009$ (top) and $\rho^* = 0.12$ (bottom). The scale refers to a normalised frequency of observation. Structures at low N_b reflect persistent structures formed in both the gas and liquid phases.

Figure 4.12 shows the local rotationally invariant bonding environment order parameter q_6 defined by Equation 3.30 employed here to probe the dependence of bond orientations on the interaction potential, as well as accounting for the influence of the presence of the hard sphere on bonding environments, in both micelles and the liquid phase. We have considered only bonds of the s–s interactions in the calculation of this metric. Distributions in the figure show well defined structures for particles which make relatively few bonds. The three peaks in the $N_b = 2$ distribution at 0.8135, 0.583 and 0.538 (most clear in the gas phase distributions) correspond to different bonding environments. In the first case the angle between bonds (made by particle i to each of its two neighbours

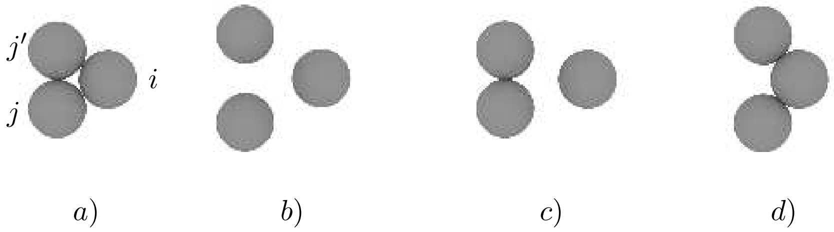

FIGURE 4.13: Structures of local bond orientations as measured by rotationally invariant order parameter distributions on the bonding networks of the *s* spheres. Equilateral triangle environments a) and b) correspond to the peak at 0.8135, the isosceles triangle in c) corresponds to the peak at 0.583, and d) to the peak at 0.538. As the system becomes more dense the steric effect of the presence lamellar structures in the liquid suppresses such as these. The index scheme referred to in the text is indicated in panel *a*) and carried through the image.

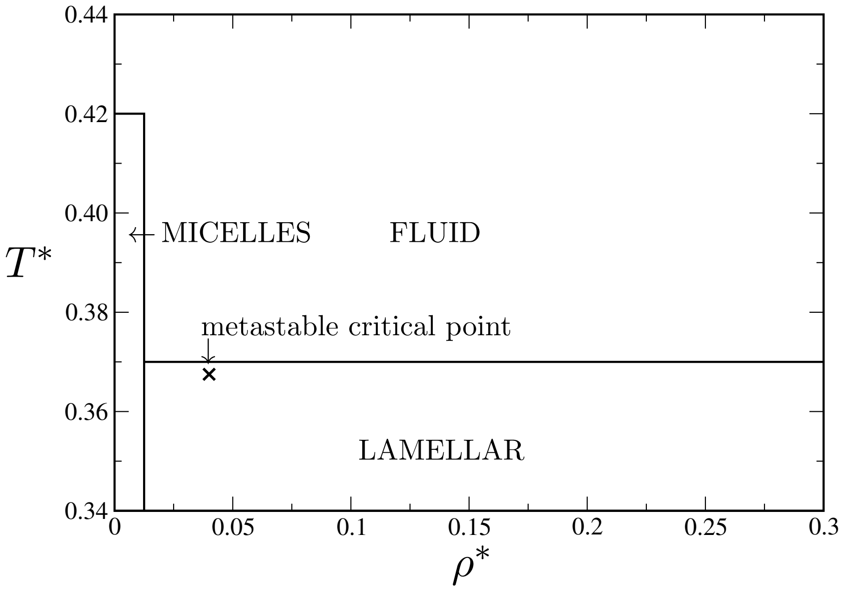

FIGURE 4.14: The phase diagram for $\varepsilon_h = 0.025$ demonstrating an empty liquid scenario. Here the formation of lamellar aggregates occurs at a higher temperature than the projected metastable gas-liquid critical point.

j and j') corresponds to $\pi/3$ radians, i.e. an equilateral triangle with $r_{ij} = r_{ij'} = r_{jj'}$ is formed, panel *a*) in Figure 4.13; the second case, 0.6797 radians, corresponds to an isosceles triangle with $r_{ij} = r_{ij'} = \sigma + \lambda\sigma$ and $r_{jj'} = \sigma$; the third case, 1.6961 radians, corresponds to $r_{ij} = r_{ij'} = \sigma$ and $r_{jj'} = \lambda\sigma$. The end of the distribution indicates particles whose neighbours number three corresponds to an equilateral triangle based pyramid whose tip, mutually at the furthest extent of the interaction range, is the particle i. Where the number of bonds is greater than four, the ability to easily detect a potential dependence ceases, and no more fine detail can be obtained directly from the distributions of q_6 , except for the distribution of numbers of bonds per particle.

Upon approaching the Janus dumbbell case, i.e. as $\varepsilon \to 0$, a third different phase scenario arises, as exemplified in Figure 4.14 for the case $\varepsilon = 0.025$. At relatively high temperatures ($T* = 0.42$), the system remains in a homogeneous fluid phase. On lowering the temperature a micellisation process occurs at low density. As the temperature is further decreased, below $T^* = 0.38$, the formation of bilayer sheets (lamellae) is observed.

4.3.2 Extrapolation of Critical Parameters to $\varepsilon_h = 0$

The extrapolation of the critical temperature, reported in Figure 4.4, leads to the prediction of a hypothetical critical temperature $T_c^* \approx 0.37$ for $\varepsilon_h = 0.025$, and marginally lower for Janus dumbbells (where $\varepsilon_h = 0$). The phase diagram of Figure 4.14 also indicates that the formation of lamellar aggregates pre-empts the gas-liquid phase separation, implying the metastability (and possibly the absence) of a corresponding critical point. The presence of the micelle phase in phase diagrams computed for $\varepsilon < 0.10$ may be result of suppressed diffusive modes of the constituent micellar aggregates. While this possibility was not explored here, some data at nearby points parameter space will be discussed in the next chapter.

Chapter 5

Janus Dumbbell Liquids Over the Range $1 < \alpha < 2$

In a similar spirit to the study summarised in Chapter 4, SUS simulations over the range of the size asymmetry parameter α are employed to document the variation in critical phenomena. The location of self-assembled structures are identified and characterised. The development of self-assembled phases, where the system size required to organise the self assembled phases render the SUS technique as implemented inadequate to characterise the systems encountered. Those particular state-points are treated in Chapter 6. Nevertheless, self-assembled structures encountered using the SUS technique are treated carefully so as to ensure, to a best approximation, that they are characterised properly with respect to their competition or coexistence with more typical critical phenomena. This chapter proceeds by summarising a paper [80] published in 2015, for which the Author of this thesis was a main contributor.

5.1 Evidence of Clustering and Liquid Formation of Heterogeneous Janus Dumbbells

Provisional exploration of what hereafter shall be referred to as the Heterogeneous Janus Dumbbells (HJD) in the space surrounding the case of equal sized sub-particles, i.e. $\sigma_s = \sigma_h$. The heterogeneity referred to henceforth is that of the parameter α which determines the size ratio between composite spheres. There is some evidence that in the region around $\alpha > 1$ that the formation of a liquid and the self-assembly of clusters and layered structures may compete [80]. Here we consider structure factors (obtained by collaborator Gianmarco Munaò), $S(k)_{ss}$, (structure factor over solely the s sub-particles)

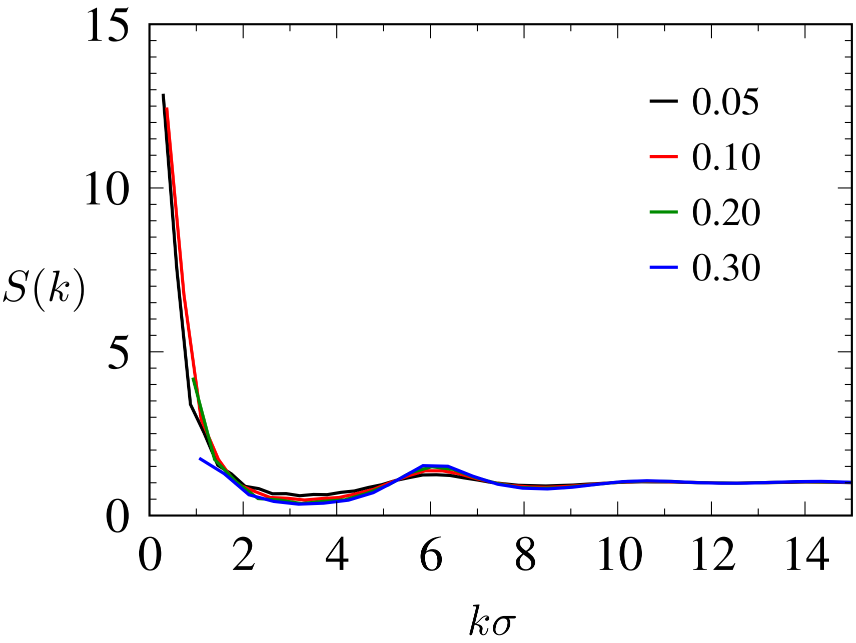

FIGURE 5.1: $S(k)_{ss}$ for $\alpha = 3/4$: the divergent with increasing ρ^* of the low k peak indicates a region where a phase-separation is likely to take place. the density is indicated in the legend inset.

employed to differentially diagnose the presence of clusters and condensed phases in NVT simulations of 1000 HJDs for $\alpha \in 0.75, 1.10, 1.25$. It has been demonstrated elsewhere that the presence of a low k peak can indicate the location of a clustering process in experiment [81, 82] and theoretically [83–85]. It is suggested that the presence of a low k peak that diverges under compression indicates a region where clustering co-exists or competes with condensation. If the low k peak resolves, the formation of a liquid is suppressed.

Figure 5.1 depicts $S(k)_{ss}$ for $\alpha = 1.25$. As the low k peak here diverges early, the presence of a phase separation is inferred. As α is decreased further to 1.1, (Figure 5.2) the presence of a low k peak that diverges suggests an isotherm where clustering and phase-separation may compete. Figure 5.3 depicts $S(k)_{ss}$ for $\alpha = 3/4$. As the system ρ^* is increased the low k peak resolves, indicating that the formation of a liquid is suppressed by a clustering process. This region will be examined in more detail in Chapter 6. Since we have computed the phase diagram for points approaching the Janus dumbbell limit ($\alpha = 1$) (see Chapter 4) where only low ρ^* self-assembled micelles and high ρ^* lamellar phases are observed, we expect that somewhere in the region $1 < \alpha < 1.4$ a gas-liquid phase-separation critical point becomes metastable with respect to the formation of self-assembled bilayer structures. This behaviour suggest that in a similar fashion to the study in Chapter 4 the phase-separation region terminates before $\alpha = 1$, the Janus limit. The process by which this occurs in unclear. These data indicate the general regions of the α space where only gas-liquid phase-separation is likely to be observed

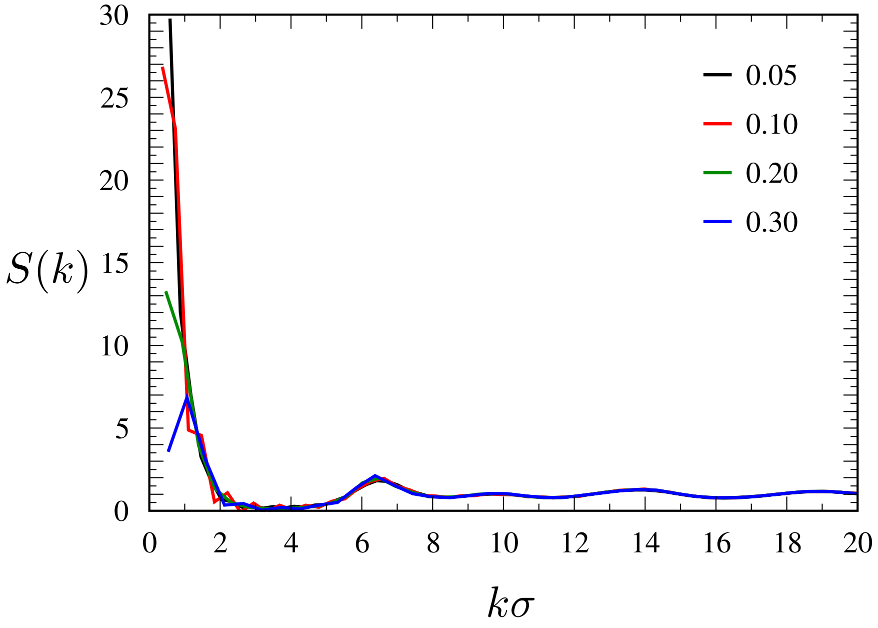

FIGURE 5.2: $S(k)_{ss}$ for $\alpha = 1.1$: a low k peak that diverges indicates a region where cluster formation and phase-separation may take place.

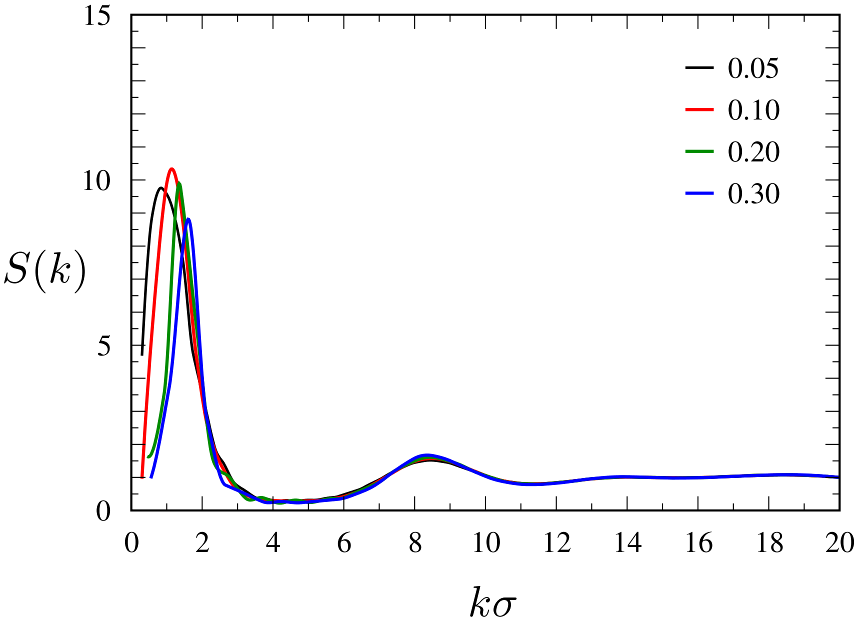

FIGURE 5.3: $S(k)_{ss}$ for $\alpha = 3/4$: relatively constant low k peak indicates a cluster forming region.

$\alpha \gtrsim 1.25$, where solely a clustering process occurs $\alpha < 1.1$, and where a clustering process and phase-separation may compete $1.1 \leqslant \alpha \leqslant 1.25$. This chapter contains a closer examination of the phase-separation dominated region where $\alpha > 1$.

5.2 Calculation of the Second Virial Coefficient $\mathbf{B_2}$

To guide the exploration of the α space as regards the variation in critical temperature, computation of the second virial coefficient, B_2, can be performed to identify the Boyle temperature, $T_{\mathcal{B}}$, below which the pair-wise attractive interactions begins to play an important role in the phase behaviour, as well as quantifying the excluded volume effects. $T_{\mathcal{B}}$ is defined as

$$T_{\mathcal{B}} \equiv T(B_2 = 0). \tag{5.1}$$

The second virial coefficient can be estimated a number of ways. Here we compute the Mayer f-function over a large number of randomly generated configurations of pairs of HJD particles [86]. The Mayer f-function is defined by

$$f_{12} \equiv e^{-\beta \mathcal{U}(\vec{\mathbf{r}})} - 1. \tag{5.2}$$

Computing the Mayer function for the dumbbell particle is a little unintuitive. The assessment of the right hand side of Equation 5.2 for a given particle pair must be performed site-wise such that for $\sigma_s \neq 0$ and $\sigma_h \neq 0$ the function f_{12}, where the subscript indicates particles 1 and 2 is calculated by

$$f_{12} = (e^{-\beta \mathcal{U}(\vec{\mathbf{r}}_{ss})} \times e^{-\beta \mathcal{U}(\vec{\mathbf{r}}_{sh})} \times e^{-\beta \mathcal{U}(\vec{\mathbf{r}}_{hs})} \times e^{-\beta \mathcal{U}(\vec{\mathbf{r}}_{hh})}) - 1. \tag{5.3}$$

Where the site on each particle is indicated by the subscript on $\vec{\mathbf{r}}$. For the endpoints of α where either diameter σ_h or σ_s are naught, where there exists only a single site, f_{12} is computed by either

$$f_{12} = e^{-\beta \mathcal{U}(\vec{\mathbf{r}}_{ss})} - 1 \qquad \text{or} \qquad f_{12} = e^{-\beta \mathcal{U}(\vec{\mathbf{r}}_{hh})} - 1. \tag{5.4}$$

Performing 10^8 placements of two particles in a cubic box of length L_{box} and summing the computed values of f_{12}, the values of the Mayer function over these configurations and subsequently averaging Equation 5.3 over these N_c configurations yields an estimate of B_2 by

$$B_2(\beta\varepsilon) = -\frac{L^3 \sum_{N_c} f_{12}}{2N_c}. \tag{5.5}$$

Calculation of $T_{\mathcal{B}}$ performed at the edges of the α parameter space to ensure agreement with (or convergence toward) the relevant reference points (identified in Section 2.2). A plot of the variation in $T_{\mathcal{B}}$ with α can be found in Figure 5.4. It should be noted here that where $\alpha \to 0$, the contribution to the computation of B_2 from the s site becomes increasingly less likely to occur, implying that excessively long computations are required to accurately ascertain a reasonable estimate here, given the likelihood of generating a configuration with $\mathbf{r}_{ss} < \sigma_s + \lambda\sigma_s$ becomes vanishingly small. The computation only extends as far down as $\alpha = 0.05$ and the assumption made that the point at which the model returns a bare hard-sphere, that $T_B = 0$. This is not an unreasonable assumption since it becomes absurd to talk about temperature of the conventional sort when discussing pure hard-spheres. Figure 5.4 shows the outcome of this calculation over the set of α.

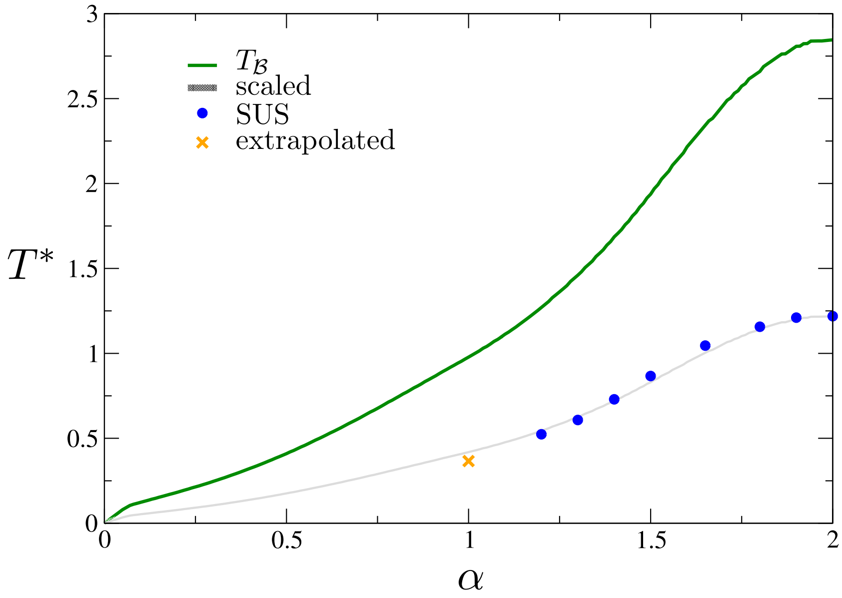

Figure 5.4: Variation in T_B with respect to α. The green line indicates the Boyle Temperature, $T_{\mathcal{B}}$, the temperature at which B_2 is zero, the maximum error indicated by the corona. The grey line indicates the variation in T_B when scaled to meet the calculated SW critical point; blue dots are T_c^* calculated by SUS in this work.

5.3 Liquids

When $T_{\mathcal{B}}$ is scaled to T_c^* of the pure SW system one can recover a crude estimate of the variation in $T_c^*(\alpha)$. This projection guides the exploration of the liquid behaviour for $\alpha < 2$. Beginning at the point where the model returns the SW ($\alpha = 2.0$), SUS simulations are performed to track variations in critical phenomena. Figure 5.4 demonstrates the quality of predictive power of $T_{\mathcal{B}}$ to the critical temperature of the dumbbells at various α observed.

5.3.1 Successive Umbrella Sampling

Successive umbrella sampling simulations of particle systems up to and including 1000 particles are equilibrated at constant volume to optimise $\langle U \rangle$ and system cluster statistics, $\langle N_{mono} \rangle$, $\langle N_c \rangle$ until fluctuations in each of these metrics was consistent with equilibrium at which point GC insertion and deletion moves are employed to populate the histogram edges. Histogram edge ratios are monitored during each simulation to ensure convergence to a stable ratio, such that $H(n+1)/H(n) \approx k \pm 0.001$ (where k is the converged histogram ratio), before the histogram can be compiled utilising Equation 3.24. Once the histograms are compiled a re-weighting technique is applied and the resultant densities of the co-existing gas and liquid, and their relative errors obtained. Figure 5.5 shows a typical (for $\alpha = 1.8$) progression of the output from re-weighted SUS data. At $T^* = 1.15$ the system has begun to display a binodal distribution in the ρ^* space. On lowering the temperature these peaks separate, and the corresponding density can be obtained by averaging over the area under each distribution.

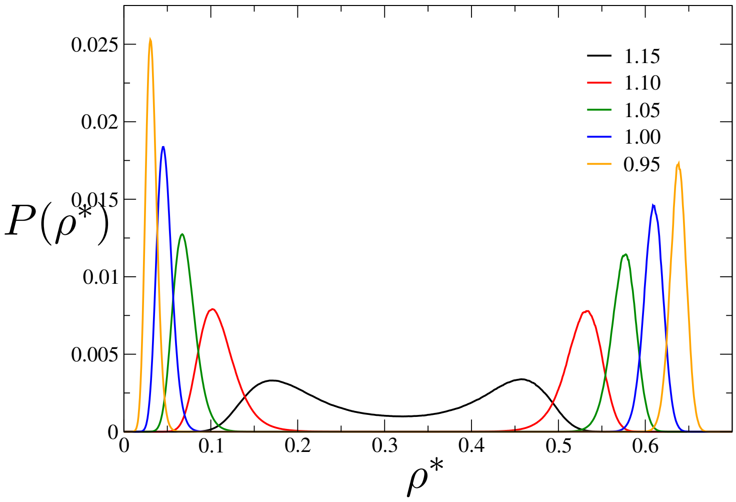

Figure 5.5: Binodal character developing for $\alpha = 1.8$ on lowering the temperature (indicated in the top-right corner) past the critical point ($T_c^* \approx 1.156$).

.

5.4 Gas-liquid Coexistence Curve Construction

Phase diagrams (presented in Chapter 7) are constructed via the determination of co-existing gas and liquid densities from SUS post processing collated with the simulation data from SA AVBMC simulations to categorise the phase behaviour around each state point. Critical values ρ_c and T_c, the system number density and temperature at the critical point, are obtained by fit using a formulation of the law of rectilinear diameters [68],

$$\frac{\rho_l + \rho_g}{2} = \rho_c + A(T - T_c) \tag{5.6}$$

where ρ_l and ρ_g are the average number density of the liquid and gas phases at coexistence, T is the system temperature, and A is a fitting parameter. The density difference at coexistence $\rho_l - \rho_g = \Delta_{l-g}$ is fit using a scaling law,

$$\Delta_{l-g} = B(T - T_c)^{\beta_c}, \tag{5.7}$$

where B is a fitting parameter and β_c, the critical exponent, treated here also as a fitting parameter. Table 5.1 summarises the parameters obtained from the fit. Figure 5.7 shows the variation in the density co-existence curves for $1.2 \leqslant \alpha \leqslant 2.0$.

Phase Separation Data						
Critical Parameters				Fitting Parameters		
α	T_c^*	ρ_c^*	ϕ_c^*	A	B	β_c
2.00	1.2106	0.3132	0.1639	-0.1328	0.9671	0.297 (0.003)
1.90	1.1808	0.3180	0.1667	-0.1103	0.9343	0.259 (0.003)
1.80	1.1566	0.3120	0.1647	-0.1109	0.9450	0.282 (0.001)
1.65	1.0558	0.2967	0.1620	-0.1189	0.9771	0.303 (0.002)
1.50	0.8667	0.2654	0.1563	-0.2055	0.8788	0.243 (0.002)
1.40	0.7295	0.2283	0.1454	-0.3008	0.8932	0.274 (0.002)
1.30	0.6079	0.1847	0.1299	-0.3416	0.8579	0.320 (0.002)
1.20	0.5191	0.1316	0.1076	-0.1518	0.7466	0.42 (0.03)

TABLE 5.1: Summary of critical point fitting parameters obtained from non-linear fitting of the SUS coexistence data.

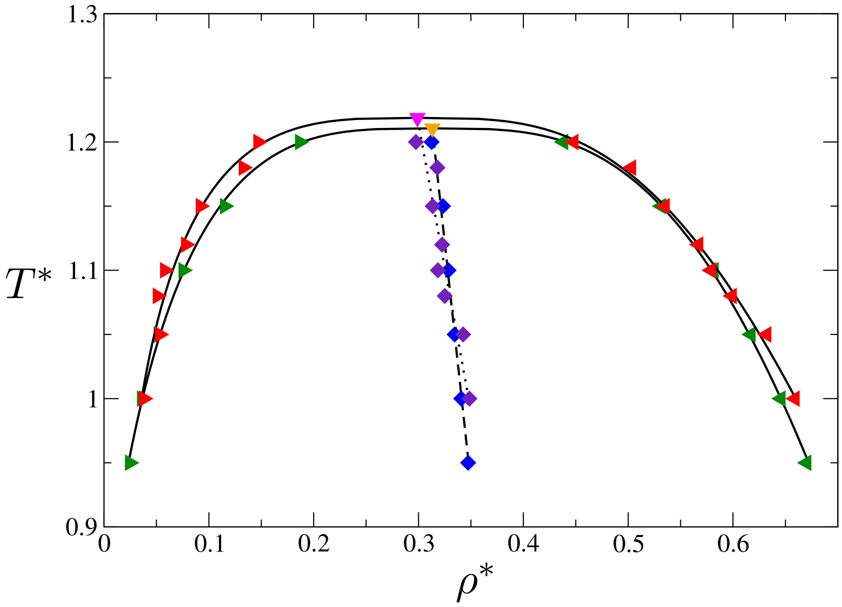

FIGURE 5.6: Comparison between the gas-liquid coexistence curve as calculated by GEMC (red and indigo symbols with magenta critical point) and the SUS method (green and blue symbols with orange critical point). Reasonable agreement between the two estimates is demonstrated, however a small differences in ρ_c^* and T_c^* are observable. More weight can be applied to the SUS technique since it is less prone to systematic error in the density near the critical point.

5.4.1 Gas-Liquid Co-existence

Coexistence Comparison

Figure 5.6 compares coexistence curves for pure s spheres, with $\lambda = 0.5$ obtained both under the current method and that obtained by GEMC in [1] (with data refit according to Equation 5.4 and Equation 5.4). Reasonable agreement between the two methods is observed, with less than 1% difference between estimates of the T_c^*. The deviation in ρ_c^* is closer to 5%, however. The origin of this deviation is unknown. One may speculate that as density fluctuations become larger using the GEMC technique on approach to the critical point, estimation of the coexistence densities may lead to comparatively less reliable data than the SUS technique, which can simulate almost up the critical point, providing the system is sufficiently large to capture enough of the diverging correlation length.

5.4.2 Varying α

Moving from the pure SW scenario, exploring the effect of a swelling h sub-particle, which for values of $\alpha > 1.5$ can fit inside the bonding volume of the s sub-particle, one can observe little difference in the shape of the coexistence curve. The critical temperature beginning at $T_c^* = 1.211(\pm 0.002)$ for $\alpha = 2$, in reasonable agreement with [1], decreases monotonically for $\alpha < 2$. The diminishing volume of the interaction range will limit the coordination number and thus decrease the temperature at which a critical point may be observed. On the other hand, ρ_c^* shows a small increase with respect to the pure phase where $1.8 \leqslant \alpha < 2.0$. This behaviour is discussed further below in Section 5.5. On decreasing α below 1.65 the coexistence curves lose their symmetry, suggesting that they do not belong to the same Ising universality class (consider both the critical exponents recorded in Table 5.1 and the shapes of the curves in Figure 5.7). Where theoretical approaches place critical exponents for 3D systems While both branches between $1.2 < \alpha < 1.5$ shift to significantly lower density, the gas branch does so at a faster rate as can be seen by the increasing slope of $(\rho_l^* + \rho_g^*)/2$. By $\alpha = 1.5$, the gas branch has shot off to a far lower density, in a trend that continues until $\alpha = 1.3$, dragging with it the critical point. For $\alpha \to 1.2$, the decline in ρ_c^* is approximately linear, whereas over the full range of α studied for critical phenomena, the variation in T_c^* appears sigmoidal.

The green points on the right-most panel of Figure 5.8 represents the critical volume fraction ϕ_c^*. This is obtained by multiplying ρ_c^* by the volume of the dumbbell via equation

$$\phi_c^* = \frac{\pi}{6}\left[\sigma_s^3 + \sigma_h^3\right]\rho_c^*. \tag{5.8}$$

As is evident from the plot, the volume fraction possesses a very slight positive slope over the region $2 < \alpha < 1.5$, excepting the small nodule between $2 < \alpha < 1.8$. Where $\alpha < 1.5$, ϕ_c^* decreases more rapidly, until the progression comes to the end of the critical parameters curve as calculated.

5.5 Liquids of Janus Dumbbells

The small increase in ρ_c^* with $1.65 < \alpha < 2.0$ is an unexpected result and warrants some analysis. One may consider, via a simple mean field style argument, that the presence of the h component ought to be interpreted as a reduction in the volume of the potential available for bonding. Adopting this view would lead one to infer a slight decrease in the temperature required to condense a liquid, and that this may be accompanied by an increase in ρ_c^*, like the pure SW liquid on decreasing λ [1]. However, the correction to the density anomaly by $\alpha \approx 1.65$ seems to indicate more than a single contributor to this density variation. To investigate the influence of the growing h sub-particle, simulations of 1000 particles are performed in the canonical ensemble on systems at $T^* < T_c^*$ and liquid $<\rho_{coex}^*>$ across the range $1.4 < \alpha < 2$ to characterise any microscopic variation

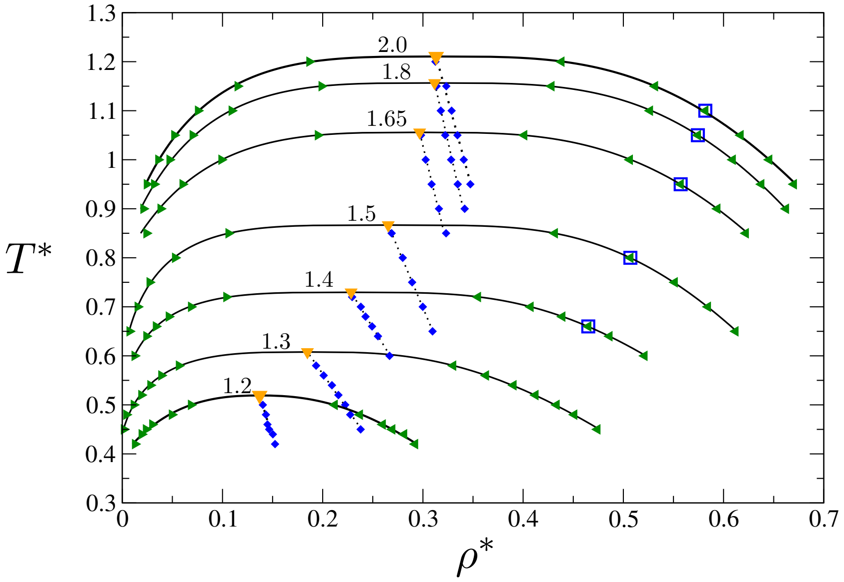

FIGURE 5.7: Variation in the gas-liquid coexistence curves at different values of α (indicated at the top of each fit). The critical points are indicated by the orange triangles, the green rightward and leftward pointing triangles indicate the densities of a coexisting gas and liquid, respectively. The blue squares indicate temperatures and densities at which the $\mathbf{g}(r)$ is computed, chosen such that ϕ^* is approximately equal to mitigate density effects, and displayed in Figure 5.10.

.

(the particular state-points examined are highlighted by the blue squares in Figure 5.7, chosen such that their ϕ^* are approximately equal to mitigate the effects of density on the radial distribution function). Simulations of $< 10^6$ Monte Carlo sweeps (MCS) were sufficient to equilibrate these systems. Production sampling of the site-wise $\mathbf{g}_r$ is then performed over 2×10^6 MCS.

5.5.1 Structural Changes $1.4 \lesssim \alpha < 2.0$

The pair correlation functions in Figure 5.10 characterise the average microscopic structure around each particle. The top panel, the centroid correlation $\mathbf{g}_c$, shows a slight elongation of the mode of all peaks for $\alpha : 2 \to 1.4$, indicating that as σ_h increases, the average $c-c$ inter-particle distance increases. The second panel, the s sphere $\mathbf{g}_{ss}$, shows a gradual progression of the average position of s sub-particles from the inner extent of the interaction range to the outer extent. One can observe for distances between σ_s and $\sigma_s + \lambda\sigma_s$ the presence of at first a sharp peak at σ_s for $\alpha = 2$, which decays until $\sigma_s + \lambda\sigma_s$, where it drops significantly. The converse is true for $\alpha = 1.5$ and 1.4, where the opposite progression occurs. At intermediate α, the presence of h sub-particles perturbs the average bonding environment around the s sub-particles, leading to an additional peak or shoulder observable at $\sigma_s + \sigma_h$ for $\alpha \in \{1.8, 1.65\}$. At the same time one can also observe the increasing correlation of the h components in the third panel and the s

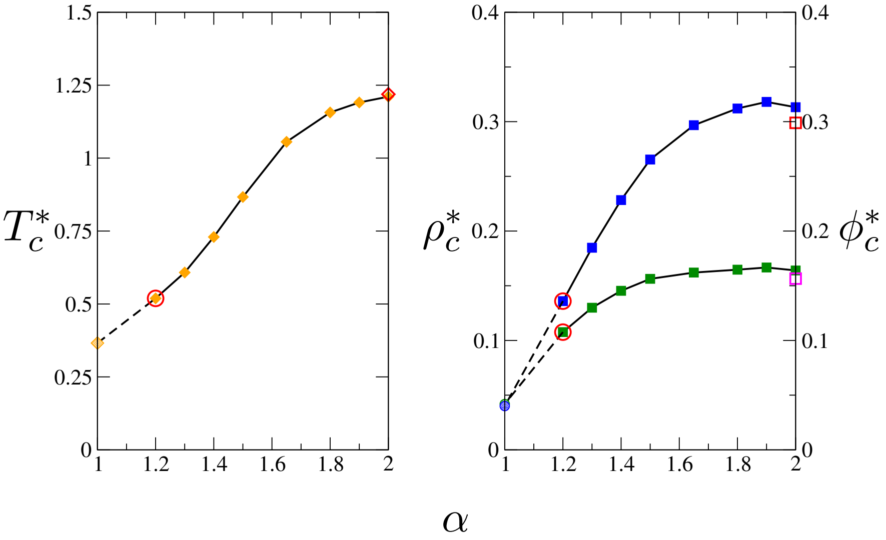

Figure 5.8: T_c^*, ρ_c^*, and ϕ_c^* against α. The differently shaded symbol at $\alpha = 1$ indicates the location of the projected critical point from the study documented in Chapter 4. The dotted line indicates a linear interpolation between the last point at which a liquid is observed by SUS ($\alpha = 1.2$), and the projected critical point. The green symbols indicate ϕ_c^*, with the corresponding magenta square the value calculated from Section 2.3.

and h components in the fourth panel of Figure 5.10 where the correlation of the s and h spheres increases. These data indicate that the h sub-particles begin to play a significant role in the local environment around each bonding site at any α away from 2, and that they begin to *push* against neighbouring s sub-particles, eventually reducing the number of bonds each particle makes. While the mean field interpretation gives us some insight as to why ρ_c^* increases slightly on a small increase of σ_h, eventually the increasing correlation of the h sub-particles begins to significantly perturb the local structure, leading to shifts in the distributions of particle positions in the bonding region. This in turn causes ρ_c^* to shift back toward the large σ_h behaviour. The growth of σ_h on decreasing α eventually restricts the number of bonds per particle and increases the average bond length, such that in order to condense a liquid the system must be cooler.a

5.5.2 Bonding Networks and Interfaces

Where the critcal parameters begin to drop rapidly for $1.5 < \alpha < 1.65$ (Figure 5.8), bonds formed across the h sub-particle diameter are restricted to the outermost extent of the potential range, significantly altering the co-ordination of bonds around each s site. This leads, at sufficiently low temperature, to the formation of h rich pockets in the liquid since maximising the number of bonding interactions creates a drive to segregate the h components. As σ_h grows beyond λ, the presence of h rich pockets grows, until the formation of layered structures occurs. Layered structures form where the presence of

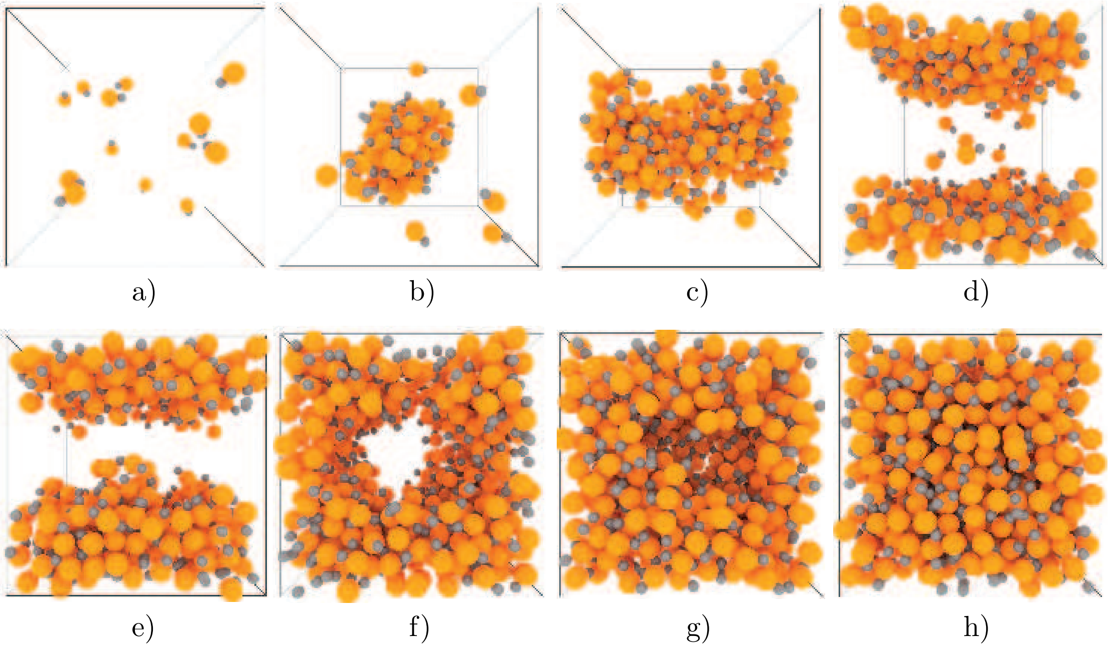

FIGURE 5.9: Snapshots of selected configurations obtained via AVBMC and SUS where $\alpha = 1.5$, $T^* = 0.65$. Here the SW-s sub-particles are coloured orange, and the HS-h sub-particles are coloured grey. They include: a) monomer gas $\rho^* \approx 0.01$; b) droplet coexisting with gas at $\rho^* \approx 0.07$; c) percolated cylinder coexisting with gas at $\rho^* \approx 0.13$; d) slab coexisting with gas $\rho^* \approx 0.23$; e) slab at $\rho^* \approx 0.31$; f) cylindrical bubble at $\rho^* \approx 0.41$; bubble cavity at $\rho^* \approx 0.5$; homogeneous liquid at $\rho^* \approx 0.61$.

the h sub-particle occupies enough of the bonding region to force a significant proportion of the h sub-particles into the interface.

This behaviour causes two problems for simulation. Firstly, at high liquid densities the propensity of the particles to align such that their s sub-particles face inward from an interface and their h sub-particles face outward toward the interface by any layered structure implies that the number of insertion sites with $-\Delta U$ at low temperature, where the interface has adopted a concave structure — such as with the aforementioned h rich regions (consider panel e) of Figure 5.12) — is depleted, rendering the acceptance of insertion moves low. Secondly, any nucleated structure will be affected by the finite size of the simulation box as particles tend to form interfaces with their hard h sub-particle facing the void. Formation of elongated structures cause percolation to occur at low density, quite close to the gas peak. Figure 5.11 demonstrates the effect of finite size on the gas branch of the $P(\rho^*)$ curves for $\alpha \in 1.3, 1.2$. One may consider that these structures are thermodynamic minima in the density space, although careful inspection of the state-points must be performed to ascertain their properties. It has been demonstrated that for simulations performed to compute the coexistence densities via MC techniques in the GC ensemble that the finite size of the simulation cell stabilises structures that

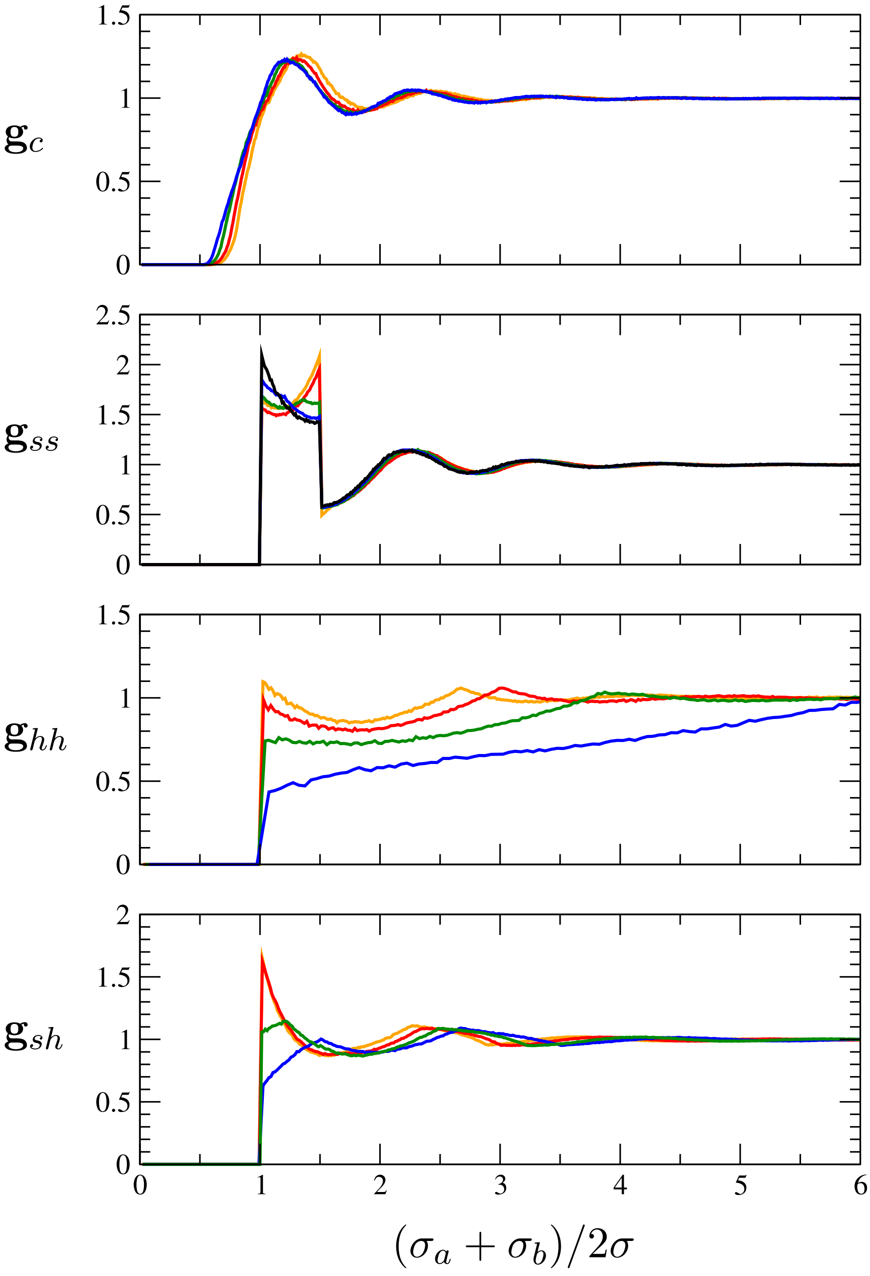

FIGURE 5.10: Distributions of site-wise $\mathbf{g}(\mathbf{r})_{ab}$, where $a, b \in s, h$, of liquids at coexistence densities formed at sub-critical temperatures over the range $1.4 < \alpha < 2.0$. Colours indicate the value of α: black, blue, green, red, and orange correspond to 2 (a pure SW system, only depicted in $\mathbf{g}_{ss}$), 1.8, 1.65, 1.5, and 1.4 respectively. These distributions demonstrate the effect of the presence of the h sub-particle on the microscopic structure of the liquid. Further discussion of features can be found in the text.

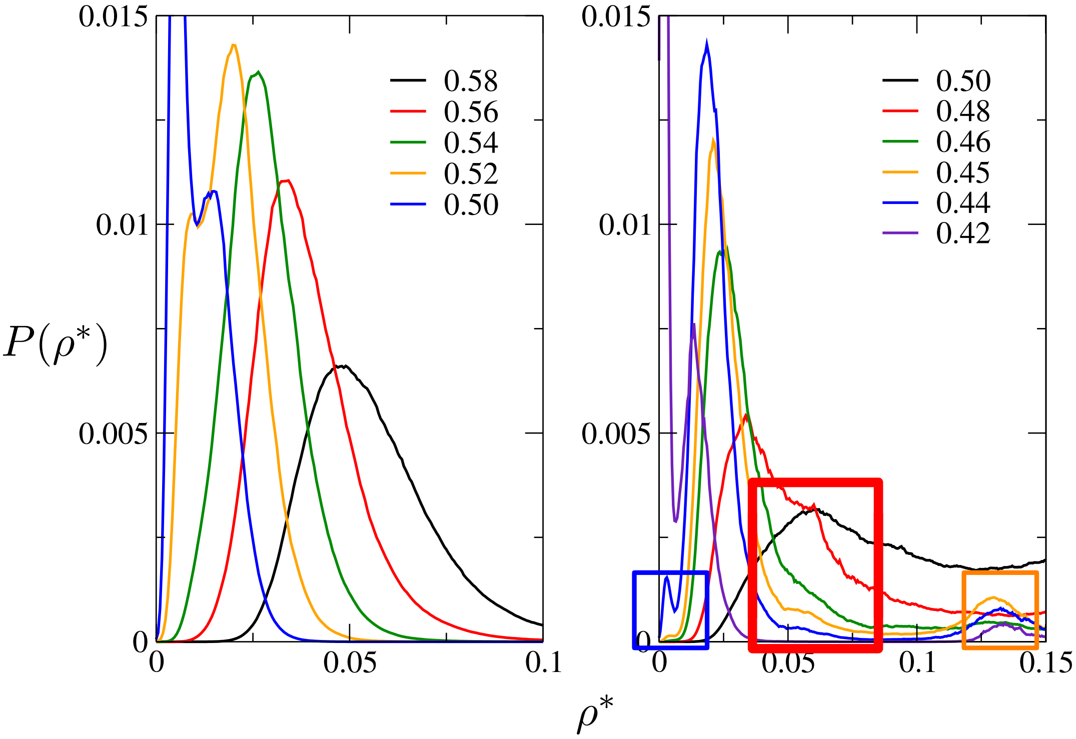

FIGURE 5.11: Finite size effects on the coexisting gas branches of the $P(\rho^*)$ against ρ^* for $\alpha = 1.3$ (left) and $\alpha = 1.2$ (right). Additional peaks and shoulders manifest over certain density ranges due to the finite size of the simulation box and the peculiarities of the potential description. Coloured boxes indicate the locations in the ρ^* space of finite size. The orange box captures a region where a single bilayer has percolated across the cell diameter; the red box indicates a region where a cylinder percolates across the cell; the blue box indicates the monomer gas peak which is metastable with respect the the small nucleate peak where $\rho^* \approx 0.025$ at $T^* = 0.44$, but dominates at $T^* = 0.42$.

minimise their interfacial free energy [87]. I.e. on the scale of a finite simulation, intermediate phases which possess minimal surface area are perfectly thermodynamically stable, but may not be representative of the bulk behaviour in the thermodynamic limit (as $N \to \infty$ and $\phi^*_{interface} << \phi^*_{bulk}$). The remedy is to increase the size of the simulation sufficient to remove the influence on the binodal of the locally stable structures with respect to the coexisting gas or liquid.

In the case of $\alpha = 1.3$, a simple system size increase suffices to remove the influence of the low density structures. For these systems, using a maximum window of $\omega = 2000$ and the corresponding box length such that $\rho^*_{max} = 0.6$ is met by the final window (an effective N-scale doubling). For $\alpha = 1.2$, the case is not so simple. Doubling the system size yields additional finite size effects and causes problems for the sampling of the histogram bin edges.

The presence of highly structured percolated structures obtained by SUS at very low density (Figure 5.12) implies that the characteristic length-scale is larger than the box dimensions, i.e. $\sigma_\epsilon > V^{1/3}$. To explore whether σ_ϵ is divergent or simply larger

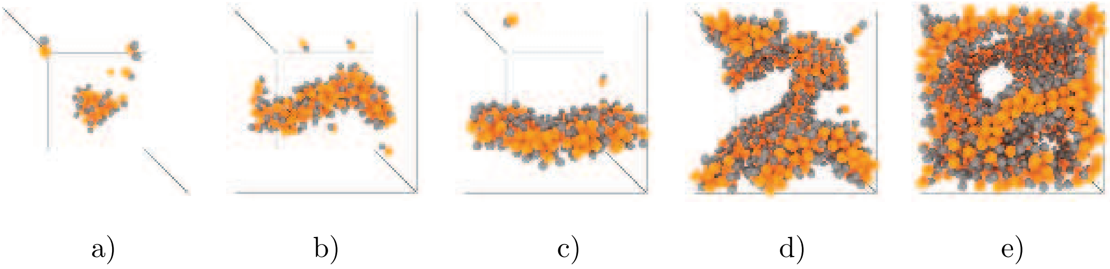

FIGURE 5.12: Structures observed in SUS runs where $\alpha = 1.2$ with $\omega_{max} = 2000$ across ρ^* at $T^* = 0.42$. From left: micelles at $\rho^* \approx 0.01$ (a); percolated string at $\rho^* \approx 0.05$ (b); percolated bilayer at $\rho^* \approx 0.13$ (c); curved bilayer slab with bridging arm at $\rho^* \approx 0.25$ (d); and a continuous cavity (percolated void) in the bilayer network liquid at $\rho^* \approx 0.3$ (e).

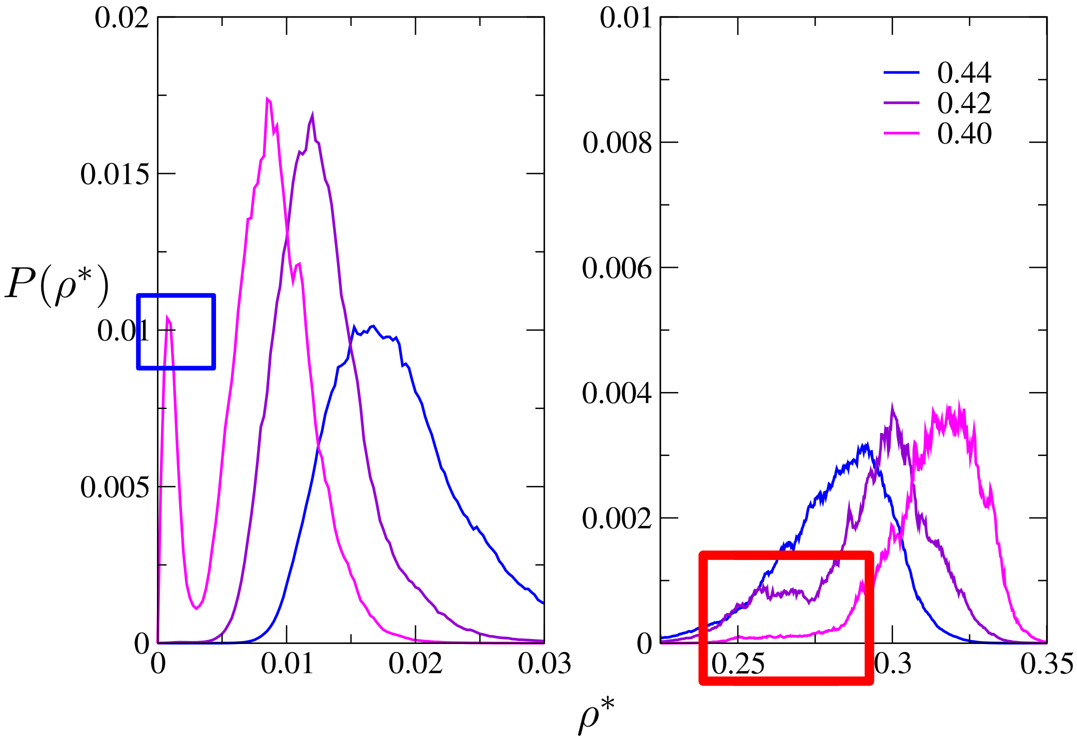

FIGURE 5.13: Persistence of finite size effects in simulations with larger system sizes in the binodal region for $\alpha = 1.2$. Colour convention maintained from the rightmost panel of Figure 5.11, with the exception of the additional distribution where $T^* = 0.40$.

than the current L_{box}, systems of $N = 3000$ particles were simulated at constant volume employing the AVBMC algorithm at $T^* \in 0.42, 0.44, 0.46$ over the density range $0.01, 0.02, 0.03, 0.04, 0.05, 0.06, 0.07, 0.08$. Snapshots of the self assembled structures can be seen in Figure 5.14.

Most puzzling for $1.15 < \alpha < 1.3$, at $0.01 \leqslant \rho^* <= 0.03$, is the presence of a single aggregate structure, a vesicle coexisting with a monomer gas. Upon increasing the density this vesicle structure percolates in 1D across the periodic boundary forming a tube (where $0.03 \leqslant \rho^* < 0.06$)), whose diameter increases with further increasing density to eventually percolate in a second dimension to form a wave-bilayer structure (where

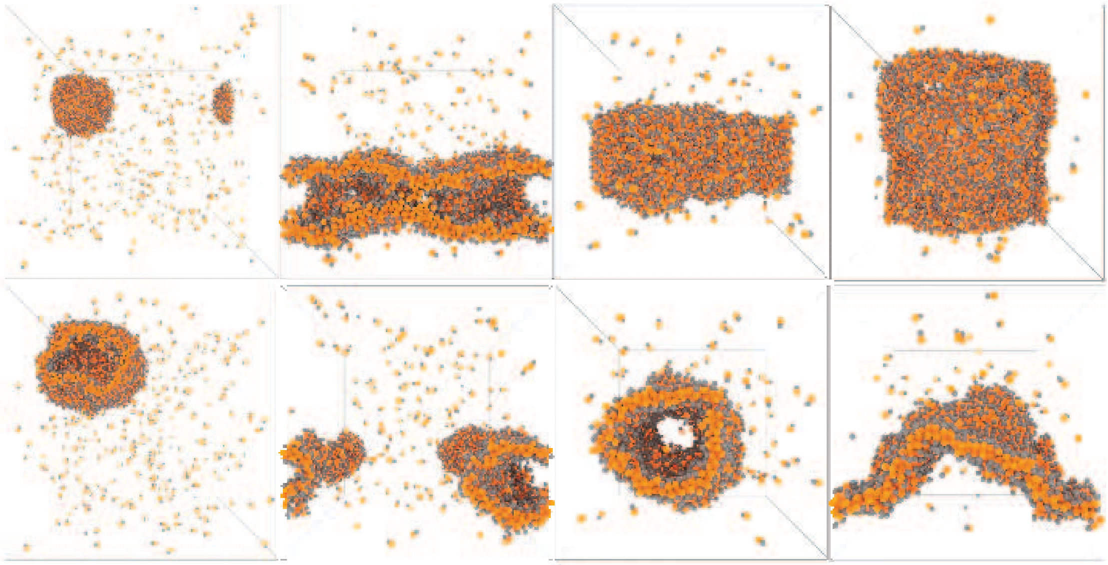

a) b) c) d)

Figure 5.14: Structures obtained utilising the AVBMC algorithm at constant volume. The top and bottom each correspond to the same snapshot: a) hollow vesicle coexisting with a monomer gas at $\rho^* = 0.01$; b) a percolated tube coexisting with a monomer gas at $\rho^* = 0.03$; c) tube with a larger diameter at $\rho^* = 0.06$; a continuous wavy lamellar sheet at $\rho^* = 0.07$.

$\rho^* \geqslant 0.07$). The structure at $\rho^* = 0.08$ (see panel (d) of Figure 5.14). If one were to perform a constant pressure simulation across this isotherm, it may be the case that the vesicle and tube structures would disappear (since there is no barrier to surface merging imposed by the presence of the smaller h particle, this is in contrast to vesicle structures observed elsewhere where the hard-core sub-particle forms what is essentially a non-interacting shell around the vesicle [29, 55]) and one would obtain solely bi-continuous layered structures. This possibility was not explored here, but is left for future work (see Chapter 8). The observation of bilayer vesicles and a continuous tube with hollow internal cavities and curved sheet structures (since the smaller h sub-particle allows the layer to tolerate some curvature, see Chapter 6) at such low densities is an important finding that may be of technological interest. While properly implemented PBC should return the behaviour of the bulk, the cubic cell geometry still exerts an influence on the characteristic length of any assembled structure, it is therefore the case that systems obtained in this region of the α space — i.e. where continuous structured systems occur at low ρ^* (such as percolated bilayers and tubes) where the simulation cell is cubic and static — actually return the behaviour of the system under a percolation enforced confinement. Constant pressure simulations with variable box dimensions may be employed to explore this possibility.

Chapter 6

Self-assembly

During the exploration of the variation of gas-liquid phenomena in Chapter 5, at sufficiently low temperature, complex ordering of particles leads to the development of particle assemblies that perturb the gas-liquid coexistence curves as calculated by SUS where $\alpha < 1.3$. Given that these structures influence the modelling of the liquid and gas phases in our finite systems, their properties ought to be studied in order to test whether their existence in a simulation is merely an artefact of finite size, or if their free-energy is lower than the competing liquid or gas in the thermodynamic limit. Since no definitive answer can be reached by means of the simulation set, this chapter proceeds by developing arguments both for and against the thermodynamic stability of certain structures obtained by the simulated annealing approach outlined below.

6.1 Self-Assembled Structures

The inherent anisotropy in both the shape of the particle and the potential virtually guarantees some orientational order to arise in structures obtained via a simulation. Moreover, due to the presence of the h sub-particle, which has no attractive interaction, the formation of interfaces is commonplace. The presence of the hard portion forces the system to adopt an interface dominated structure. This point is crucial. Any structure that forms will try to minimise its interfacial energy. Since the presence of the h sub-particle at sufficiently large σ_h restricts the number of bonding interactions a particle can engage in, any structure which seeks to minimise its surface energy will arrange its constituent particles such that they orient with respect to its neighbours to form s rich regions and h rich regions. Where $\alpha < 1.3$, i.e. where the total volume of the particle has a significant contribution from the h sub-particle. One way to interpret this partitioning is to think of the particles as a model surfactant, where the s sub-particle is the solvophobe. The analysis in Chapter 5 demonstrated that as the h sphere grows for $\alpha < 2.0$, the gas-liquid critical parameters (eventually) reduce in magnitude to bring the gas-liquid coexistence curve into close contact with self assembled layered structures. In spite of being plagued by finite size effects for the smaller system sizes studied, the formation of highly ordered structures at sufficiently low temperature indicates that there is a strong tendency to organise an interface and that the interface usually considered to contribute strong finite size effects on simulations of isotropic potentials is likely to be standard for Janus type nano-particles. Where structures begin to have a divergent characteristic length $\sigma_c \to L_{box}$, the finite size, and constant aspect ratio of the simulations cell allows only structures that have a wavelength with maximum dimension L (or $L^{1/2}$ or $L^{1/3}$ if appropriately oriented). This can be most intuitively seen in panel (d) of Figure 5.14. This implies that the aspect ratio of the cell will exert a strong influence on the structure which forms. We assume this will have the effect of stabilising phases with approximately cubic symmetry across α.

6.2 Notes on Packing

The simple parameterisation developed here allows the broad prediction of structural properties of linear aggregates as a function of purely geometric considerations. Figure 6.1 demonstrates the construction of the dumbbells to obtain the restrictions on packing on surfaces of arbitrary curvature. This is, of course, only in 1D and a more thorough analysis must take into account 2D and 3D packing arguments, however as a starting point some interesting properties of the dumbbells can be obtained via this method. Projecting rays from the homothetic centre through the internuclear axis and the common tangent produces an angle, θ, which is employed to study packing restrictions. The angle θ is defined by

$$\theta = \sin^{-1}\left(\frac{\sigma_\Lambda - \sigma_\Delta}{\sigma_\Lambda + \sigma_\Delta}\right), \tag{6.1}$$

where σ_Λ is the diameter of the *larger* sphere: normalised to unity and which can include the interaction range (if $\alpha > 2/3$, see Figure 6.2) when considering a geometry away from the close-packing limit; and σ_Δ is the smaller sphere which is the parameter we varied. Although this angle can be generalised to spherical geometries by converting to a solid angle, we consider only 1D packing here, however. Figure 6.1 and Figure 6.2 demonstrate that the space is split into two regions above and below the close packing limit corresponding to regions above and below $\alpha = 1$, indicated in the legends, where constraints differ. Below $\alpha = 1$ the interaction range $(\lambda\sigma_s)$ extends beyond the limit of the h sub particle, where $\sigma_s = \sigma_{\Delta} = 2/3$ and above. Below this point $\sigma_s + \lambda\sigma_s < \sigma_h$. Outside the region delineated on one side by the close packing line and the outer extent of the orange region is inaccessible to the system. Above $\alpha = 1$, $\sigma_s + \lambda\sigma_s = \sigma_{\Lambda}$ and $\sigma_h = \sigma_{\Delta}$. The boundary of the blue-green region and the white-space defines a maximum. The number of particles, N_r, one can pack, under the given constraints, straddling the perimeter of r_c, where the radius is defined from the centre of the largest sphere to the homothetic centre, H.

$$N_r = \left\lfloor \frac{\pi}{\theta} \right\rfloor, \tag{6.2}$$

where $\lfloor\rfloor$ indicates the nearest lower integer. Where $\alpha > 1$ a curved surface that orients all h sub-particles toward the centre of a spherical cavity is subject to a minimum N_r defined by the blue-green line and the white-space. structures in the fluid can have an $N_r > N_r^{min}$ defined by this boundary. r_c as indicated on Figure 6.1, the distance from the homothetic centre, H, to the centre of the larger sphere, is given by

$$r_c = \frac{1}{\kappa} = \frac{\sigma_\Lambda}{2\sin\theta}, \tag{6.3}$$

where κ is the curvature.

Referring to Figure 6.2, observing lower limit of the orange shaded curve where $\theta = 0$ and $\sigma_S = 2/3$ ($\alpha = 2/3$), r_c diverges indicating the point at which a straight linear connection of particles is first possible. At or marginally above this limit, if bilayer structures were to form, each h sub-particle must contact its neighbours while the inner bonding region is at the furthest extent of the potential range. Close packed structures (black line on Figure 6.2) still have a finite N_r and so curved structures are expected to dominate this region. Above this limit but below $\alpha = 1$, providing there is sufficient free volume within the potential range, particle configurations can have any curvature (see the bottom panel of Figure 6.3). Where $\alpha > 1$ one can infer that for an $\alpha = 1.25$, a structure that contains h-rich pockets must have a minimum pocket diameter of 3σ and at least 6 particles in the loop.

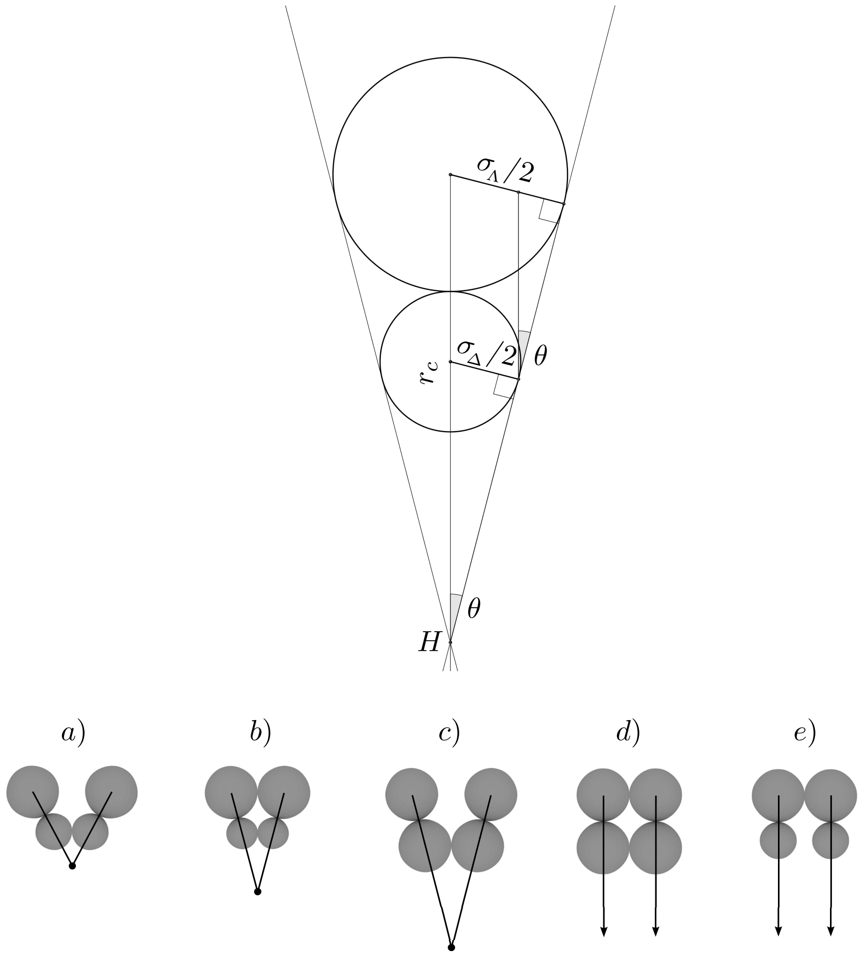

FIGURE 6.1: Computing the packing properties for the asymmetric dumbbell. Geometric analysis of the dumbbell yields limits on the geometry of aggregates and continuous structures. Lengths σ_Λ and σ_Δ correspond to the diameters of large and small spheres. Cases *a*) and *c*) correspond to scenarios where $\alpha \geqslant 1.0$, *b*) and *d*) correspond to close-packed scenarios for $\alpha = 1.0$ (d), and any $\alpha \neq 1.0$ (b). The unique case *e*) corresponds to the limit $\alpha = 2/3$, where values of $\alpha > 2/3$ have the ability to form structures with zero curvature in at least 1D.

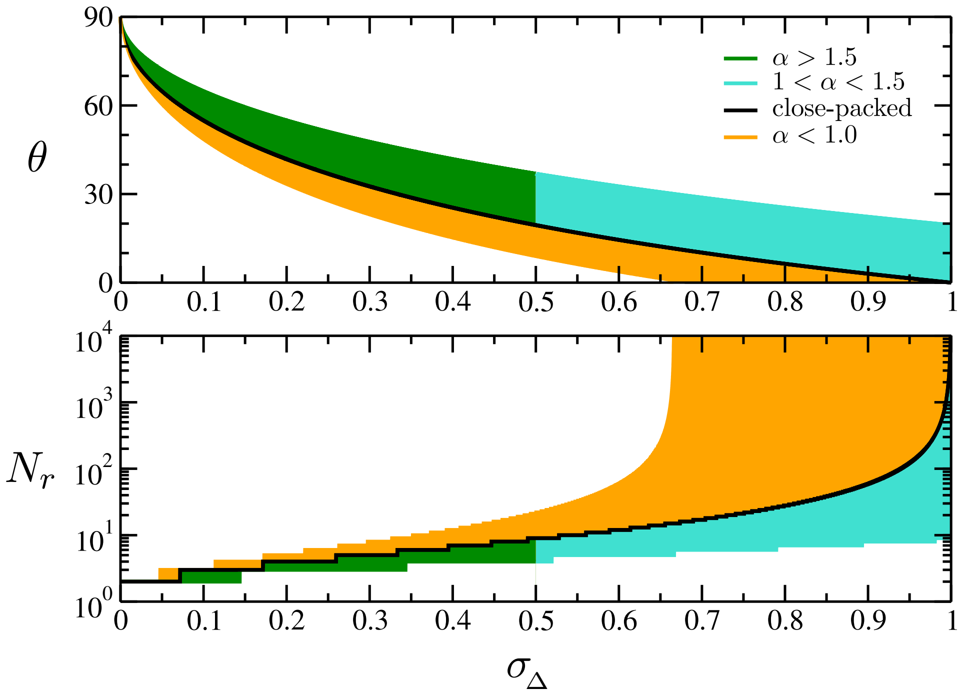

FIGURE 6.2: Angle θ made by geometric analysis of the dumbbell shape, and the number of particles N_R, able to pack around a circle with r_c (Figure 6.3) defined by θ.

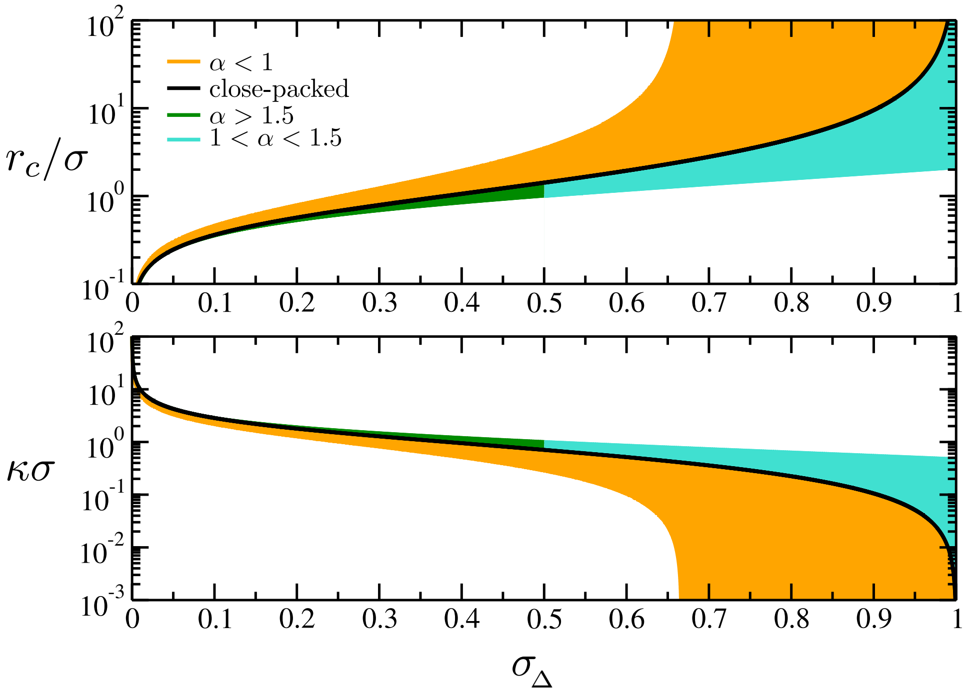

FIGURE 6.3

This analysis is unsuitable for flat structures where $\alpha < 1$. Dumbbells constrained to pack in a flat geometries such as bilayers have restrictions on the number of contiguous dumbbells that can pack in a row. The limits for which can be found via a different diagram (see Figure 6.4). For packing in flat structures, the number of particles that can pack in a straight line is limited by the presence of the h sub-particle. There are two limiting cases: the case where all the small spheres on one side of a layer are touching - the close packing limit (cp) ; and where the small spheres are at the furthest extent of the potential range, such that $\vec{r}_{ss} = \sigma + \lambda\sigma$, we shall refer to this as the bonding limit (bl). In general, the close-packing limit allows for smallest number of particles to fit for a given α, and the bonding limit allows for the largest number. We define the centres of each of n s sub-particles to be co-linear, each joined to an h sub-particle, with internuclear distance $(\sigma_s+\sigma_h)/2$. The distance between any two touching h sub-particles is σ_h, and we calculate the number (to n_{cp} for the close packing limit, and to n_{bl} for the bonding limit) of particles able to be packed before one of two limits occur. Figure 6.4 demonstrates the parameters for computation of n_{cp} and n_{bl}. We define a distance, c_i, describing the internuclear distance between h_i and s_{i+1} defined by angles θ_i, ψ_i, ϕ_i, which are in turn defined recursively by a system of equations:

$$c_i = L^2 + H^2 - 2LH\cos(\theta_i), \tag{6.4}$$

$$\psi_{i+1} = \cos^{-1}\left(\frac{H^2 + L^2 - c_i^2}{2HL}\right) \tag{6.5}$$

$$\phi_{i+1} = \cos^{-1}\left(\frac{H^2 + c_i^2 - \sigma_h^2}{2Hc_i}\right), \tag{6.6}$$

$$\theta_i = \pi - \psi_i - \phi_i, \tag{6.7}$$

Where H is the internuclear distance between s_i and h_i, defined here to be $(\sigma_s + \sigma_h)/2$, and L the inter-nuclear distance between s_i and s_{i+1}. This system of equations is propagated until one of two limits is reached. Either the h_i comes into contact with s_{i+1} where $c_i = (\sigma_s + \sigma_h)/2$; or, $\theta_{i+1} < 0$ in which case the next particle forced to align to the surface can not be bound to the previous particle. If there are an even number of particles in the layer, θ_0 takes the value

$$\theta_0 = \frac{\pi}{2} - \sin^{-1}\left(\frac{\sigma_h - L}{2H}\right) \tag{6.8}$$

Figure 6.4 demonstrates both the parameterisation for the packing calculation, and the result for the close-packing limit and the bond limit cases for even and odd numbers of particles. In a similar fashion to the analysis for $\alpha < 1$, (see the orange region in the bottom panel of Figure 6.3), for both the even and odd cases, n_{bl} case diverges as $\alpha = \sigma_s \to 2/3$. The close-packing limit at this point for the odd case $n_{cp}^{odd} = 5$, meaning that from this point where $\lambda = 0.5$, a structure that splits characteristic bonding lengths to the ends of the interaction range can contain layers of close packed dumbbells and also pack infinitely with the benefit of the outer bonding length contributing a unit of β. It is possible that having a smaller interaction range this behaviour may not be seen until the particles are more similar in size.

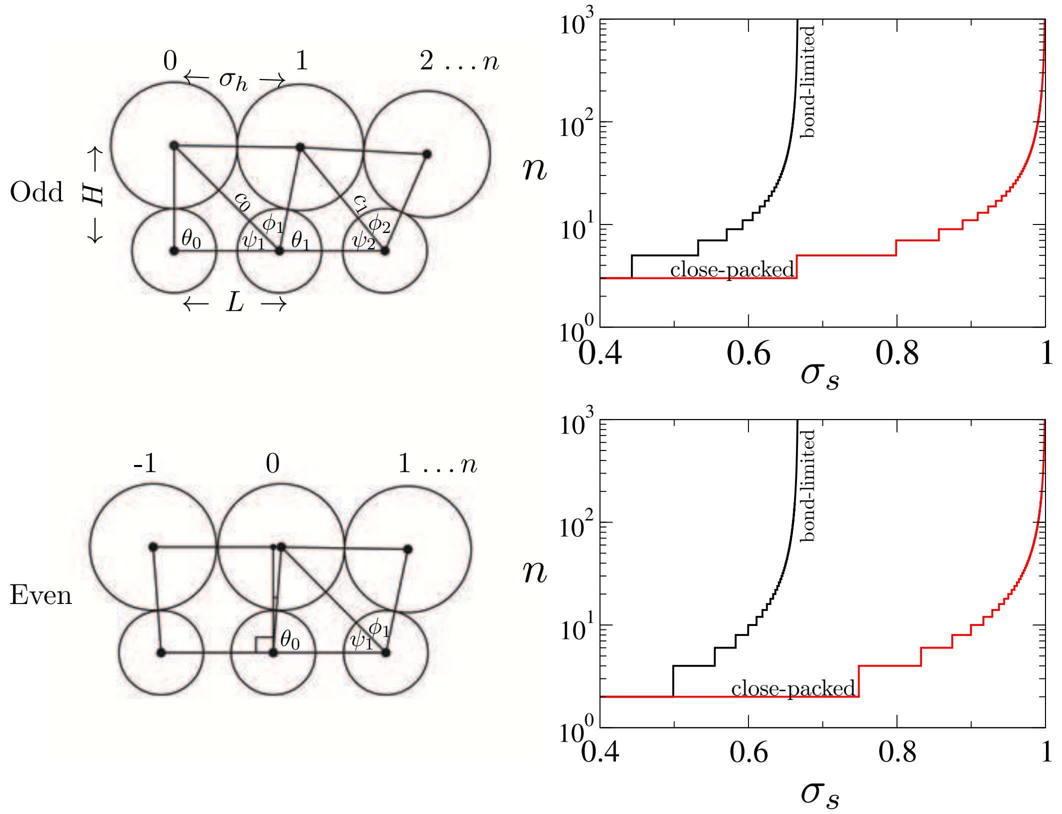

FIGURE 6.4

6.2.1 Simulated Annealing

The SA heuristic was applied to particle systems of $N = 1000$ over the α range between $0.25 \leqslant \alpha \leqslant 1.3$. Simulations begin at a temperature near $T_{\mathcal{B}}$, slightly less for $\alpha > 1$ but well above T_c^* for the corresponding α, and are allowed to equilibrate before the annealing process begins. Where $\alpha < 1$ the initial temperature was taken as approximately $T_{\mathcal{B}}$. The precise starting temperature factor β_i is determined by the decrement interval β_s the length of the annealing process L_{SA} in MCS, and the target temperature factor β_f,

$$\beta_i = -\left[\beta_s \times L_{SA} + \beta_f\right]. \tag{6.9}$$

Figure 6.5 collects the state-points studied and the location of lines delineating pertinent trends. The curve describing $T_{\mathcal{B}}$ has also been scaled (see curve labelled $T_{\mathcal{B}}$ - scaled (green)) to meet the critical temperature of the pure SW system. The variation of the scaled $T_{\mathcal{B}}$ approximately tracks the variation in critical parameters across the range of α. Where it extends into the region where $\alpha < 1$ possibly indicates a region of $T^*(\alpha)$ beneath which either condensation or some form of assembly process occurs. This is addressed later in this chapter.

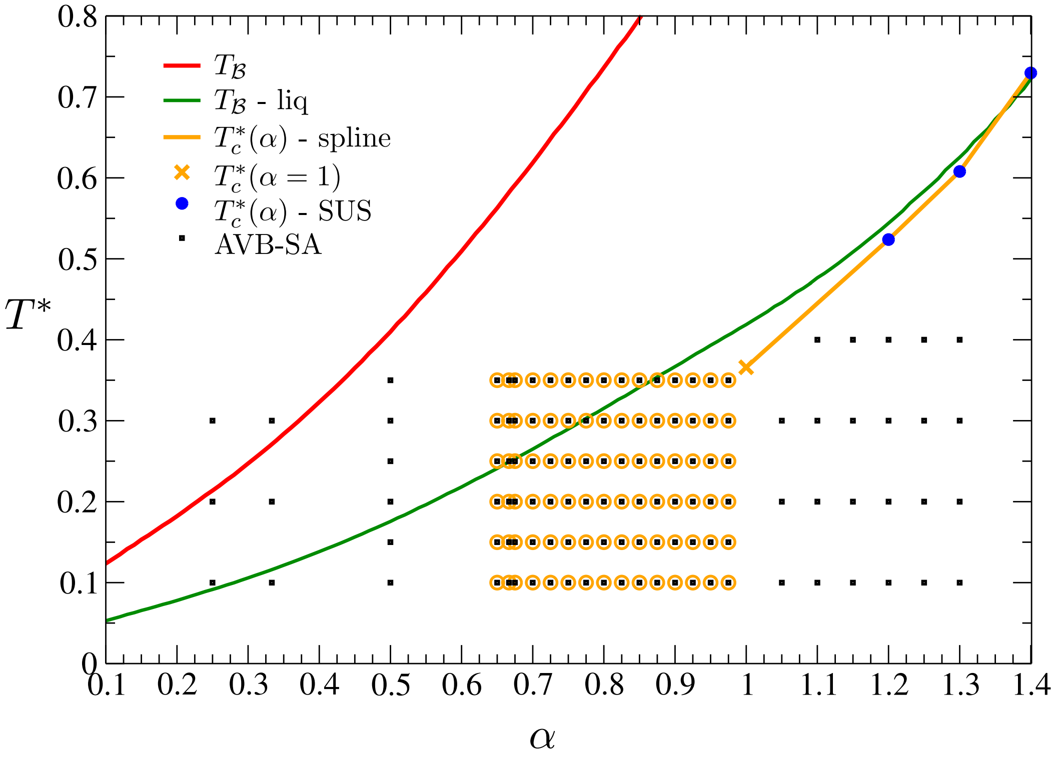

FIGURE 6.5: Summary of all T^* examined at each α by SA employing the AVBMC algorithm (black squares) and the regions also probed by AVBMC without the SA heuristic. Also located here for reference, various temperatures considered when determining the temperature descent protocol: $T_{\mathcal{B}}$, $T_{\mathcal{B}}$ - scaled to meet $T_c^*(\alpha = 2)$, $T_c^*(\alpha)$ as obtained by SUS technique.

6.3 Structural Diversity $\alpha < 1$

6.3.1 Fractal Dimension of Clusters $\alpha < 1$

In order to discuss the geometry of aggregates in a systematic fashion the α space below $\alpha = 1$ is divided into two regions above and below $\alpha = 2/3$. Below $\alpha \approx 2/3$, no continuous structures are observed. Below $\alpha \approx 0.25$ simple geometric arguments can be employed to understand the structure of aggregates where the temperature is sufficiently low to encourage aggregation. From slightly below $\alpha \approx 0.25$, the aggregates have some choice as to what structure they adopt with many low lying in energy structures competing, a zoo of face-capped polytopes can be formed, all with approximately spherical geometry. The region where $\alpha \gtrsim 2/3$ the system is observed to first form continuous aggregates. The presence of the h sub-particle here influences the aggregate geometry by inhibiting linear growth of clusters in a counter-intuitive manner (see Figure 6.4).

The $\log - \log$ plot of N_s against R_g/σ yields the fractal dimension of the cluster systems, D_f, as the approximate slope of the distribution. Figure 6.6 shows the radius of gyration,

R_g, against cluster size, N_s, over a sampling[1] of all clusters observed where $\alpha < 1$. R_g is in terms of σ. Three main regions of differing geometry can be abstracted from Figure 6.6. Where N_s is smaller than 20, across all α, aggregates $D_f \approx 3$ form. Where $N_s \gtrsim 20$, aggregated structures begin to take on density driven growth determined by the packing constraints, and can be classified roughly into 1, 2, and 3 dimensional regions. Regions which appear to have non-integer or fractured dimensionality, tend to be as a result some curvature imposed by orienting around neighbouring structures, or by some percolation enforced confinement where σ_c, the characteristic length approaches $V^{1/3}$. At very high N_s and state points where the percolation locus is at relatively low density, $L_{box} \propto \rho^*$ begins to effect a limit on R_g as measured, outside the range on the diagram. Clusters with an $R_g > L_{box}/2$ are not included on the diagram.

The adoption of different geometries which depend upon both the state point, as well as the geometric restrictions placed upon the bonding network of s sub-particles by the presence of h sub-particles (see Section 6.2), is inspected by first considering D_f for each state-point (T^*, ρ^*) at each α. Since T^* must be sufficient to encourage an aggregation process, and in order to traverse the large length-scale variation in a sensible manner, parameter α, which determines σ_s and thus $\sigma_s\lambda$, the interaction range, implies that the corresponding T^* that encourages an aggregation process will also vary with α.

As is evident from the plot, phases at different α undergo distinct regions where the collection of system aggregates take on differing fractal dimension (D_f, read as the approximate slope of the curves with the same colour, where the colour indicates α) over the range of densities studied. For low N_s across the range of α, the cluster system geometry can be described as approximately spherical (arguably zero dimensional, though these regions have a $D_f \approx 3$). For the lowest α studied, the dimension of aggregate growth remains ≈ 3 across most ρ^* and T^* up to the highest N_s where a cluster merging process takes place. As α is increased, the maximum N_s of approximately spherical aggregates grows. For $\alpha > 2/3$, where, due to steric hindrance imposed by the presence of the h sub-particle on growing aggregates, clusters cannot grow in all 3 dimensions and so begin to take on structures with different geometries. Where $\alpha \approx 2/3$ and above, at sufficiently low temperature, the bonding network of s sub-particles can maximise the number of bonds by arranging into flat platelet structures. These platelets are approximately circular across the large diameter. The platelets attain a slightly lower $<U/N>$ along the interior regions by packing into close packed layers with a finite maximum along the close-packed region(n_{cp}), stacked together with an offset of $\approx \sigma_s/2$. such that they approximately form an intra-layer triangular lattice. Referring to Figure 6.4,

---

[1] Due to the large quantities of data generated, only a subset of points chosen randomly, appear on Figure 6.6.

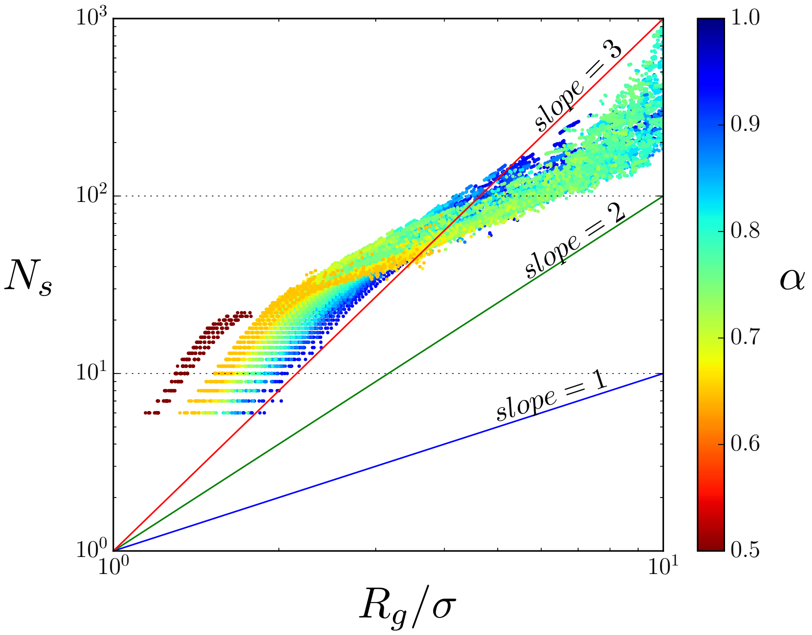

FIGURE 6.6: The size of a cluster, N_s, against the radius of gyration in terms of the characteristic length σ: R_g/σ, over the range of densities and temperatures studied, for each α, indicated by the colourbar. The slope gives system fractal dimension D_f. The red, green, and blue lines guide the eye for slope for $D_f = 3$, 2, and 1, respectively.

platelets which form before $\alpha = 2/3$ are subject to hard constraints in their average diameter. Where $\alpha \to 1$, the system is observed to adopt 2D bilayer structures consistent with the endpoint studied in Chapter 4. In the intervening region $2/3 \lesssim \alpha \lesssim 0.925$, where these flat proto-lamellar platelet structures form, two interesting phenomena are observed. Firstly, from $\alpha = 0.725$, strip-like structures are observed. These strips have a similar internal structure to the observed platelets, yet sacrifice some breadth in order to maximise their length (and thus U). Secondly, above $\alpha \approx 0.775$ strip structures branch which can form bridges between strips. Where branching occurs, the system geometry is not restricted to linear or planar structures and can form networks of branched strips that percolate through the system in 3D. This is observable as the aqua-marine—sky blue portions of Figure 6.6 possess regions where, for $N_s \lesssim 10^2$ the systems have $D_f \approx 1$ (parallel with the blue line) and for $N_s \gtrsim 10^2$, $D_f \in (1, 3)$.

6.3.2 Aggregates and Variations

In the region of $\alpha < 1$ we observe three finite structure types, one with 2 sub-types, and 4 distinguishable continuous phases. Of the finite structures, these differ by internal bond structure and interface geometry. Where the density is sufficiently high, and where α allows, certain types of structures are observed to yield continuous phases.

$\alpha << 2/3$

Micelles

Micelle structures form at all $\alpha < 1$ but take different forms at different α. Polytopes and roughly spherical aggregates form at low α. Figure 6.7 displays the energy per particle at each T^*, ρ^* for $\alpha = 1/4$ and $1/3$. At $T^* = 0.3$ for $\alpha = 1/4$, $< U/N >$ indicates behaviour of a compressible gas, where $T^* = 0.2$, some form of assembly has occurred with a gradient in ρ^* and by $T = 0.1$, the system energy is essentially flat. The case is similar for $\alpha = 1/3$, however by $T^* = 0.2$ the distributions are essentially flat. Where the the gradient of $< U/N >$ with respect to ρ^* is zero indicates a region over which compressing the particles makes no difference to the bonding behaviour. It is possible that further compression of the system will lead to a different $< U/N >$ where the clusters must pack together. Figure 6.8 displays the distribution of cluster sizes for $\alpha = 1/4$ (panel a) and $\alpha = 1/3$. Figure 6.9 and Figure 6.10 display typical snapshots of clusters up to N_s^{max}. Over this region the structure of aggregates take simple polytope geometries. The largest allowed clusters are rare. They usually form where a cluster can face-cap an already relatively close-packed structure and are entropically disfavoured with respect to those with smaller N_s that allow some free-volume around each particle in the cluster. The modes in Figure 6.8, at temperatures to see significant clustering (i.e. $T^* \lesssim 0.2$), which are $N_s^{mode} = 6$ for $\alpha = 0.25$ and $N_s^{mode} = 10$ for $\alpha = 0.25$. Notice $< U/N >$ for $\alpha = 1/4$ roughly coincides with $N_s - 1$ for N_s^{mode} (since a $U/N \approx N_{bonds}/2$), indicating that these structures maximise the number of bonds per particle for this state point (i.e. each particle makes a bond to each of the others in the host cluster). This relationship is not observed above $\alpha = 1/4$, where factors in addition to the maximally bonded structure (see Section 6.3.1) where packing the h sub-particle around the bonding core begins to play a stronger role in determining the structure of the aggregate.

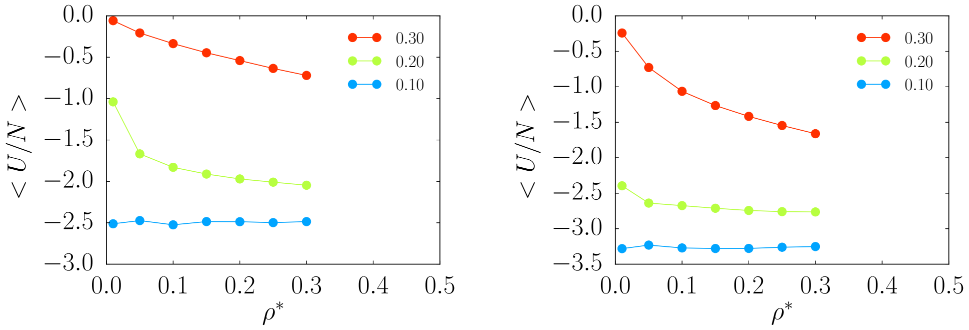

(a) $\alpha = 1/4$, $N_s^{mode} = 6$. (b) $\alpha = 1/3$, $N_s^{mode} = 10$.

FIGURE 6.7: Average energy per particle, $< U/N >$, as a function of density along isotherms indicated in the legend of each panel.

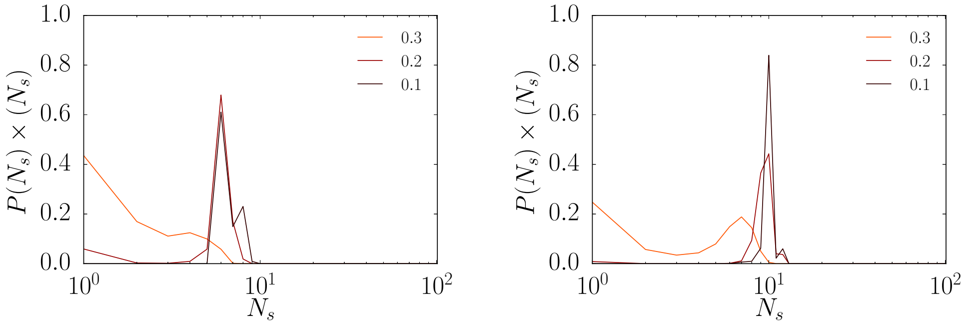

(a) $P(N_s) \times N_s$ for $\alpha = 1/4$, $\rho = 0.2$. (b) $P(N_s) \times N_s$ for $\alpha = 1/3$, $\rho = 0.2$.

FIGURE 6.8: The probability of observing a particle in a cluster of size N_s.

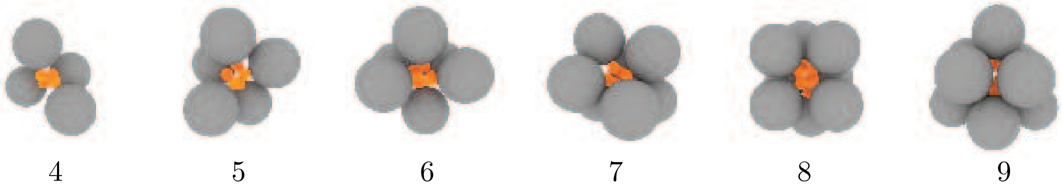

FIGURE 6.9: Micellar aggregates where $\alpha = 1/4$. The number indicates N_s. The cluster with $N_s = 8$ (second to last), has a square anti-prism bonding arrangement of s sub-particles reflected in the packing of the h sub-particles. The rightmost cluster ($N_s = 9$) is a face-capped (compare the vacant site viewed where $N_s = 8$) square prism.

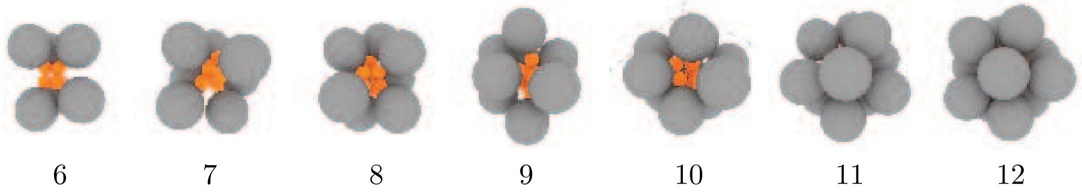

FIGURE 6.10: Micellar aggregates where $\alpha = 1/3$. The number indicates N_s. The leftmost cluster is a trigonal prism. As $N_s \to 12$ defect icosahedral order increases. The final cluster where $N_s = 12$ is an axially compressed icosahedron.

Where $\alpha = 1/2$ micelles are observed to be larger and more spherical. Figure 6.11 depicts the $P(N_s) * N_s$ and $< U/N >$ along isotherms. There is a smooth progression from $T^* = 0.35$ down to $T^* = 0.15$ where the $< U/N >$ then jumps down to where the number of bonds per particle is approximately eight. The jaggedness of the $P(N_s) * N_s$ indicates that there is not a lot of cluster rearrangement, that the clusters observed here are likely frozen. Crystallinity of clusters was not explored further here, though additional peaks resolve in the radial distribution function (similar to those in Figure 6.16), further analysis needs to be performed to ascertain their structure(s) and investigate their high ρ^* properties, however. Snapshots of large clusters at $\alpha = 1/2$ are depicted in Figure 6.12.

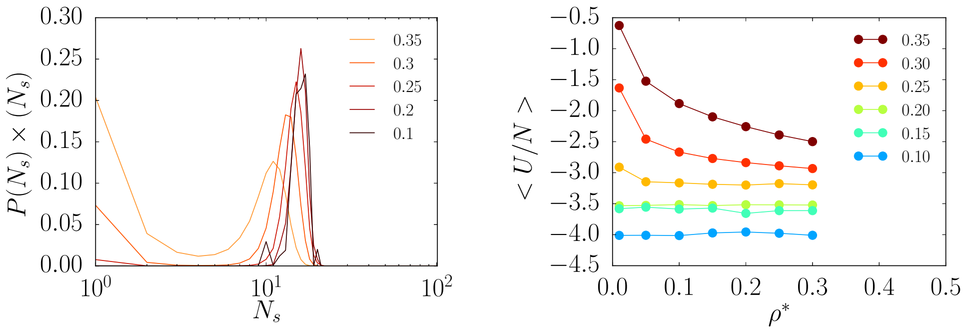

(a) $P(N_s) \times N_s$ for $\alpha = 1/2$, $\rho = 0.2$.

(b) $<U/N>$ for $\alpha = 1/2$, $\rho = 0.2$.

FIGURE 6.11: The probability of observing a particle in a cluster of size N_s and $<U/N>$ for $\alpha = 1/2$.

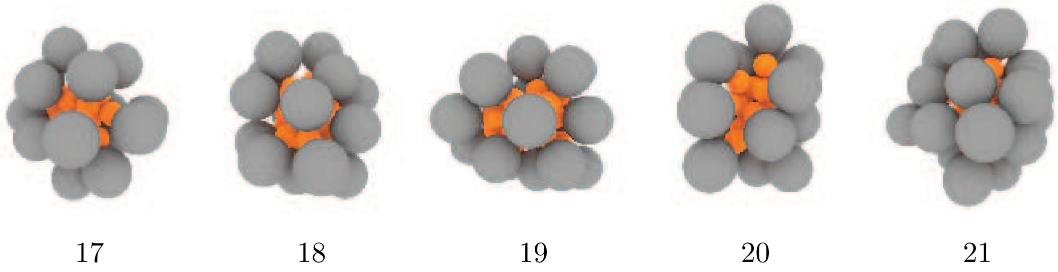

FIGURE 6.12: Micellar aggregates where $\alpha = 0.5$. The number underneath indicates N_s. By this α, micelles have ceased to be rationable as simple polytopes where they now take on approximately spherical or slightly elongated geometries.

Elongated Micelles

On the interval $0.5 \lesssim \alpha < 0.65$, micelles gain the ability elongate. Still restricted in longest dimension by the presence of the h sub-particle, these elongated clusters vary in shape and bond networks and tend to be observed at the lowest temperatures and highest densities studied. Figure 6.13 shows the $<U/N>$ (panel a) and the $<N_s>$ (panel b) for $\alpha = 0.65$. Where $T^* > 0.25$, again a compressible gas is observed. For $0.3 < T^* < 0.15$ a smooth progression in energy and roughly invariant average cluster sizes occur across ρ^* over each isotherm. Eventually, where $T^* < 0.20$, a negative slope of $<U/N>$ with $\rho^* > 0.15$ is observed. For the last two densities on panel b) the average cluster size almost doubles. This behaviour correlates with a density driven cluster merging process. Here smaller micelles merge to form elongated micelles. Snapshots of elongated micelles from across $0.15 < \rho^* \leqslant 0.3$ where $\alpha = 0.65$ and $T^* = 0.15$ can be seen in Figure 6.14.

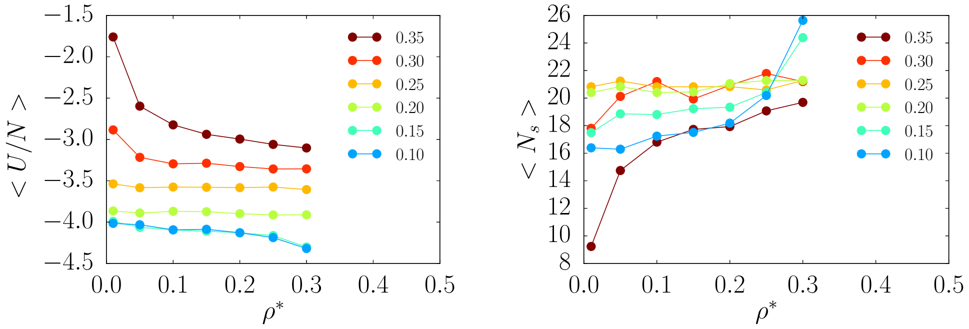

(a) $<U/N>$for $\alpha = 0.65$.

(b) $P(N_s) \times N_s$ for $\alpha = 0.65$, $\rho = 0.2$.

FIGURE 6.13: Energy profiles $<U/N>$ and average cluster size across each isotherm indicated in the legend.

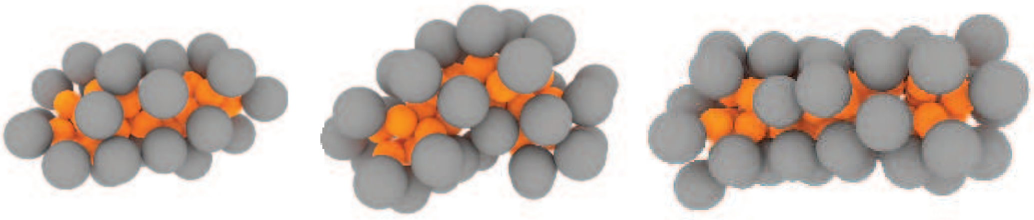

$\rho^* = 0.20$ $\rho^* = 0.25$ $\rho^* = 0.30$

FIGURE 6.14: Elongated micellar aggregates at $\alpha = 0.65$.

Platelets

By $\alpha = 2/3$, clusters are observed to flatten out into a platelet structure. Platelet structures occur at low temperatures and are finite in extent, constrained by packing h sub-particles around the exterior bonding core along a flat geometry (see Section 6.4). These platelets have an average diameter determined by α and the stacking geometry they adopt. Figure 6.15 depicts snapshots of clusters over each α.

Ordering into Platelets

The differentiation of state-points consisting of mostly micelles or platelets (since they are often observed to coexist) can be performed by inspecting the radial distribution function. While the formation of additional peaks in $\mathbf{g}(r)$ can also signify the location of onset of other structures, such as crystalline non-platelet clusters, these distributions differ qualitatively. Figure 6.16 demonstrates the formation of additional peaks in the radial distribution functions at $\alpha = 2/3$ between a micelle dominated state-point (red); a region with approximately half micelles, half platelets (green); and platelet dominated

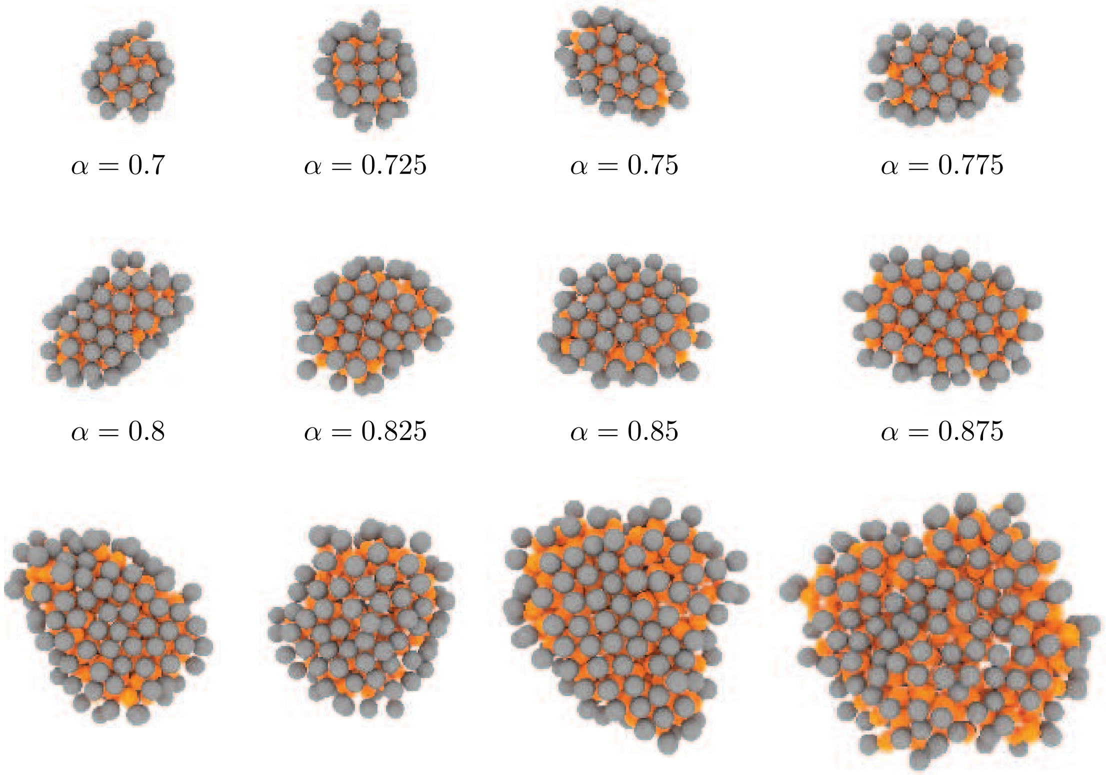

$\alpha = 0.7$ $\alpha = 0.725$ $\alpha = 0.75$ $\alpha = 0.775$

$\alpha = 0.8$ $\alpha = 0.825$ $\alpha = 0.85$ $\alpha = 0.875$

$\alpha = 0.9$ $\alpha = 0.925$ $\alpha = 0.95$ $\alpha = 0.975$

FIGURE 6.15: Platelet structures formed at low ρ^* at each α at $T^* = 0.2$, demonstrating the increase in platelet diameter with increasing α. Also notice that for $\alpha > 0.9$ the internal structure of these aggregates ceases to have the partitioning of close-packed — bond-limited structure.

state-point (blue). Peaks resolve in $\mathbf{g}_{ss}$ at state-points where significant platelet formation has occurred. Correlations in the $s-s$ distributions imply resolution of bond distances. This bifurcation of the bonded peak implies that particles involved in platelet structures pack with two characteristic bonding lengths, roughly at the inner and outer extent of the interaction range. Packing into structures where planarity is enforced forces a platelet system to adopt a structure with two properties. Where limits occur in $\mathbf{g}_{sh}$ that is where $\vec{r}_{sh} \approx (\sigma_s + \sigma_h)/2$, where h sub-particles rest upon a neighbouring s, orientation of the h sub-particle are influenced by the orientation of its immediate neighbours. Platelets are observed to be composed of close-packed layers of approximately triangular layer stacking. The layer on the opposing side does not sit in the trigonal interstices of other layer, but pack such that each close packed stripe on the opposing side line up, with an in-plane offset of $\sigma_s/2$. Ordering into platelets, specifically where the close packing behaviours are concerned, is consistent with the packing arguments outlined in Section 6.2.

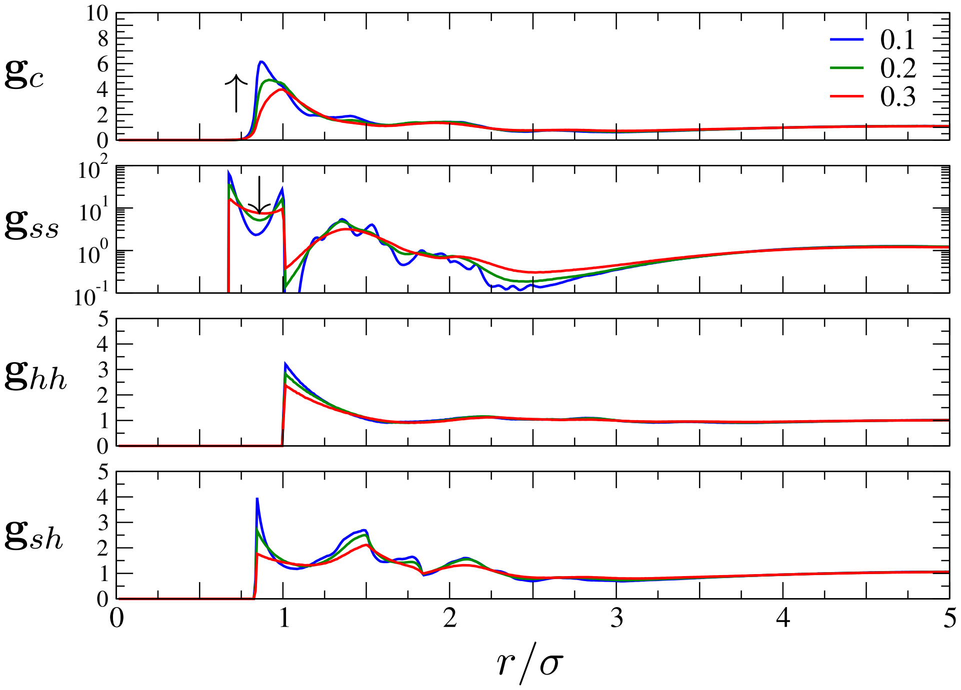

FIGURE 6.16: Where $\alpha = 2/3$ at $\rho^* = 0.25$, radial distribution functions $\mathbf{g}_c$, $\mathbf{g}_{ss}$, $\mathbf{g}_{hh}$, and $\mathbf{g}_{sh}$, over selected T^* indicated in the top panel. The peaks resolving on lowering T^* indicate an ordering process between elongated micelles at high $T^*(\gtrsim 0.2)$ and crystalline platelet clusters at low $T^*(\lesssim 0.2)$.

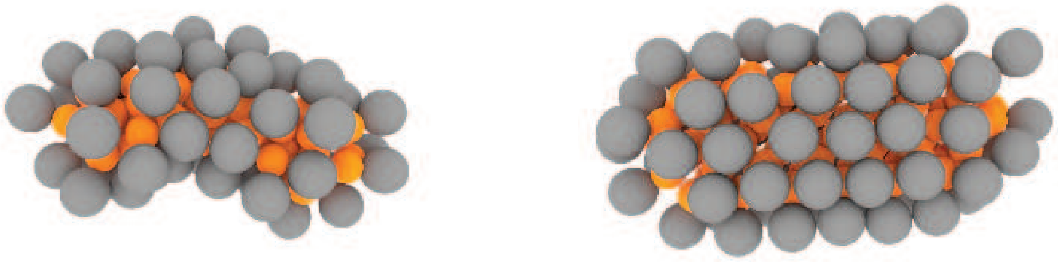

FIGURE 6.17: An elongated micelle and a platelet at $\alpha = 0.725$ with approximately equal N_s from $\rho^* = 0.2$, between T=

Strips

Strips form at the high end of densities studied where $\alpha < 0.8$. Where $\alpha > 0.8$, the formation of strips occurs at increasingly low ρ^*. The internal structure of the strips is similar to the platelet structures at the corresponding α, suggesting that formation of strips may occur by platelet merging processes. If strips are to form from structural relaxation of large micelles, they may take on a different bond structure. Strips have a lower $<U/N>$ and can pack more efficiently than platelets. Due to their similar internal structure, we define a delineation between a platelet and a strip as the aspect ratio. We define the platelet-strip aspect ratio to be determined by the 'length' (defined as the longest linear dimension), c, of a planar cluster divided by the 'width' (the shortest linear dimension), a. If a platelet-like cluster has an aspect ratio $c/a \gtrsim 2$ then it is referred to as a strip. At state-points where platelets and strips coexist, platelets have a slightly larger smallest diameter. It is likely that if the assembly process into strip structures from a platelet occurs by merging and orientation-relaxation, the growing strip will sacrifice some of its diameter, and thus $< U/N >$ in order pack into a continuous structure. A temperature moderated assembly process may also take place, where a disordered elongated micelle structure relaxes into a more defined strip structure. An example of this for $\alpha = 0.725$ can be viewed in Figure 6.18. Hierarchical assembly relaxation has been observed in similar model colloids between multi-loop structures to planar layers [31]. This process itself may have a significant activation barrier for shorter range potentials. It is likely that a large relative interaction range encourages relaxation events such that they can be observed in simulations in reasonably tractable simulation lengths.

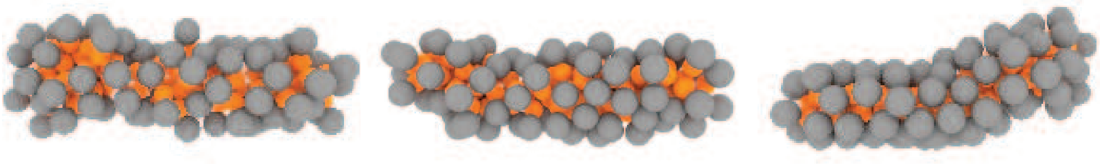

Figure 6.18: Structural resolution of an longated micelle on cooling at $\alpha = 0.725$.

$2/3 < \alpha \leqslant 3/4$

Where $\alpha = 3/4$ an interesting scenario arises. The s sub-particle is sufficiently large to form 1D continuous layered aggregates (i.e. $\alpha > 2/3$ - see Figure 6.2) — strips — and yet the strips are not quite yet able to form branched structures. Between $T^* = 0.25$ and $T^* = 0.20$ a transition from a fluid of elongated micelles which percolate at high ρ^* to ordered plate and strip structures is observed. Figure 6.19 displays $< U/N >$, and $< N_s >$ for $T^* \geqslant 0.2$. Above $T^* = 0.2$, the system is composed of micelles coexisting with a monomer gas yielding a relatively small per particle energy. As ρ^* is increased, the monomer population is decreased until only elongated micelles are observed, which at the highest densities percolate through the system, indicated by a larger $< N_s >$. Across the isotherm $T^* = 0.2$, the system undergoes three distinct regions each with two regions where different structures are observed to coexist. For $\rho^* < 0.15$, platelets and micelles are observed together. Where the density is higher, at $0.15 \leqslant \rho^* < 0.25$, platelets and strips coexist. Above $\rho^* \approx 0.2$ a pure strip phase is observed. The formation of platelets

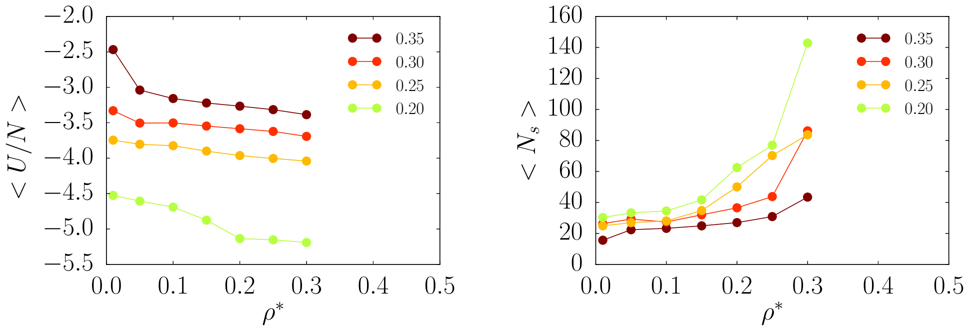

(a) $<U/N>$for $\alpha = 0.75$.

(b) $P(N_s) \times N_s$ for $\alpha = 0.75$, $\rho = 0.2$.

Figure 6.19: Energy profiles $<U/N>$ and average cluster size across each isotherm indicated in the legend.

at low T^* is accompanied by a lower $<U/N>$. Upon increasing the density, the system forms additional platelets until $\rho^* = 0.15$ where strips are first observed, accompanied by a further reduction in $<U/N>$, where $<U/N>$ eventually remains constant.

Figure 6.21 shows radial distribution functions obtained on simulations of a percolating fluid and the strip structures at $\rho^* = 0.25$. The development of peaks in all $\mathbf{g}_{ss}$ indicates a long range ordering of bonding particles in the strip that is not present in the nearby higher T^* fluid (see Figure 6.21). The distributions of $P(n_i \cdot n_j)$ at $T^* = 0.2$ and $0.01 \leqslant \rho^* \leqslant 0.30$ (displayed in Figure 6.20) demonstrate a small degree of orientational ordering developing at high density. Where $\cos\theta_{ij} \approx 0.9$, a small lip is visible. This effect is caused by the close-packed intra-layer regions where the position of the next particle in the layer has a restricted orientation. Due to the fact that $P(n_i \cdot n_j)$ is a global order metric, the magnitude of this effect is suppressed since strips at these low densities are not restricted to align to one another. Though on increasing ρ^* a small amount of global orientation order develops.

The strips that form are mostly linear (a small amount of strip curvature in the long axis is observed to be tolerated – see also the rightmost panel of Figure 6.23) and where the density is sufficient the strips are observed to percolate across the simulation cell. Snapshots of configurations at different ρ^* across an isotherm ($T^* = 0.2$) are depicted in Figure 6.22.

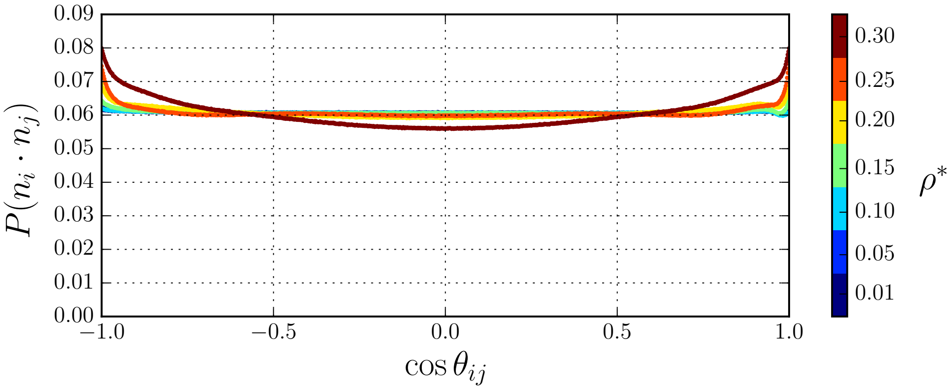

FIGURE 6.20: Global orientation distribution $P(n_i \cdot n_j)$ collected over each ρ^* where $\alpha = 3/4$. A small degree of orientational order arises at high density.

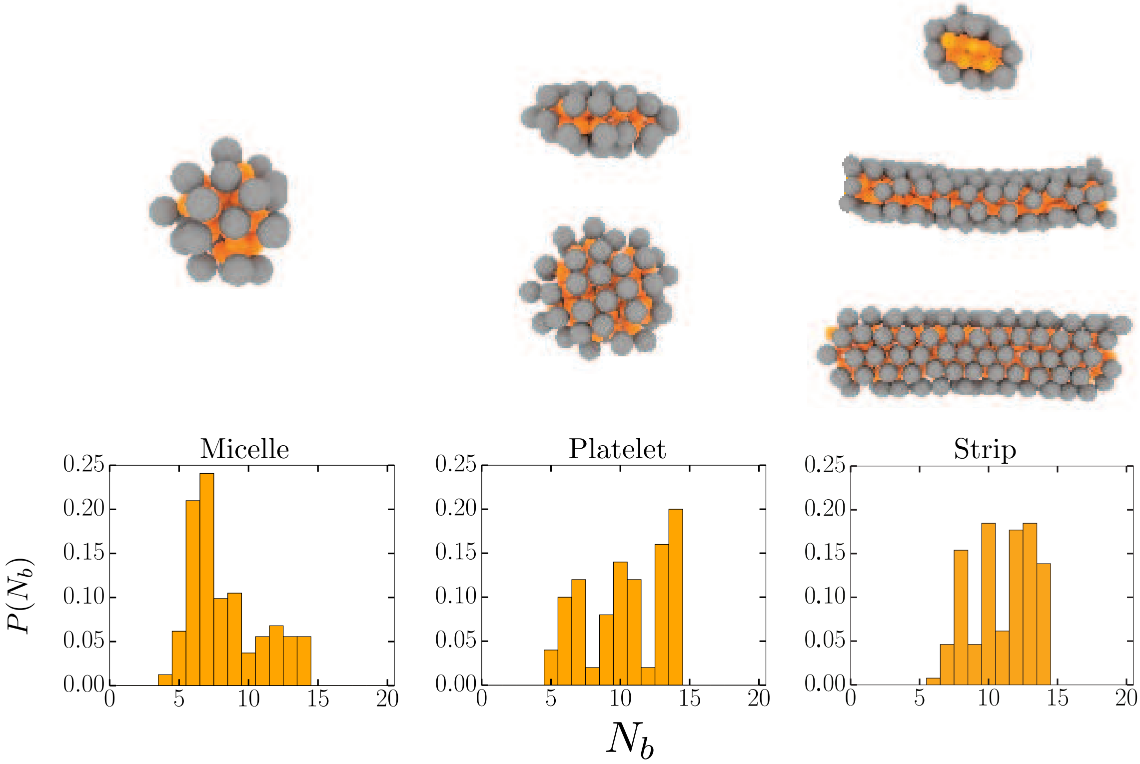

FIGURE 6.23: Examples of aggregates formed where $\alpha = 3/4$. Bond profiles for each type of structure are pictured underneath.

Strip structures are composed of close packed planes of particles stacked with a $\sigma_s/2$ offset between successive stacking with the long axis at an angle $\approx \sin^{-1}(1+\lambda)/2$ to the close packing direction. Figure 6.24 shows the values of order parameters $\mathcal{M}$, $\mathcal{V}$, and $\mathcal{B}$ (top panel), and $\mathcal{M}$ against $\mathcal{B}$ for each density where $\alpha = 0.75$ at $T^* = 0.2$.

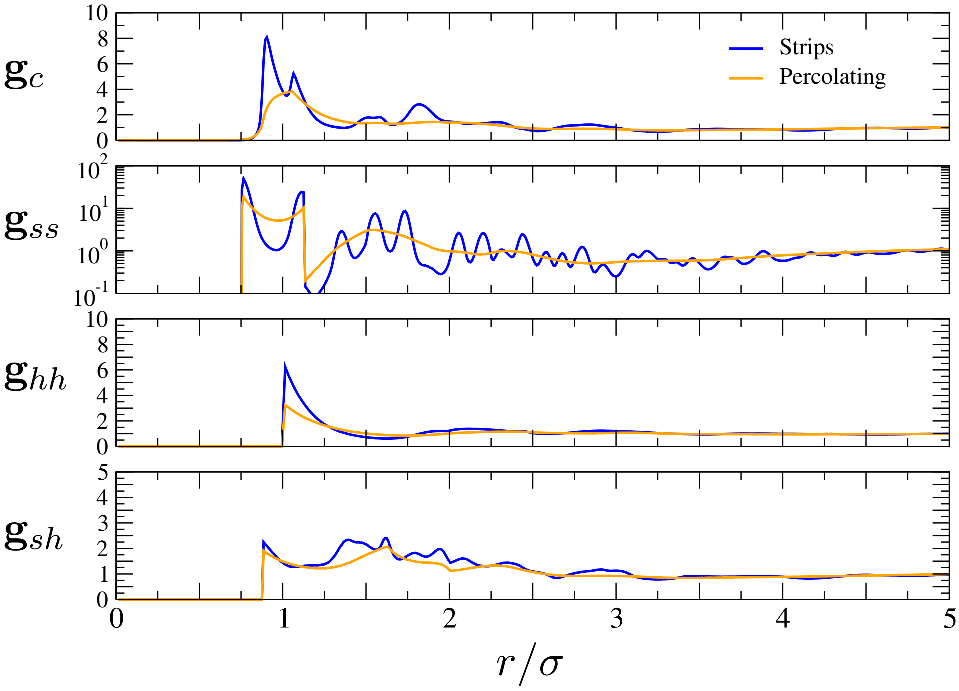

FIGURE 6.21: Where $\alpha = 0.75$ at $\rho^* = 0.25$, radial distribution functions $\mathbf{g}_c$, $\mathbf{g}_{ss}$, $\mathbf{g}_{hh}$, and $\mathbf{g}_{sh}$, for a percolating fluid at $T^* = 0.25$ and below the strip transition at $T^* = 0.2$ indicated in the top panel. The peaks resolving on lowering T^* indicate a long range ordering process. Strip structures at this ρ^* percolate across the simulation box (see the final panel of Figure 6.22)

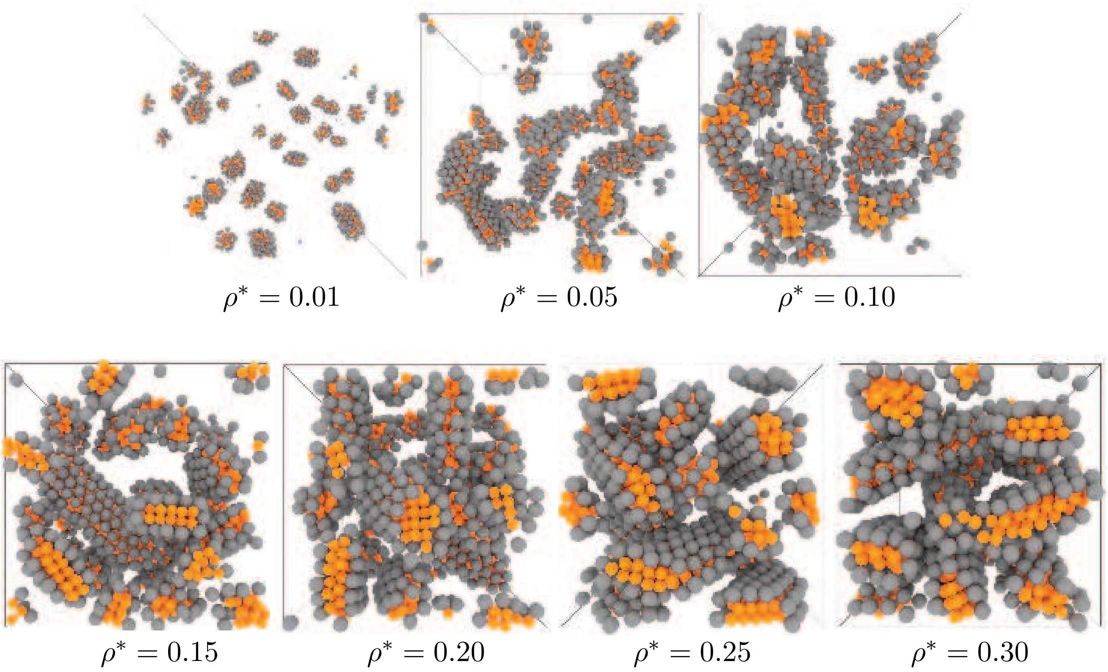
$\rho^* = 0.01$ $\rho^* = 0.05$ $\rho^* = 0.10$

$\rho^* = 0.15$ $\rho^* = 0.20$ $\rho^* = 0.25$ $\rho^* = 0.30$

FIGURE 6.22: Snapshots of final configurations from simulations where $\alpha = 3/4$, $T^* = 0.2$. Platelets and micelles structures are observed from $0.01 \geqslant \rho^* \geqslant 0.10$, mixtures of platelets and strips are observed between $0.10 < \rho^* \leqslant 0.2$ and pure strips for $\rho^* > 0.2$.

Strip structures that are located in the bilayer region have a maximum $\mathcal{B} \approx 0.5$. This relatively low $\mathcal{B}$ value indicates that while there is significant bilayer structure in each strip, that the steric interaction of adjacent h spheres, consistent with the packing arguments outlined in Section 6.2, forces each successive dumbbell to have an angle offset from normal to the stacking plane, forcing the structure to have a reduced bilayer character as measured by $\mathcal{B}$.

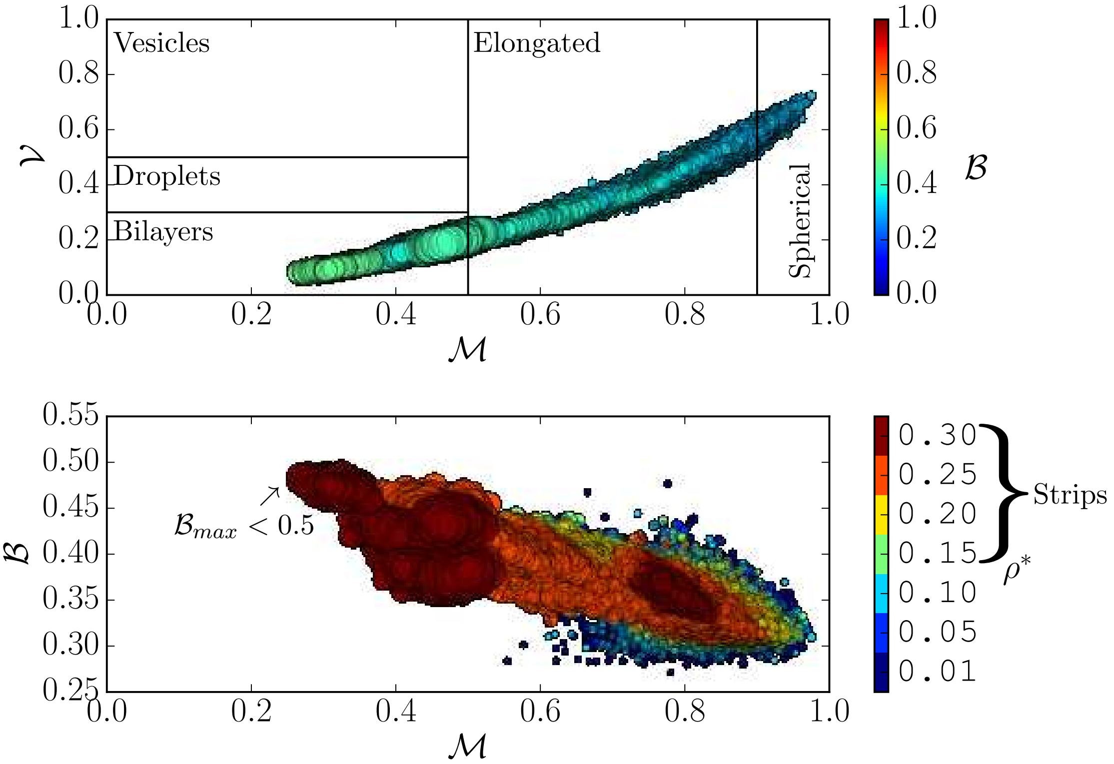

FIGURE 6.24: Plots of metrics $\mathcal{M}$ against $\mathcal{V}$ coloured by $\mathcal{B}$ (top panel) and $\mathcal{M}$ against $\mathcal{B}$ where the colour indicates ρ^* and the size indicates the size of the cluster, N_s. Superimposed on the top panel are the delineations between regions of differing cluster behaviour as labelled. All aggregates observed during production sampling across the $T^* = 0.2$ isotherm are considered here.

6.3.3 Branched structures and sponge-like order

Above $\alpha = 0.775$, the strips appear to tolerate significant curvature along the long axis and, if percolated, and therefore under self-imposed confinement, tend to twist. Panel (a) of Figure 6.25 shows some twisted strip structures that form at low densities where $\alpha = 0.8$. At low T^*, and sufficiently high ρ^* the system adopts networks of branching strips. Panel (b) of Figure 6.25 demonstrates an example of a branched structure. Further along the α parameter, branched network structures at moderate ρ^* give way to sponge-like structures at high ρ^*. These sponge-like structures appear to have a larger degree of branching, have broader layered regions (i.e. possess more lamellar character) than the corresponding network structures. We define a sponge structure to be small regions of curved bilayer sheets bridged by arm structures with percolated voids. Figure 6.28 depicts a sponge structure obtained at $\alpha = 0.9$. As α is increase further toward unity, lamellar structures begin to dominate the phase behaviour. This can be observed by inspecting the increasingly quartic appearance of distributions of $P(n_i \cdot n_j)$ as a function of ρ^* across an isotherm as depicted in Figure 6.30. Snapshots of a lamellar phase at $\rho^* = 0.30$ and sponge phase at $\rho^* = 0.25$, where $\alpha = 0.95$ can be viewed in Figure 6.29.

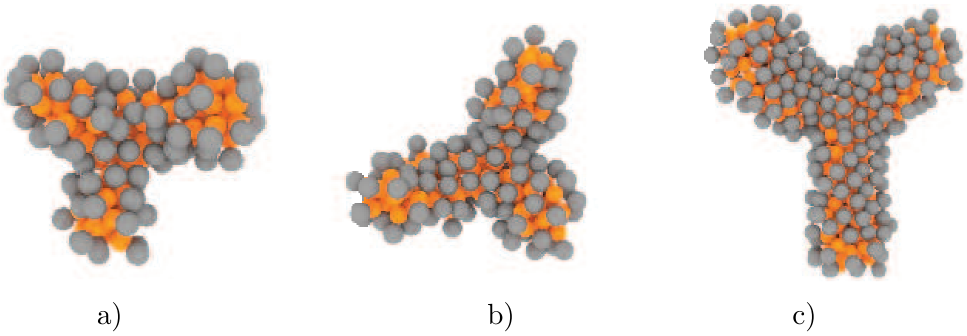

Figure 6.25: Twisted (a) and branched (b) structures obtained from $\alpha = 0.8$, $T^* = 0.2$, and $\rho^* = 0.2$. The branched structure in (b) is a single continuous cluster percolated across the simulation cell with $N_s \approx 1000$.

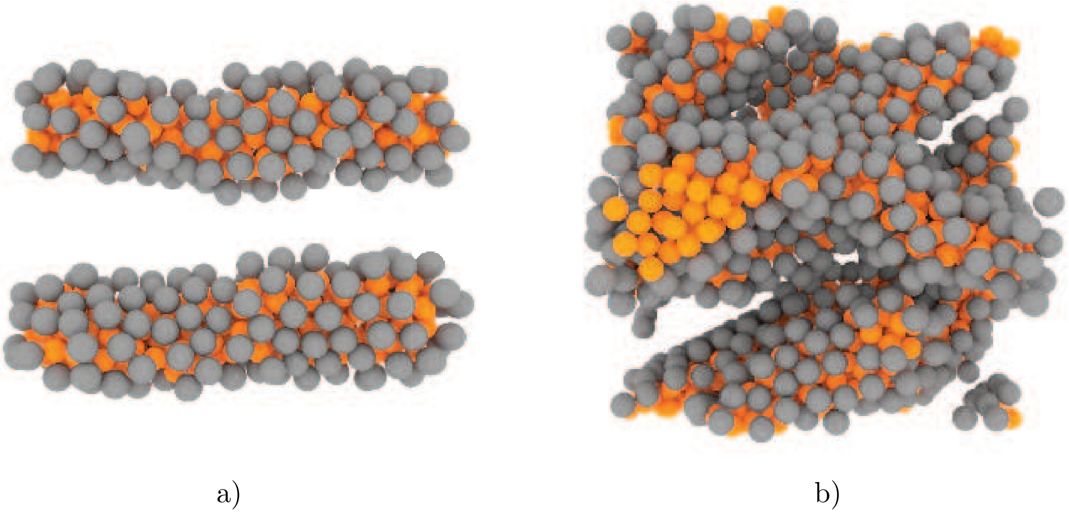

Figure 6.26: Structures with a small degree of branching where $\alpha = 0.8$.

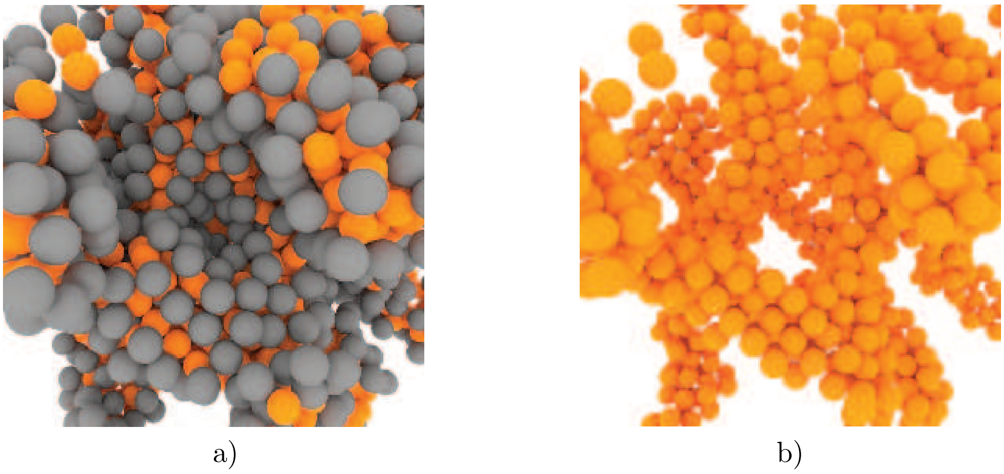

Figure 6.27: A network structure where $\alpha = 0.85$, $T^* = 0.25$, and $\rho^* = 0.20$; with (a) and without (b) h sub-particles to demonstrate the bonding network.

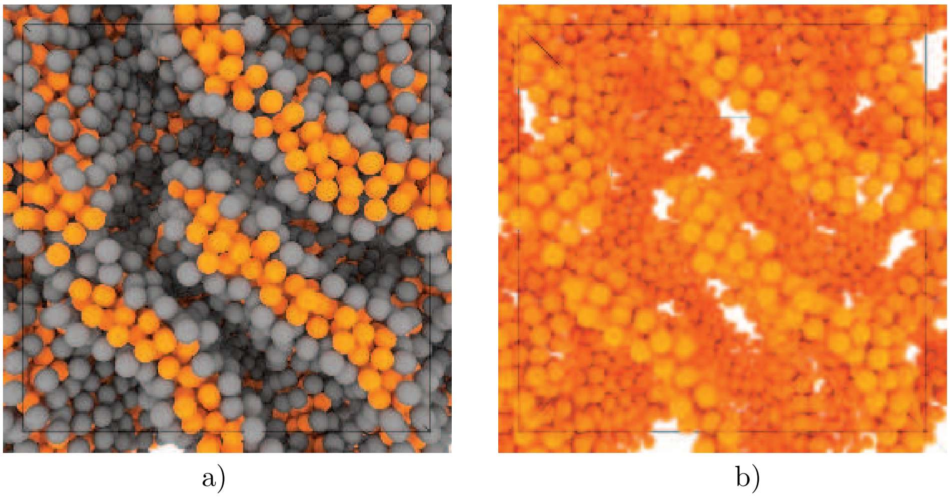

FIGURE 6.28: A sponge structure where $\alpha = 0.9$, $T^* = 0.25$, and $\rho^* = 0.20$; with (a) and without (b) h sub-particles to demonstrate the bonding network. In both of these images ambient occlusion has been employed in the render to highlight the depth.

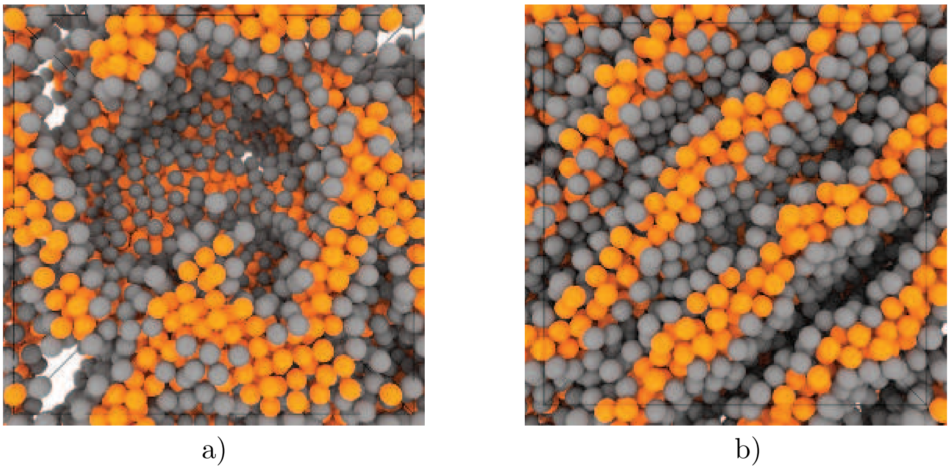

FIGURE 6.29: A sponge structure where $\alpha = 0.95$, $T^* = 0.20$, and $\rho^* = 0.25$ (a), and a lamellar structure at $\rho^* = 0.30$ (b) h. In both of these images ambient occlusion has been employed in the render to highlight the depth.

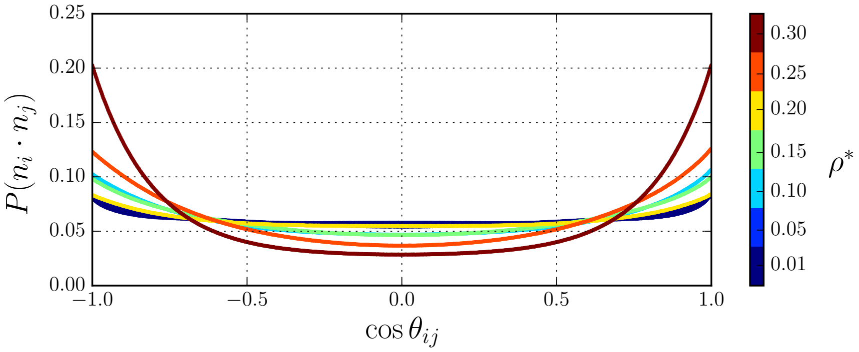

FIGURE 6.30: Distributions of $P(n_i \cdot n_j)$ at different ρ^* across $T^* = 0.2$ where $\alpha = 0.95$. Here the increasingly quartic distribution demonstrates the density driven formation of lamellar structures.

6.4 Structural Diversity $\alpha > 1$

On the other side of the Janus limit, for $\alpha > 1$, where the s sub-particle is larger than the h sub-particle ($\sigma_s > \sigma_h$), the SA protocol was applied to investigate the assembly of phases below the gas-liquid phase separation region indicated in Figure 6.5. Over the region $1 < \alpha < 1.3$, we document the variation in the phase behaviour as one of either vesicles, tubes, gyroid, lamellar, or cavity liquid, all of which except for the cavity liquid are bilayer structures. It is important here to note that these structures are all locally similar, i.e. the environment around each particle is approximately the same. Therefore each of these structures: vesicle; tube; wave, gyroid; lamellae; are all bilayer structures differentiated by their topology. At least 3 different simulations are performed at each state point (indicated in Figure 6.5). All of these simulations were performed in cubic boxes with $N = 1000$ HJDs and periodic boundary conditions. Systems that form continuous structures will be constrained to have a characteristic length similar to the box dimensions (as mentioned in Chapter 5). Due to this fact we tentatively assign the phase based upon the general environment around each particle.

Structures which are found, whether they are vesicles, percolated tubes, or some other continuous structure, that are composed of some complicated network of bilayers, are referred to simply as ‘bilayer structures’. Where the system adopts some other structure say a liquid with cavities, this is referred to as a cavity liquid (a cavity liquid may also be called reverse micelles, though the term usually refers to the micellisation of water in oil emulsions, and since the “solvent” is indirectly modelled via the interaction potential and the location of each philos, thus in a high concentration suspension of this kind of particle it is imprecise to use the term reverse micelle). Though arguably a bilayer and a cavity dominated structure share some similar characteristics, the differences pertain mainly to the variation in their local structure. For example, a cavity liquid will contain at least two distinct particle environments: dissolved in the bulk; and at a cavity interface. Whereas a system composed of bilayers, whatever the global topology, the local structure around each particle will be approximately the same. Another caveat one must also bear in mind here is that the effect of the geometry of the periodic box on the outcome of a simulation is essentially one of confinement. Since all simulations are carried out in periodic boundary conditions if a bilayer structure is to bond with its next periodic image, the maintenance of the bond network will exert an influence on the topology of the structure that forms. Again this type of kinetic trapping, addressed briefly at the end of the previous chapter (Chapter 5), favours structures which form first, or which percolate first.

Some state-points reliably return a particular topology. This is especially true of state-points where low ρ^* vesicles, single percolated bilayers, and is often the case where gyroid-like, and high ρ^* lamellar structures are observed. At intermediate ρ^*, there is the possibility the formation of a vesicle, tube, or a single bilayer structure can form by whatever happens to form first. These regions are identified and marked as such in Chapter 7. Unfortunately, in this region the metrics we have employed are inadequate to characterise the differences in structures obtained. We proceed by displaying snapshots of some structures observed here. We highlight state-points where simulations give results which have conflicting outcomes.

6.4.1 Lamellae and Cavities

We begin by discussing the two extremes of the α space where self-assembled structures are observed. Where $1 < \alpha = 1.1$, as highlighted in Chapter 4 and Chapter 5, the phase behaviour is dominated by bilayer structures which are finite at low ρ^*, but percolate and form ordered lamellae at high ρ^*. Where $\alpha = 1.3$ a cavity liquid is observed. A snapshot of a lamellar structure and cavity liquid is presented in Figure 6.31 for comparison. Panel (b) particular snapshot possesses an obvious finite size effect — a cylindrical void that has percolated across the boundary of the cell — chosen purposefully to demonstrate the two distinct particle environments[2]. As mentioned above two particle environments can be observed in the cavity liquid, whereas the lamellar phase possesses local similarity everywhere. On cooling of the cavity liquid in the density interval underneath the coexistence region the cavities become more pronounced.

6.4.2 Vesicles and Tubes

In the space of $1.1 < \alpha < 1.3$ at $\rho^* < 0.1$, the system can adopt two topologically different curved structures. Vesicles, which at high T^* coexist with a gas, but at low T^* contain all of the particles in the system, are observed. At vesicle forming α, all structures obtained at $\rho^* = 0.01$ are vesicles. Where ρ^* is increased toward 0.05, the system can percolate and there is some ambiguity as to what structure the system prefers. Taking the cross section of these structures demonstrates that they are essentially similar, except for the fact that the tube has percolated and thus has a different topology. Snapshots of a tube and a vesicle structure showing the internal structure and an ‘end on’ perspective are displayed in Figure 6.32.

---

[2] Contrast the image in panel b) of Figure 6.31 with that of the finite size effects in panel f) of Figure 5.9

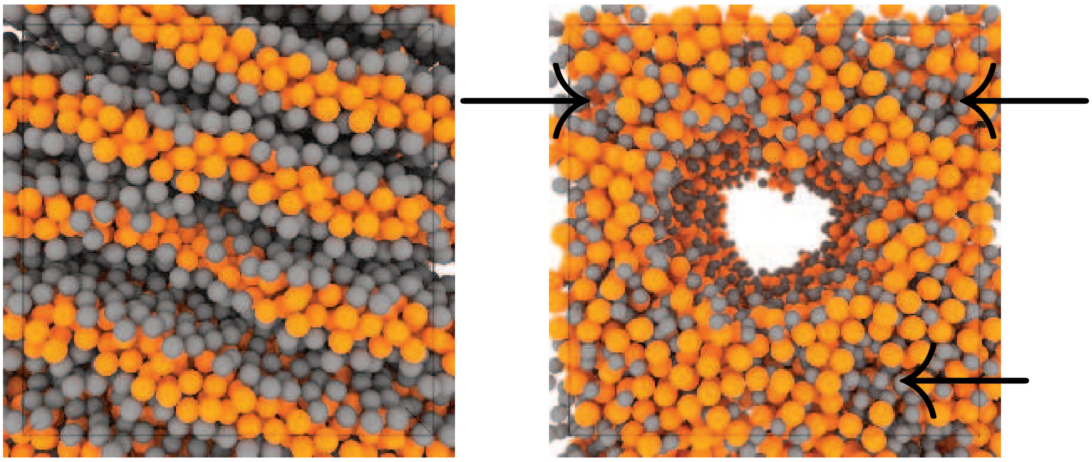

a) b)

FIGURE 6.31: A lamellar structure where $\alpha = 1.05$, $T^* = 0.3$, and $\rho^* = 0.3$ (a), and a cavity liquid where $\alpha = 1.3$, $T^* = 0.4$ and $\rho^* = 0.3$ (b). Arrows on the figure indicate the location of cavities collecting h sub-particles *en-masse* in the liquid. The finite size effect — the percolated void (referred to as a cylindrical bubble in Chapter 5) — enables viewing of the orientation of HJDs at the interface of the bubble.

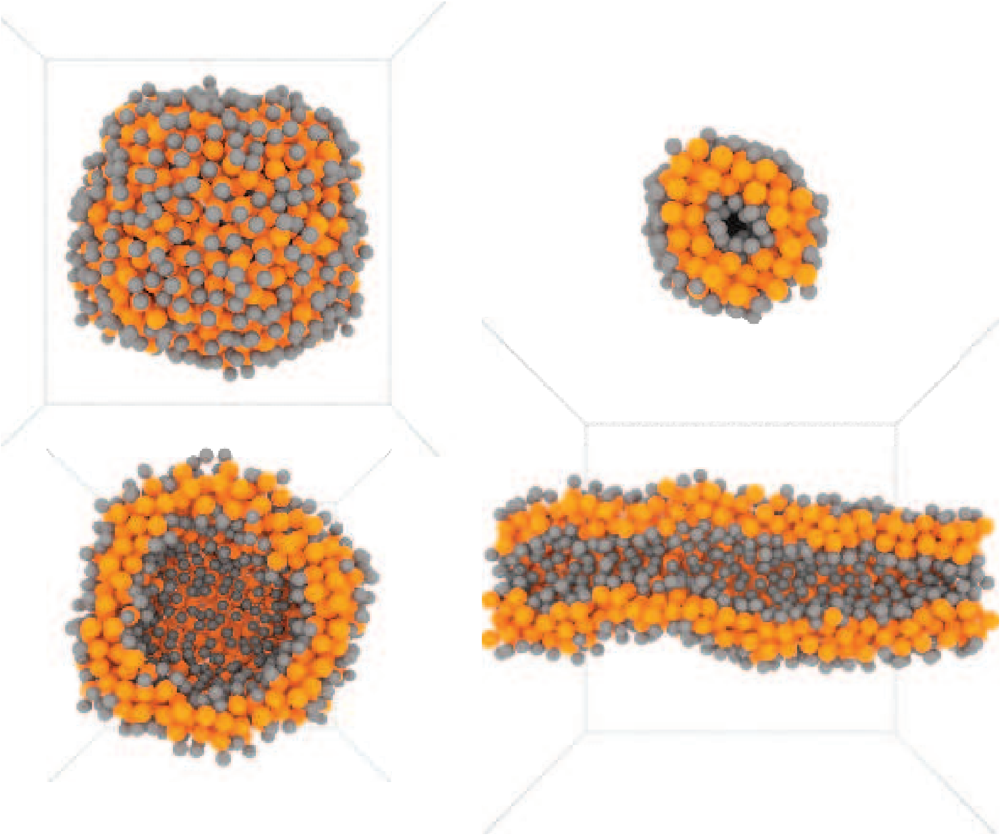

a) b)

FIGURE 6.32: A vesicle structure from outside (top) and a cross-section (bottom) where $\alpha = 1.25$ depicted in panel a); Tube structure observed at the same state-point in a duplicate simulation, 'end-on' (top) and a cross section (bottom) depicted in panel b).

6.4.3 Bilayers and Gyroids

It has been demonstrated that amphiphillic molecules can form gyroid like structures in lipids, block co-polymers and in simulation [88–91], but also in simulation of soft, asymmetric dumbbell shaped colloids [92]. Here we observe two other types of structure topologically distinct from the vesicle, tube, planar bilayer (termed here 'lamellar'). Bilayers that form where $1.1 < \alpha < 1.3$ can tolerate significant curvature. This can already be observed in the case of the vesicle and tube structures observed above. In Figure 6.33, snapshots of structures consisting of a single wave-bilayer (with wavelength proportional to the box length), a bilayer with an bridge join, and a gyroid-like structure can be viewed. The gyroid structure is not exactly a minimal curvature surface. Two orthographic[3] snapshots from $\alpha = 1.2$ and $\alpha = 1.15$ can be seen in Figure 6.34. These structures are all strongly affected by the cubic box geometry. Additional work needs to be done to ascertain the stability of these structures with respect to compression and variable box dimensions (see Chapter 8). It is likely that an NPT simulation with variable box lengths may yield results that differ slightly from the present study. It is unclear at this stage what structure they may take. It can be stated without ambiguity that the structure of state-points, whatever the final box geometry, that form at these low temperatures will be composed of percolated bilayers, and, since the dumbbell geometry here allows the surface to have some curvature while still maximising the number of bonds per particle, it is likely that structures such as the gyroid and other bi-continuous structures will be observed.

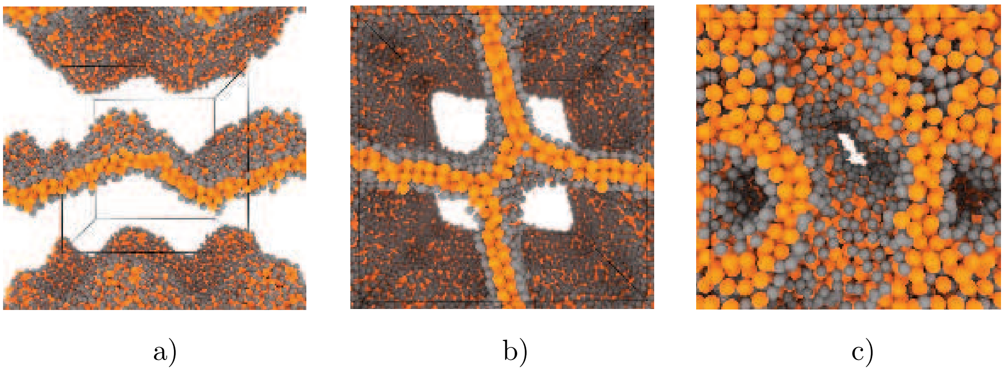

FIGURE 6.33: Structures obtained across the $T^* = 0.3$ isotherm where $\alpha = 1.2$: A wavy bilayer structure, panel a); a wavy bilayer with a bridge, panel b); and a bi-continuous gyroid-like structure, panel c).. Periodic images are included for clarity. The size of each simulation cell is indicated in each panel by the black cube.

---

[3] an orthographic projection allows us to view the continuous cavities formed by 3D void percolation on a 2D surface

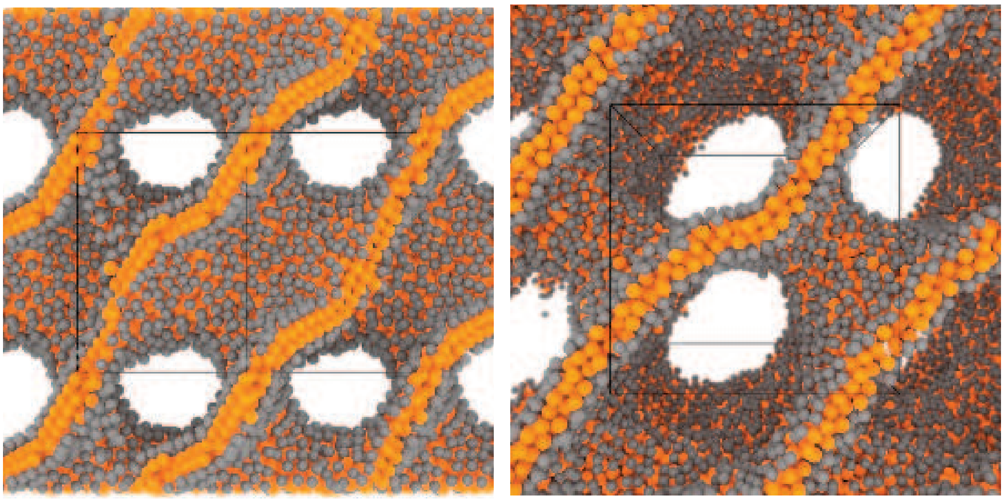

a) b)

Figure 6.34: Gyroid-like structures formed by void percolation. Panel a) is from $\alpha = 1.2$, where focal point for the orthographic snapshot cell edge. Panel b) is from $\alpha = 1.15$, where cell is face-on.

6.4.4 Crystalline Order at Low Temperature

Where $T^* = 0.3$, $\mathbf{g}_{ss}$ indicates fluid local structure around the s sub-particles at both $\rho^* = 0.1$ and $\rho^* = 0.3$. Upon lowering the temperature from $T^* = 0.3$ to $T^* = 0.2$ across all $\alpha > 1.05$ bilayer systems develop crystalline order around each s sub-particle. Figure 6.35 demonstrates the formation of additional peaks in the low temperature fluid on cooling. The local structure observed on cooling is related to the local structure observed in the strip, platelet, and lamellar structures observed where $\alpha < 1$ (compare panels 2 and 4 of Figure 6.35, with panel 2 of Figure 6.21). Bond-wise distributions of q_6 can be viewed in Appendix C.

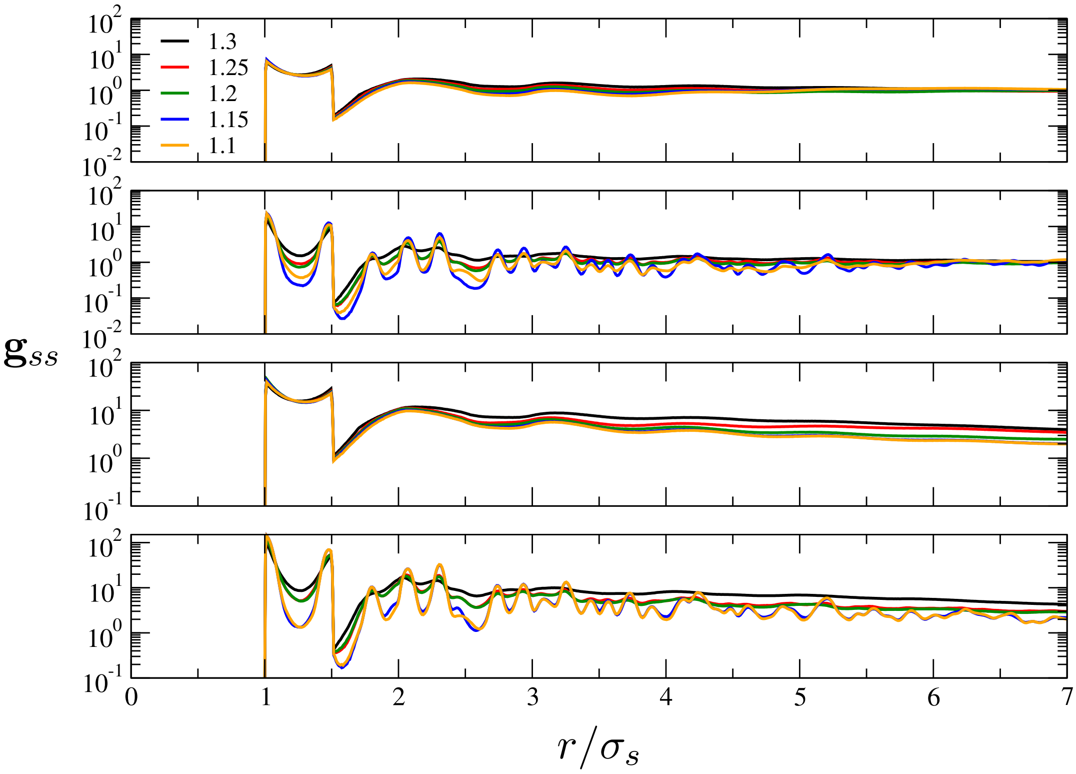

FIGURE 6.35: Demonstration of crystalline order developing in the low temperature fluid across $1.1 \leqslant \alpha \leqslant 1.3$ (indicated in the top panel). The top two panels collect $\mathbf{g}_{ss}$ collected at $\rho^* = 0.3$ for $T^* = 0.3$ and $T^* = 0.2$, respectively; and the bottom two panels collect $\mathbf{g}_{ss}$ collected at $\rho^* = 0.1$ for $T^* = 0.3$ and $T^* = 0.2$, respectively. Where $T^* = 0.3$, at all α considered on the plot the self-assembled structures clearly demonstrate fluid order. The formation of structure in $\mathbf{g}_{ss}$ on cooling from $T^* = 0.3$ to $T^* = 0.2$ indicates that the local bonding structure around each s sub-particle is highly ordered.

Chapter 7

Phase Diagrams

This relatively short chapter concentrates on phase diagrams developed based on the results of Chapter 4, Chapter 5, and Chapter 6. Based upon Chapter 4, we apprehend that the point at which the system reaches the Janus limit (i.e. $\alpha = 1$, or equivalently $\sigma_s = \sigma_h$) the system adopts primarily planar bilayer structures. This α is used as a reference point that connects the two regions of α above and below $\alpha = 1$ where the phase behaviours are observed to be distinctly different. Broadly, above $\alpha = 1$ systems can be classified with respect to their proximity to liquid forming region where $\alpha \gtrsim 1.15$, and layered structures where $\alpha \lesssim 1.3$. The region $1.15 < \alpha < 1.3$ is a region where competition between layered assemblies and gas-liquid coexistence occurs at low T^*, and on further cooling a number of different self-assembled phases which become increasingly planar as $\alpha \to 1$. The region where $\alpha < 1$, we observe several different phase scenarios consisting of 3D, 2D, and 1D aggregate systems. These are categorised as sponge, network, lamellar, platelet, strip, and micelle, in order of decreasing dimensionality.

7.1 Phase Categorisation

Due to the complex nature of aggregates observed, the multi-pronged approach to phase identification outlined in the previous chapter is employed. Where an ambiguity is encountered, say, for an $\alpha < 1$ where there is little orientational order but where $N_{largest}$ the state-point shows that the system is one large structure, visual inspection of configurations is employed to decide what phase the state-point has adopted. This process can be facilitated by inspecting the bonding network. Where an ambiguity does occur, the interpretation based on a visual inspection is preferred.

7.2 Phase Diagrams $\alpha < 1$

7.2.1 Reading Phase Diagrams

Phase diagrams for $\alpha < 1$ are given a form consistent with the array of T^* and ρ^* studied at each α (see Figure 6.5). All phase diagrams have the proportions $T^* \in (0.05, 0.35]$ and $\rho^* \in [0, 0.3]$. Each state-point is assigned a rectangle in this space and coloured according to the phase observed. Regions which possess no colour were not investigated in the present study. The colour assigned to each phase is displayed on the right hand side in each case for quick reference. Rectangles which contain two colours indicate a state point where two different structures are observed, sometimes in coexistence. Indicated on each phase diagram is a line marked in red below which an ordering transition takes place. This ordering transition line identifies a temperature below which additional peaks resolve in the radial distribution function over the σ_s sub-particles $\mathbf{g}(r)_{ss}$ (see Figure 7.1 in red). Regions marked percolating are regions above where structure can be observed in the $\mathbf{g}(r)_{ss}$, but where the system still displays clustering that connects to its next periodic image through the bond network. Descriptions and snapshots of each type of structure can be obtained from Chapter 6. Similar phase diagrams from adjacent values of α are contained in Appendix A.

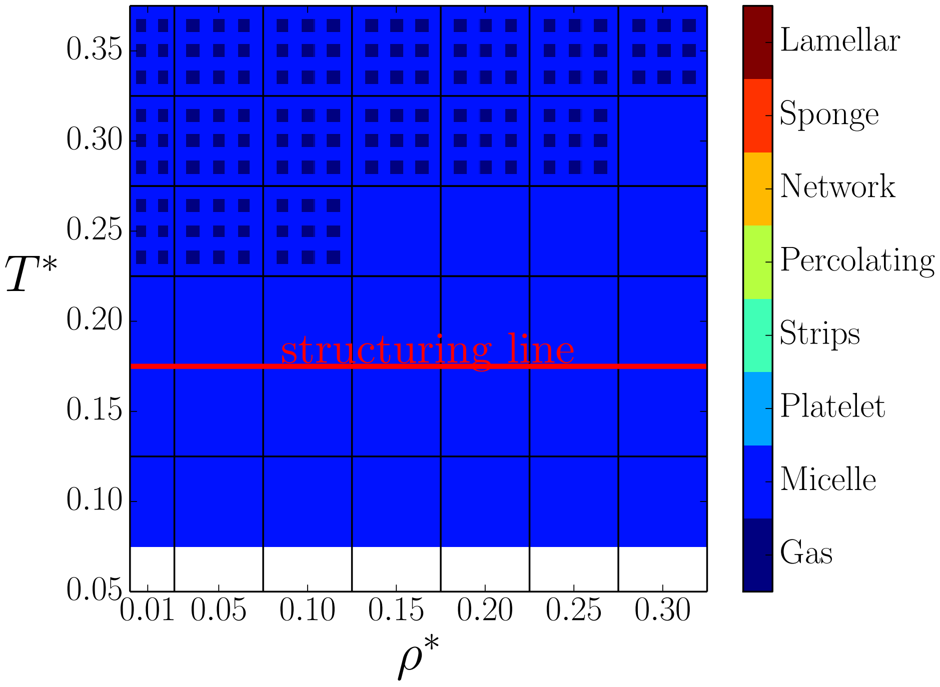

FIGURE 7.1: Phase diagram for $\alpha = 0.65$. At high temperatures a gas coexists with approximately spherical micelles, on lowering the temperature. Regions with two colours indicate a state-point where structures are found to co-exist. The red line indicates the T^* below which additional peaks can be observed in the radial distribution function.

Figure 7.1 depicts the phase diagram for $\alpha = 0.65$. Here a gas at high T^* coexists with micelles, which eventually, on cooling past the red line (below $T^* = 0.20$) form what appear to be crystalline clusters. No continuous structures are observed.

Figure 7.2 depicts the phase diagram upon increasing the s sub-particle to 2/3 of the h sub-particle diameter. Here, below the red T^* line, micelles are found to coexist with platelet structures at all densities studied. At high T^* the system is similar to the case where $\alpha \leqslant 0.65$. The structural differences between micelles and platelets can be viewed in Chapter 6.

Where $\alpha = 0.75$ (depicted in Figure 7.3), the high T^* scenario is characterised by a monomer gas coexisting with micelles which at higher ρ^* elongate and eventually percolate where $\rho^* \gtrsim 0.25$. Below the red line, where $T^* \leqslant 0.2$, The system undergoes three regions where different structures are observed. Firstly, a gas of micelles co-exist with platelet structures where $\rho^* < 0.15$. Strip structures are observed to coexist with platelets between $0.10 < \rho^* < 0.25$. At $\rho^* = 0.25$, the platelet population is depleted and solely strips are observed some of which have percolated. This percolated strip phase occurs around the same density as percolation in the less ordered fluid above the

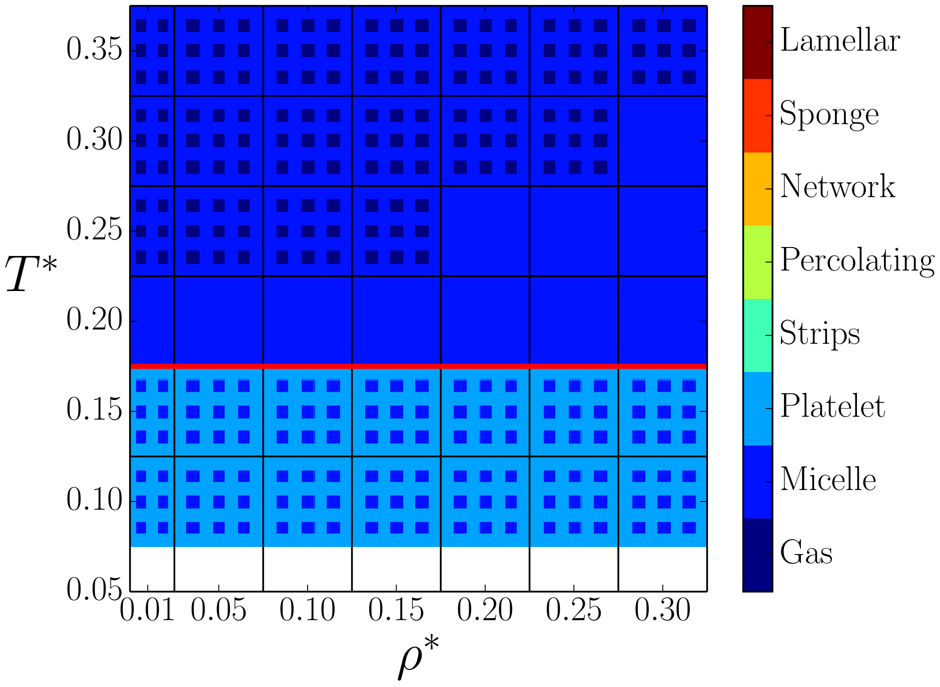

FIGURE 7.2: Phase diagram for $\alpha = 2/3$. Here below the red line the formation of platelets occurs in co-existence with micelles. This is the first instance of platelet formation observed in the simulation set.

red-line indicating that it is density-confinement driven process. A case study of this α can be found in Chapter 6.

Where $\alpha = 0.8$, the phase diagram is qualitatively similar to $\alpha = 3/4$. A micelle gas coexisting with monomers at high T^* and low ρ^*, changing to a pure elongated micelle phase before the system percolates at $\rho^* = 0.2$ for all $T^* > 0.2$. Below the red line, coexisting micelles and platelets give way to platelets and strips at $\rho^* \approx= 0.15$ for all $T^* < 0.25$, with the exception of $T^* = 0.1$, where this occurs earlier and yields a pure strip phase at $T^* = 0.2$. By $\rho^* = 0.15$, all $T^* < 0.25$ have adopted a platelet and strip coexistence, which ends at $\rho^* = 0.25$ where all $T^* < 0.25$ have adopted the network structure. The first appearance of networks of branching curved structures is observed at a slightly lower α (see Appendix A). Snapshots of some structures here are depicted in Chapter 6. This particular α has been studied elsewhere [55], which addresses the effect of sphere separation on the self-assembly products. In this case the sphere separation is such that the s sub-particle is extruded from the h sub-particle up to a sphere separation of $l \approx 0.5$ (see the discussion in Section 1.5). It is observed that as the sphere separation is increased, the formation of spherical and elongated micelles eventually gives way to bilayer structures at higher ρ^*, although the authors employ a single temperature (parameterised as an attraction strength $\beta\varepsilon = -3.58$) to observe

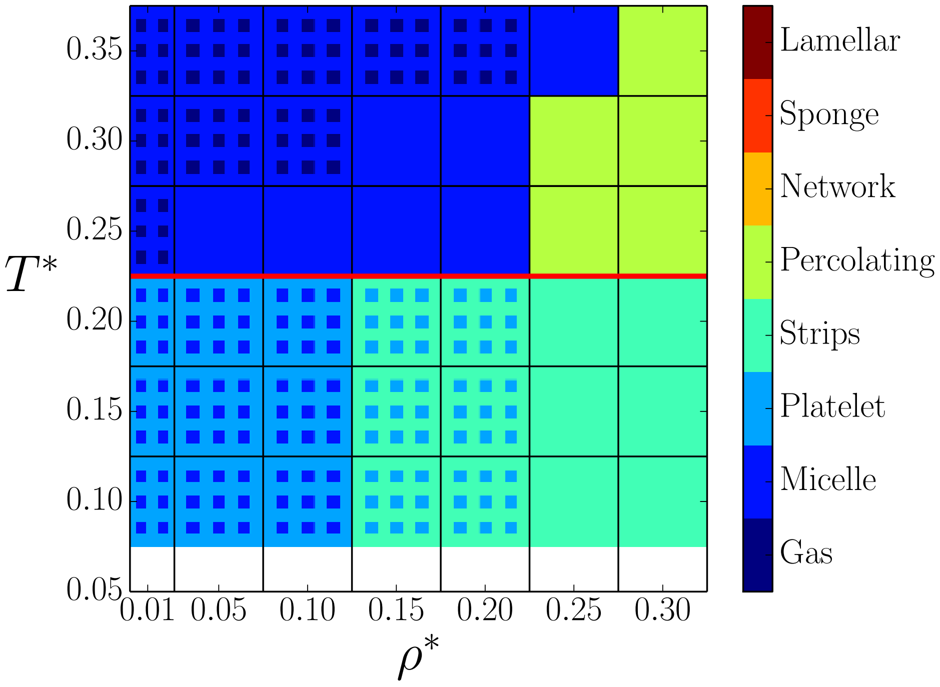

FIGURE 7.3: Phase diagram for $\alpha = 0.75$. Above the structuring line (in red) a monomer gas coexists with micelles which at high density percolates. Below the red line ($T^* < 0.225$) a density drive transition from elongated micelles co-existing with platelets, then platelets co-existing with strip structures are observed.

assembly which is equivalent to $T^* = 0.27$. No strips or strip-network structures are observed in [55]. The reason for this is likely two-fold. Firstly the temperature employed is too high to observe the formation of ordered strips, since the T^* at which strip order is observed in the current study ($T^* < 0.25$) is just below temperature backed out from their attraction strength parameter ($T^* = -1/\beta\varepsilon \approx 0.279$). Secondly, it may also be the case that only the extrusion of the s sub-particle toward a tangent dumbbell allows branching to occur since the variety of bond angles is increased by having a larger portion of the sphere available for bonding in the present parameterisation, given that in [55] the l parameter was only varied over $0 \lesssim l \lesssim 0.5$. While the results agree qualitatively that the formation of micellar aggregates occur here, in the present study the interesting structured aggregates fall on the diagram at a lower temperature.

By $\alpha = 0.85$, the percolation of strips has shifted to far lower $\rho^*(= 0.05)$, the red line has shifted to higher $T^*(0.2 < T^* < 0.25)$, and the network region has expanded to fill almost half of the studied region below the red line. Strips here are characterised as having wider small diameter owing to a larger close-packed stacking arrangement, and the network structures possess more curvature. The percolation threshold at T^* above

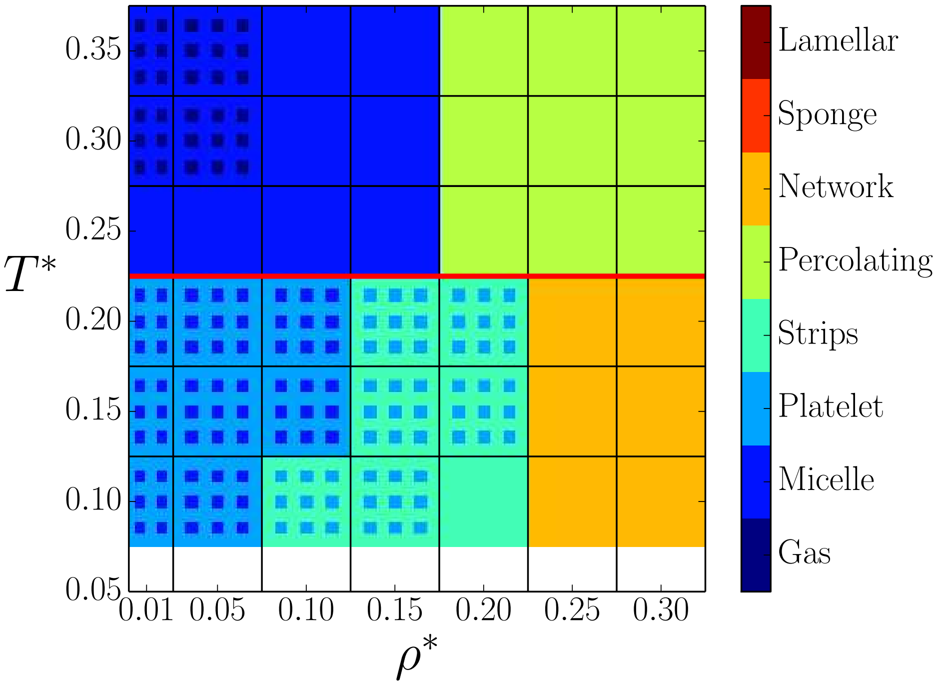

Figure 7.4: Phase diagram for $\alpha = 0.8$. Here the percolation region has advanced to lower ρ^*, the low T^* behaviour now includes the presence of branching network strips.

the red line has shifted to between 0.01 and 0.05. The phase diagram for $\alpha = 0.85$ is depicted in Figure 7.5.

Where $\alpha = 0.9$, the appearance of sponge structures (which emerge where $\alpha = 0.875$, see Appendix A) begin to occupy a large portion of the phase diagram (Figure 7.6). The percolation threshold hasn't moved from the case where $\alpha = 0.85$. Regions of previous diagrams where strip structures are found have been squeezed out be the formation of networks. By $\alpha = 0.925$ the strip structures do not occur on the phase diagram, replaced by platelet regions and networks. Eventually, by $\alpha = 0.95$ (Figure 7.7), lamellar structures begin to dominate the phase diagram. This trend continues until $\alpha = 1$, where only lamellar structures are observed.

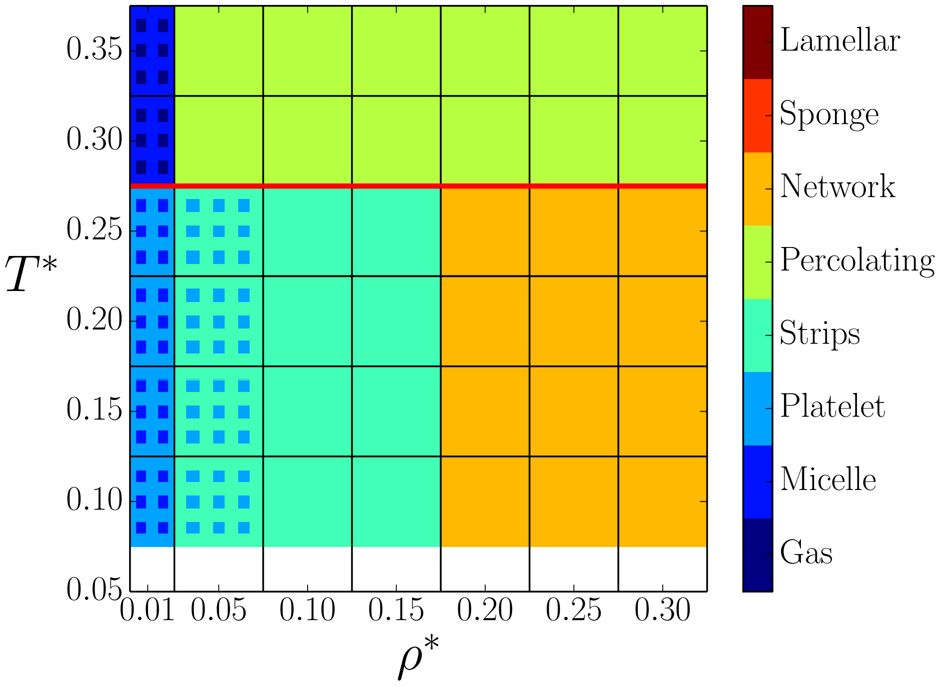

FIGURE 7.5: Phase diagram for $\alpha = 0.85$. Here the percolation region has advanced to between $0.01 < \rho^* < 0.05$. Below the structuring line nearly half of the state-points are branching networks. The presence of strips has also moved to lower ρ^*.

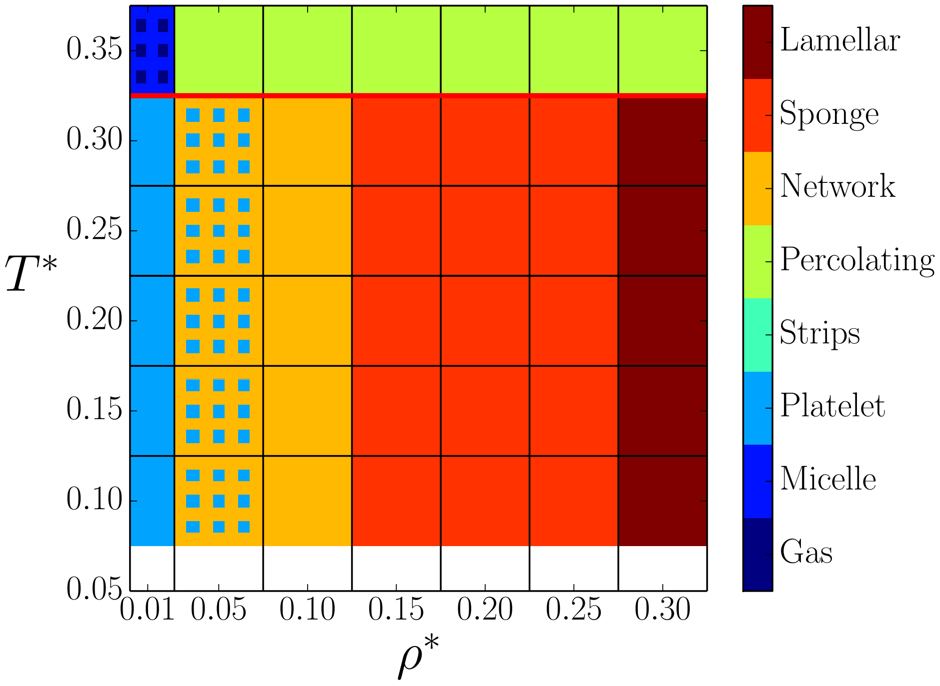

FIGURE 7.7: Phase diagram for $\alpha = 0.95$. Here the presence of elongated micelles below the structuring line has vanished, replaces by solely platelets. At higher ρ^* lamellar order has developed.

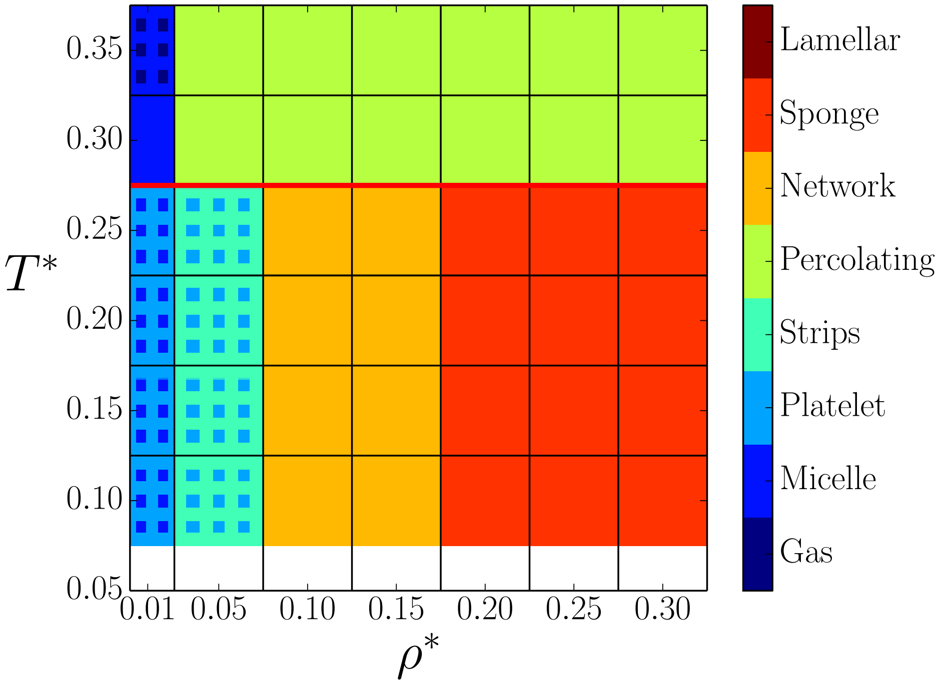

FIGURE 7.6: Phase diagram for $\alpha = 0.9$. By this α sponge-like order (in orange) has developed in the low T^* region. This is one of the most complex α studied. Consisting of gas, spherical micelles, and percolation at T^* above the structuring line; and elongated micelles, platelets, strips, branched networks, and sponge-like order below in increasing ρ^*.

7.3 Phase Diagrams where $\alpha > 1$

As mentioned in the preceding analysis set out in Chapter 5 and Chapter 6, beneath the gas-liquid phase coexistence region on the interval $1.1 < \alpha \lesssim 1.3$[1] the formation bilayer structures begins to perturb the liquid structure. As the system is cooled past the coexistence region cavities formed by the collection of h sub-particles eventually yield large percolated voids between bilayer structures. Since the region under the coexistence curve is dominated by finite size effects (see Section 5.5.2 and the analysis in Chapter 6) tentative phase diagrams are presented here demonstrating the location of bilayer structures and their topology in conjunction with the gas-liquid binodal. On each of the three (for $\alpha = 1.3$, 1.2, and 1.1) phase diagrams are the approximate temperature below which the system begins to display significant cavitation, denoted by a green dotted line; where the system is dominated by bilayer structures — whatever the topology — denoted by the blue dotted line; and finally the temperature of onset of crystalline order in the bilayer structures (see Section 6.4.4) a red dotted line, below which additional peaks in $\mathbf{g}_{ss}$ emerge, and bond-wise distributions of q_6 indicating a

---

[1] Additional diagrams of the structures observed at each state-point can be found in Chapter **??**

significant proportion of the system has adopted relatively high coordination numbers and that these particle environments have only a few specific spacial arrangements of neighbouring particles. The temperature of onset of the the cavity liquid line, and the bilayer line are extracted from the analysis in Chapter 5. For $\alpha = 1.2$ and $\alpha = 1.1$, where bilayer structures are observed, the outcome of the simulated annealing simulations is superimposed on the phase diagram to demonstrate where these structures may lie on the phase diagram, pending the demonstration that they not meta-stable to the formation of some other structure. Figure 7.8 contains the proposed phase diagram for $\alpha = 1.3$. Here the critical point is estimated at $T_c^* \approx 0.608$, $\rho_c^* \approx 0.185$, beneath which a region of gas-liquid coexistence, which on cooling begins to display significant cavitation at $T^* \approx 0.44$. Upon lowering the temperature below $T^* \approx 0.25$, the system is observed to demonstrate crystalline order. Decreasing α to 1.20 (Figure 7.9), the critical point has shifted to $T_c^* \approx 0.520$ and $\rho_c^* \approx 0.132$. Again at $T^* \approx 0.44$ significant cavitation occurs in the fluid, only this time the formation of bilayer structures occurs below $T^* = 0.42$. Across the isotherms $T^* = 0.4$ and $T^* = 0.3$ different topologies of bilayer structures are observed. These are categorised according to the method described in Chapter 6. They include vesicle, tubes, lamellar bilayers, and gyroid -like structures. Further along where $\alpha = 1.1$ (Figure 7.10), no liquid is observed only self-assembled bilayer structures are observed, including vesicles and bilayers. Here the projected critical point is approximately coincident with respect to the formation of bilayer structure. A progression of the critical point to be metastable with respect to the formation of bilayer structures at this α is consistent with the lack of observation of a gas-liquid critical point for $\alpha = 1$ (and $\varepsilon_h = 0$) in Chapter 5.

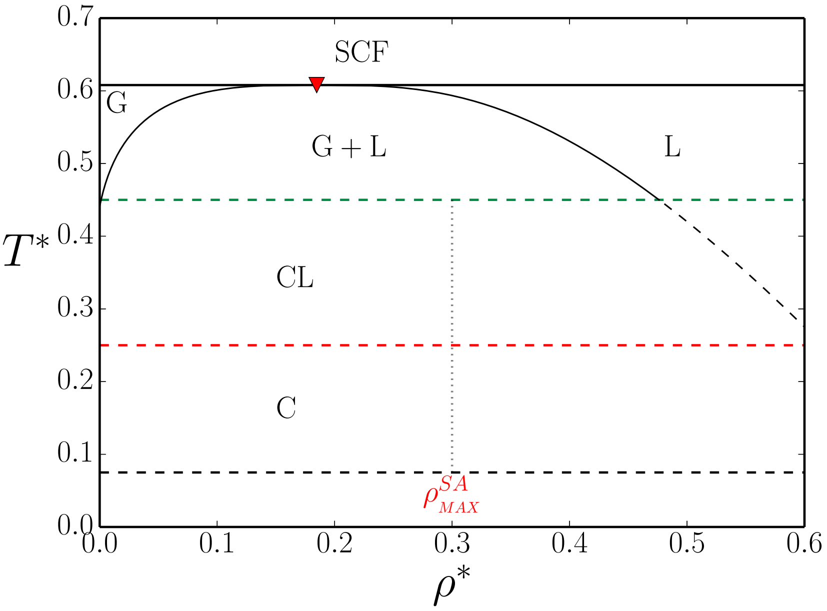

FIGURE 7.8: Phase diagram for $\alpha = 1.3$. Regions include the super-critical fluid (SCF) at high temperature, gas (G), liquid (L), gas-liquid coexistence region (G+L), a cavity liquid region (CL), and crystalline (C) region. The vertical grey line marked ρ^{SA}_{MAX} denotes the ρ^* past which no SA simulations were performed.

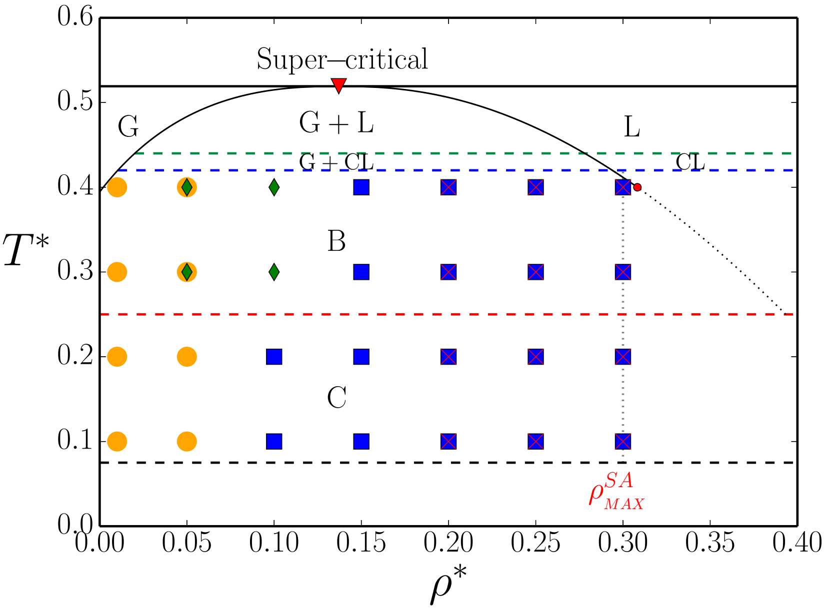

FIGURE 7.9: Phase diagram for $\alpha = 1.2$. Regions include the super-critical fluid (SCF) at high temperature, gas (G), liquid (L), gas-liquid coexistence region (G+L), a cavity liquid region (CL), bilayer region (B), and crystalline (C) region. The dotted vertical grey line marked ρ^{SA}_{MAX} again denotes the ρ^* past which no SA simulations were performed. The self assembled phases denoted by the symbols are vesicles (orange circles), tubes (green diamonds), lamellar bilayers (blue squares) and gyroid-like (red crosses). state-points with two symbols are where the structure obtained via SA was either one.

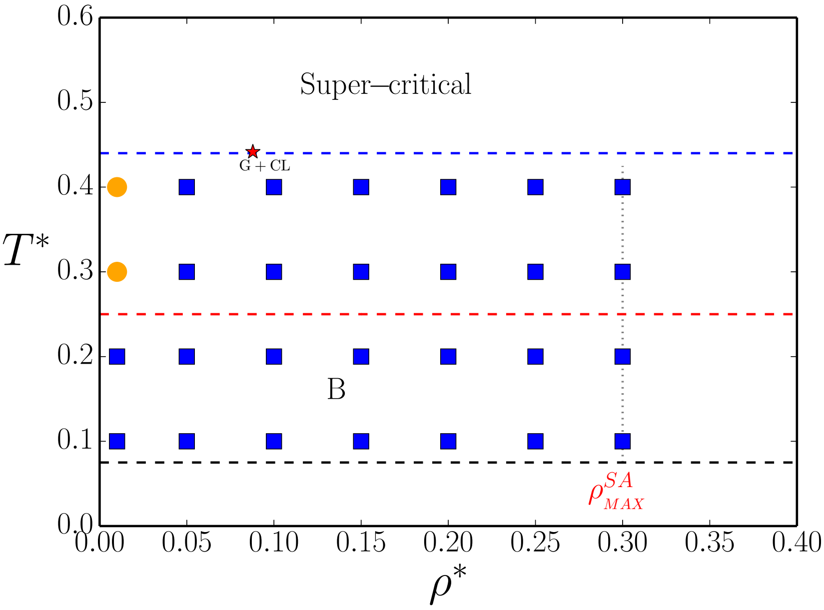

FIGURE 7.10: Phase diagram for $\alpha = 1.1$. No gas-liquid phase behaviour is observed here, the projected critical point, denoted by the red star symbol is above the region where simulations are performed, yet no binodal was observed here. The bilayer structure observed in the simulated annealing points are vesicles (orange circles) and bilayers (blue squares).

Chapter 8

Conclusions

We advance a model of colloidal dumbbell shaped particles with strongly anisotropic interaction that is sufficiently simple as to become tractable for numerical study and yet sufficiently complex to demonstrate a wide array of phase behaviours controlled by fairly simple relationships between particles. It has been suggested [35] that this kind of investigation can be performed at "different levels of realism", with this one likewise corresponding to an "extreme coarse graining procedure". It is evident that only rather elementary descriptions of particle geometry, interaction potentials, and methodological approaches can be employed to yield very rich and diverse phase behaviours. In this light we combine the hard-sphere model, which undergoes a first order phase transition from a fluid to a crystal upon compression; and the square well model, which demonstrates all the phase behaviours of classical matter: gas-liquid critical phenomena. A Numerical study of the phase behaviour of "tangent dumbbells", consisting of two spherically symmetric interaction sites, was performed via exploration of two orthogonal pathways from three reference systems to the Janus limit, where both constituent sub-particles have equal diameter ($\sigma_h = \sigma_s$) and the attractive interaction strength on one site is naught (i.e. $\varepsilon_h = 0$). Firstly via a gradual reduction or 'tuning' of the interaction strength on the site of a SW dumbbell, via an interaction strength parameter ε_h. Secondly via inflating the size of a hard-sphere sub-particle, tangent (i.e. where the internuclear distance is half the sum of the diameters) to a square-well sub-particle, to the Janus limit (with equal diameter sub-spheres), and subsequently shrinking the square-well sub-particle to leave solely a hard-sphere. This interaction site size ratio is controlled by the sphere size ratio parameter α. Gas-liquid coexistence curves are computed from two reference points which contain a liquid phase i.e. from the square-well tangent dumbbell, and from the square-well sphere up to a point near the Janus limit. Several interesting phase scenarios are observed in this regime.

8.1 Square-well dumbbells to the Janus limit

Two main observations are presented in which it is demonstrated that the increase in anisotropy of the interaction potential drives the self-assembly of certain structures which compete with the formation of a liquid. Firstly, due to the reduction in volume of the interaction potential as the interaction site on one sub-particle is ‘tuned’ to 10 % of the other, the critical temperature reduces linearly consistent with a mean field theoretic approach [57], and the critical density becomes very small such that at the Janus limit ($\sigma_s = \sigma_h$) $\rho_c^* \to 0$ and the gas-liquid critical point becomes metastable with respect to the formation of self-assembled structures. The dominant self-assembled phase observed in the low temperature fluid is lamellar. We advance the argument that as the interaction potential becomes more anisotropic, that the formation of lamellar self-assembled structures dominates the phase behaviour.

8.1.1 Heterogeneous Janus dumbbells

Finite low density self-assembled structures where interaction anisotropy parameter $\varepsilon_h \to 0$, referred to in Chapter 4 as micelles, may be the result of kinetic trapping due to an inability to diffuse across the simulation cell. Given that self-assembled phases are expected to abound in the HJD, where $\varepsilon_h = 0$, a non-local intra-box swap move algorithm — a version of Aggregation Volume Bias Monte Carlo — is implemented to avoid, or at least reduce the effects of the kinetic bottlenecking on the study of particle systems across α. It is observed via the parameterisation developed here for the tangent HJD that solely via tuning of the composite sphere sizes that variegated phase behaviours can be obtained. For $\alpha < 2$ these include typical and atypical gas-liquid phase separation (considering the critical exponents and their relation to the Ising universality classes); low density percolation thresholds caused by the formation of self-assembled bilayer structures, which we variously categorise as vesicles in the ultra-low density regime, tubes and waves in the low to moderate density regime — where the box size has allowed percolation to occur, and the system is essentially under a percolation enforced confinement — gyroids where the system is essentially bi-continuous at moderate densities, and lamellar where multiple layer stacking coexist at moderate to high densities. Future work on these systems may take the form of structure nucleation studies in the Grand Canonical ensemble to investigate the growth of particular structures; One may also treat a surface comprised of these bilayer nano-particle structures to investigate the relative stability of each topology at point where particular topologically different structures are observed at the same state point and compare this to existing thermodynamic reasoning [17]. One may also investigate the effect of switching on the second interaction site to investigate the role of slight interaction anisotropy.

Where $\alpha < 1$, $\sigma_s < \sigma_h$, self-assembled structures dominate the phase diagrams. Where $\alpha \lesssim 1$ the formation of lamellar structures dominates. Further shrinking of σ_s causes faults in the stacking of bilayer sheets and promotes the formation of curved structures with percolated voids in the moderately high density regime, which we refer to as sponge-like order. This can be considered as a contraction in the maximum contiguous bonding of successive particles. Eventually, where $\alpha \approx 0.85$, sponge-like order is suppressed in this density regime and particle assemblies adopt defined internal structures composed of strips, which we here refer to as branching networks. Lower α futher enhances the contiguous bonding restriction and promotes the formation of non-branched linear strips (around $\alpha \approx 0.775$). By $\alpha = 0.675$ the formation of continuous structures has ceased and only platelets, micellar aggregates and monomers ar observed. This trend continues until just below $\alpha = 2/3$ where solely elongate micelles are observed. By $\alpha = 0.5$ and below the presence of only roughly spherical micelles are found, which upon further reduction in α, take on small face-capped polytopes until simple prisms and other polytopes are observed nearer $\alpha = 0.25$. Again, nucleation studies may be performed here to investigate the free energy of formation of particular self-assembled structures, especially where two structures are found to coexist. Interconversion between two structures at low but finite temperatures may be slow for real systems, especially where length scales are at the high end of the meso-scale. The potential description may also be developed to incorporate continuous attractive potential energy functions.

It is suggested [4] that the enormous combinatorial space of particle anisotropy needs to be wrangled in a manner to allow a common language and taxonomy to be developed. It is quite obvious from the findings here that even very simple combinations of these anisotropy dimensions can yield very complex aggregation behaviour that varies strongly along the anisotropy parameters. To observe and develop approaches to the reliable manufacture of particle assemblies these simple relationships may be utilised as a first stop when considering where to start with a new synthesis.

Appendix A

Additional Phase Diagrams

This appendix contains additional phase diagrams referred to in the text for reference.

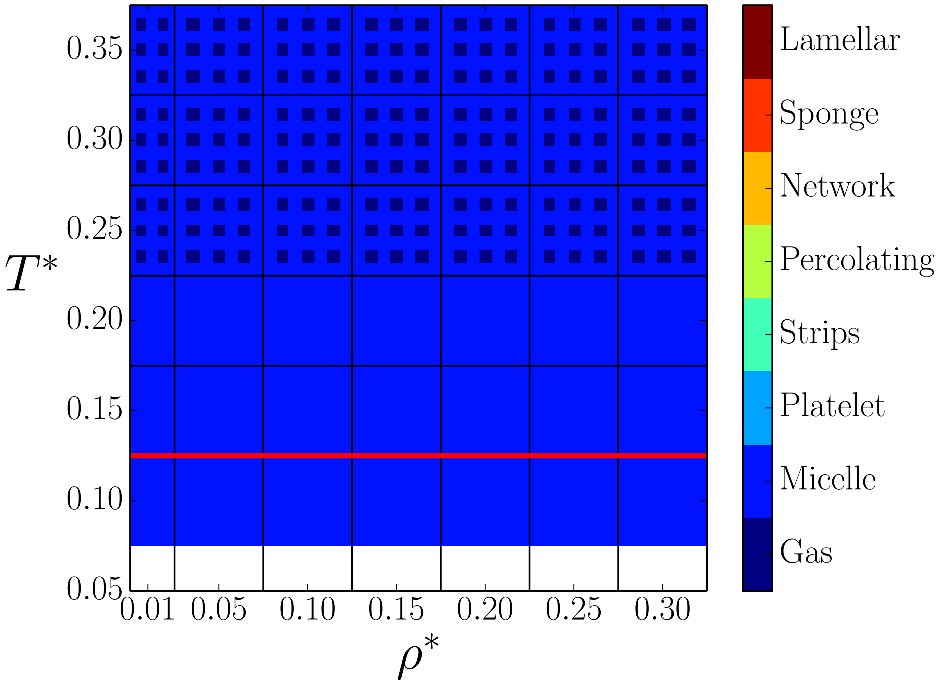

Figure A.1: Phase diagram for $\alpha = 0.5$

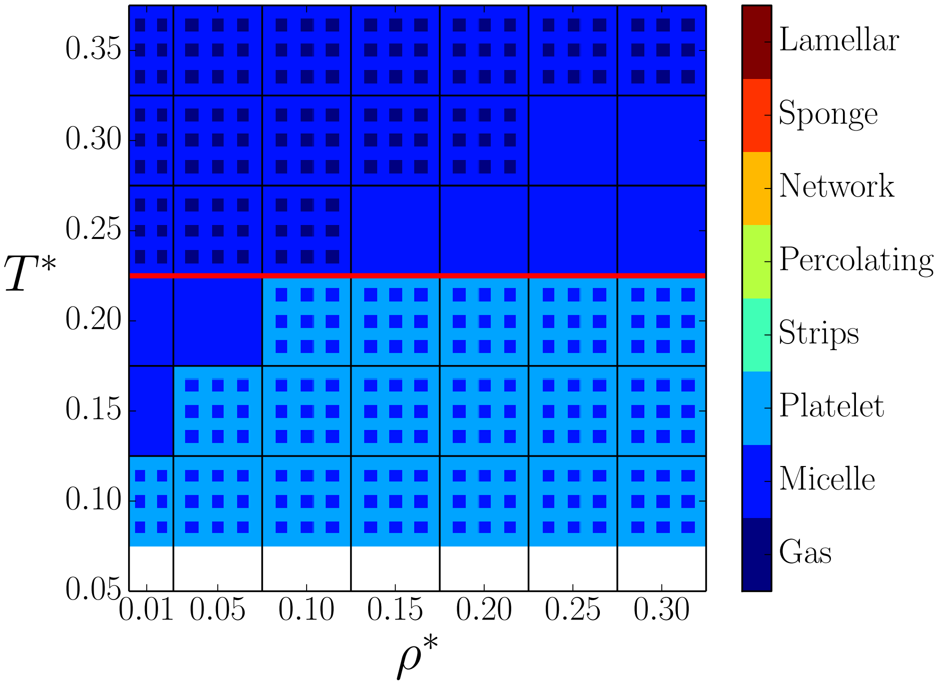

FIGURE A.2: Phase diagram for $\alpha = 0.675$

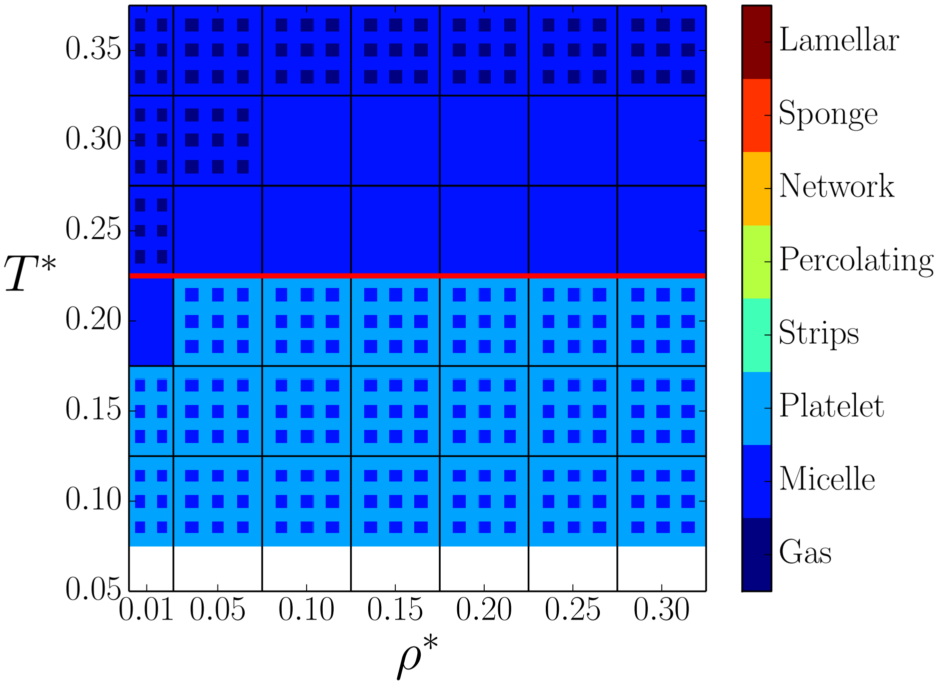

FIGURE A.3: Phase diagram for $\alpha = 0.7$

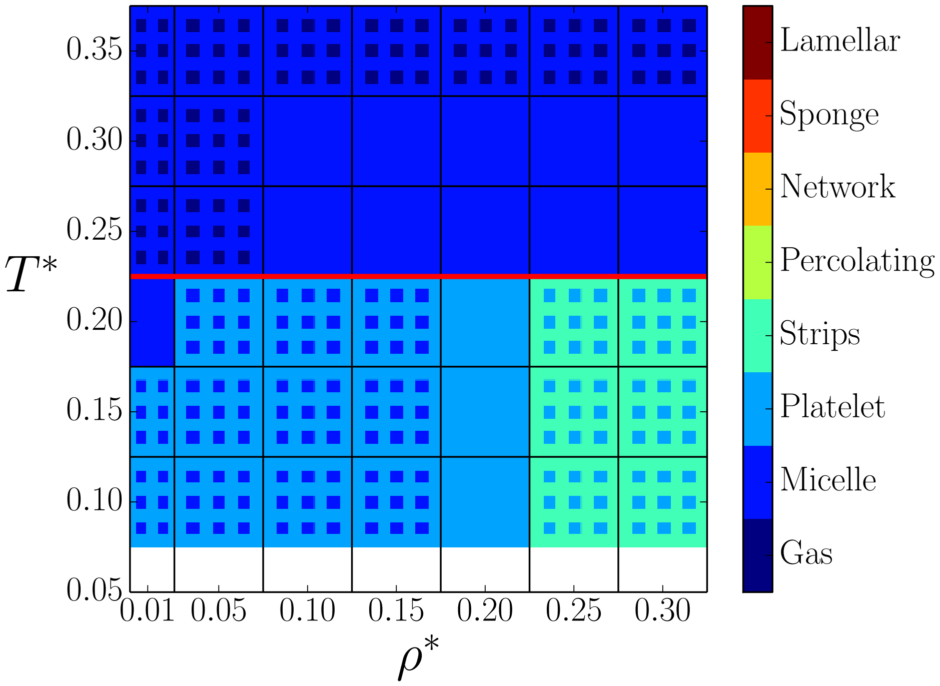

Figure A.4: Phase diagram for $\alpha = 0.725$

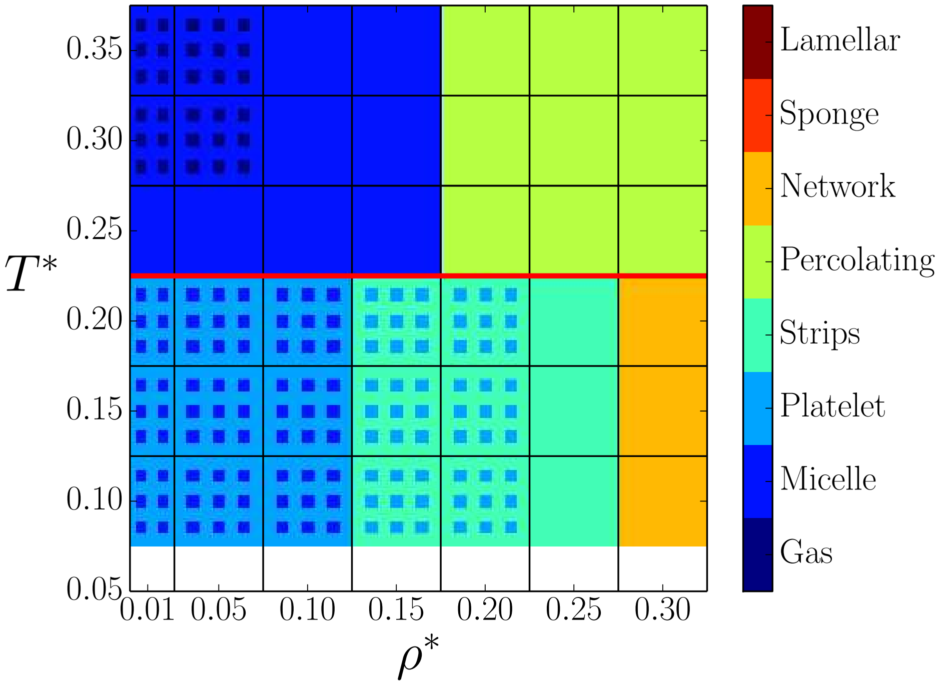

Figure A.5: Phase diagram for $\alpha = 0.775$

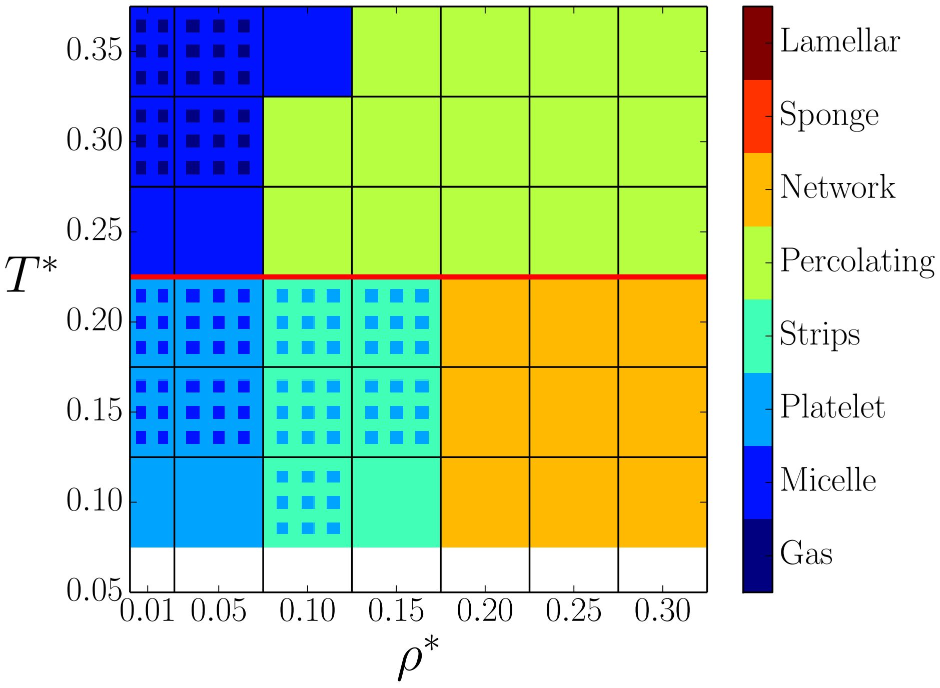

Figure A.6: Phase diagram for $\alpha = 0.825$

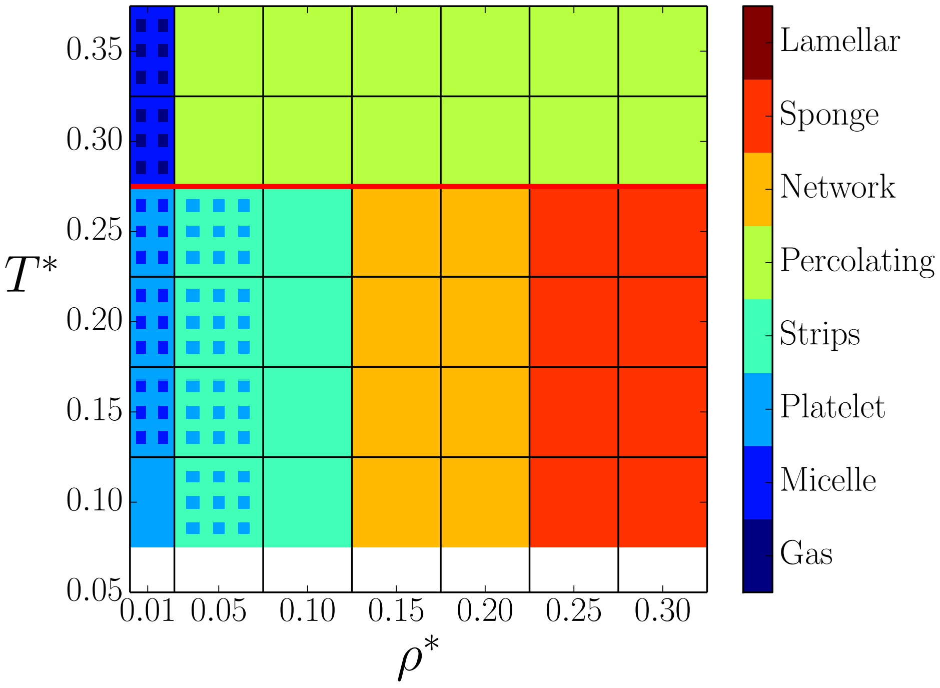

Figure A.7: Phase diagram for $\alpha = 0.875$

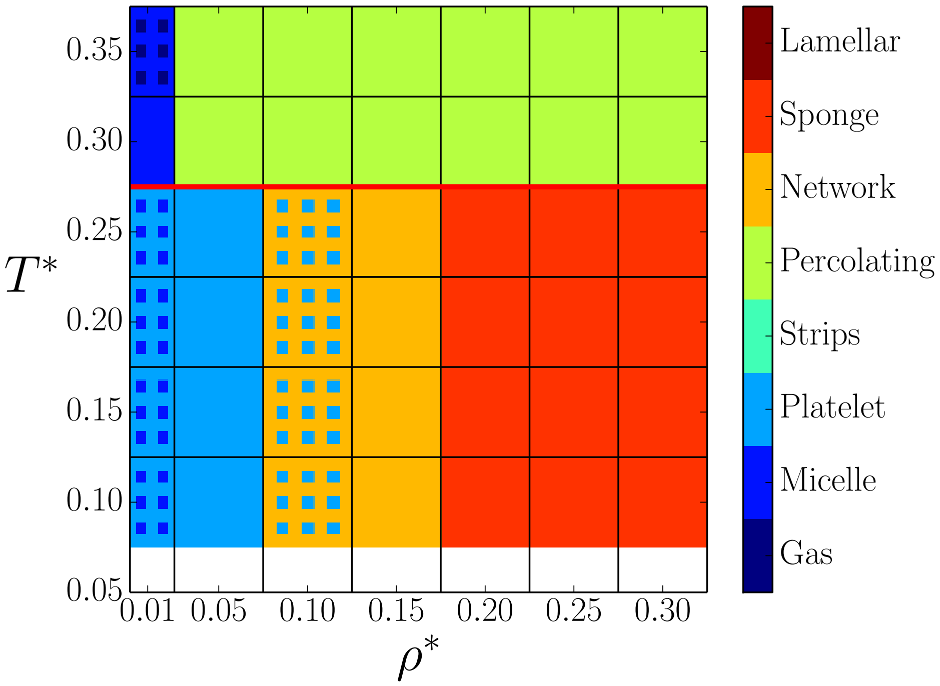

FIGURE A.8: Phase diagram for $\alpha = 0.925$

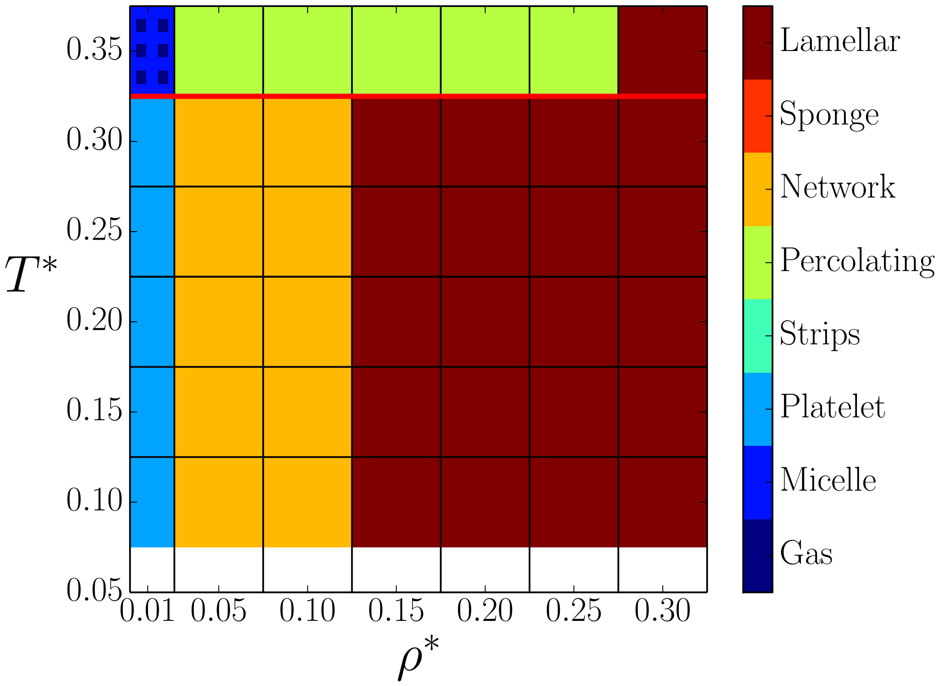

FIGURE A.9: Phase diagram for $\alpha = 0.975$

Appendix B

Self-assembly summary for $\alpha < 1$

	Structure						
α	Spherical Micelles	Elongated Micelles	Platelets	Strips	Branch Networks	Sponges	Lamellae
1/4	✓						
1/3	✓						
1/2	✓						
0.65	✓	✓					
2/3	✓	✓	✓				
0.675	✓	✓	✓				
0.7	✓	✓	✓				
0.725	✓	✓	✓	✓			
3/4	✓	✓	✓	✓			
0.775	✓	✓	✓	✓	✓		
4/5	✓	✓	✓	✓	✓		
0.825	✓	✓	✓	✓	✓		
0.85	✓	✓	✓	✓	✓		
0.875	✓	✓	✓	✓	✓	✓	
9/10	✓	✓	✓	✓	✓	✓	
0.925	✓	✓	✓		✓	✓	
0.95	✓	✓	✓		✓	✓	✓
0.975	✓	✓	✓		✓		✓

Appendix C

Distributions of q_6

It is observed for finite aggregates and continuous configurations below a certain T^* at certain α that the formation of highly structured particle environments are observed. Bond-wise rotational invariant order parameter q_6 is employed to examine the local bond orientation structure. Unfortunately, due to their complex nature, only a cursory examination was performed here. Only certain α are considered (0.75 and 1.20). $\alpha = 0.75$ was chose since it is the region with the most clear transition between micelles, platelets and strips. $\alpha = 1.2$ was chose since it is the region where both the liquid structure was analysed and simulated annealing performed on continuous bilayer structures.

C.1 $\alpha = 0.75$

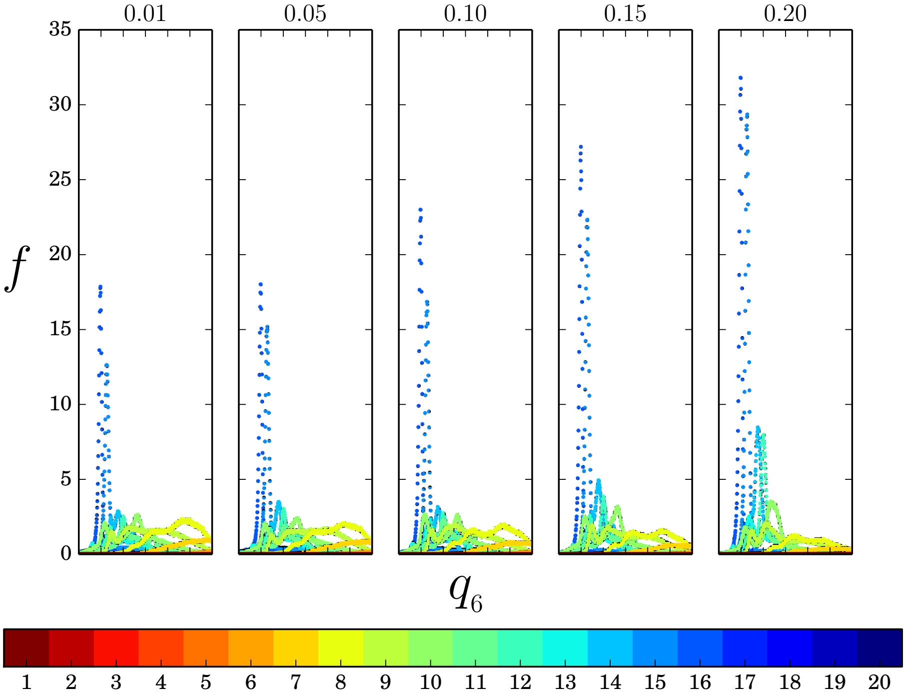

FIGURE C.1: Distributions of q_6 coloured by number of bonds - indicated in the colour bar. All x-axes are on the interval [0.2,0.5]). This region traverses the $T^* = 0.2$ isotherm, demonstrating the consistent internal bond structure of the density driven strip growing process. Clusters with disordered bond networks, such as approximately spherical and curved elongated micelles, have diffuse q_6 structure as can be observed on the leftmost distributions for $N_b \lesssim 10$. As structuring occurs these populations are depleted. The formation of the strips where a collection of $10 - 16$ coordinate particle environments grows, the number of bonds depending upon distance from the middle of the strip. Densities are indicated at the top of each distribution.

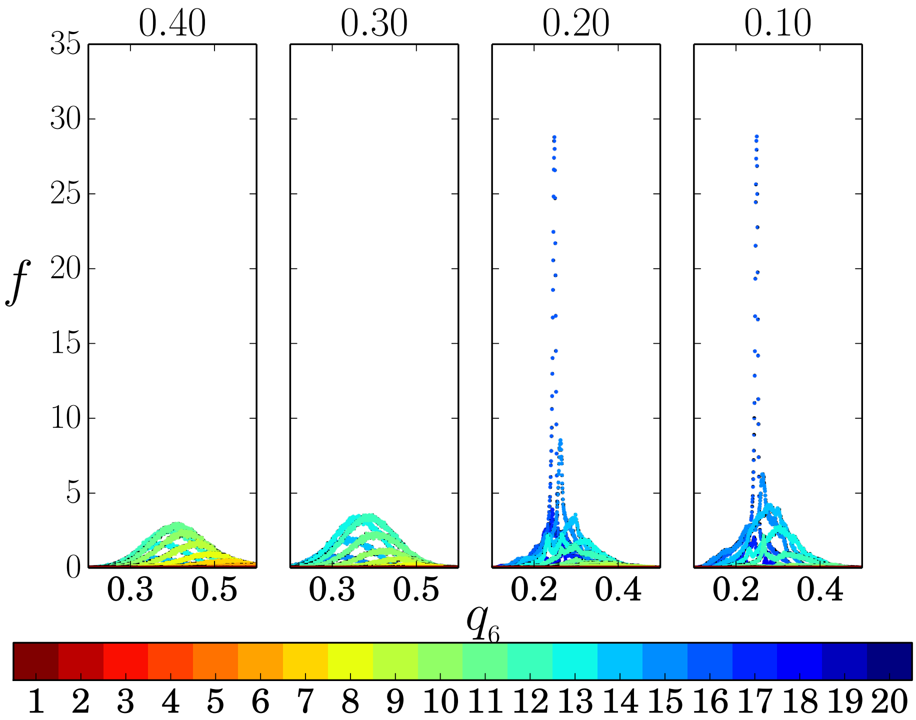

FIGURE C.2: Distributions of q_6 coloured by number of bonds - indicated in the colour bar. All x-axes are on the interval [0.2,0.6]). This region traverses the $\rho^* = 0.3$ isopycnal, demonstrating the differences in internal bond structure of the temperature driven crystallisation. Liquid bilayers with disordered bond networks have diffuse q_6 distributions. On cooling, the distributions of develop sharp peaks where the number of bonds N_b has approached 16. T^* is indicated at the top of each distribution.

Bibliography

[1] L Vega, E Demiguel, L F Rull, G Jackson, and I A McLure. Phase-Equilibria and critical behaviour of square-well fluids of variable width by Gibbs ensemble Monte Carlo Simulation. *J. Chem. Phys.*, 96(3):2296–2305, 1992. doi: 10.1063/1.462080.

[2] YN Xia and GM Whitesides. Soft lithography. *Angew. Chemie-International Ed.*, 37 (5):550–575, mar 1998. ISSN 1433-7851. doi: 10.1002/(SICI)1521-3773(19980316) 37:53.0.CO;2-G.

[3] George M Whitesides and Bartosz Grzybowski. Self-assembly at all scales. *Science*, 295(5564):2418–21, mar 2002. ISSN 1095-9203. doi: 10.1126/science.1070821.

[4] Sharon C Glotzer and Michael J Solomon. Anisotropy of building blocks and their assembly into complex structures. *Nat. Mater.*, 6(8):557–562, 2007. ISSN 1476-1122. doi: 10.1038/nmat1949.

[5] Q A Pankhurst, J Connolly, S K Jones, and J Dobson. Applications of magnetic nanoparticles in biomedicine. *J. Phys. D. Appl. Phys.*, 36(13):R167–R181, jul 2003. ISSN 0022-3727. doi: 10.1088/0022-3727/36/13/201.

[6] Verónica Salgueiriño-Maceira, M. A. Miguel a. Correa-Duarte, V Salgueirino-Maceira, and M. A. Miguel a. Correa-Duarte. Increasing the complexity of magnetic core/shell structured nanocomposites for biological applications. *Adv. Mater.*, 19 (23):4131–4144, dec 2007. ISSN 09359648. doi: 10.1002/adma.200700418.

[7] Stoyan K. Smoukov, Sumit Gangwal, Manuel Marquez, and Orlin D. Velev. Reconfigurable responsive structures assembled from magnetic Janus particles. *Soft Matter*, 5(6):1285, 2009. ISSN 1744-683X. doi: 10.1039/b814304h.

[8] Marco Lattuada and T. Alan Hatton. Preparation and controlled self-assembly of Janus magnetic nanoparticles. *J. Am. Chem. Soc.*, 129(42):12878–12889, 2007. ISSN 00027863. doi: 10.1021/ja0740521.

[9] Heng Yu, Min Chen, Philip M Rice, Shan X Wang, R L White, and Shouheng Sun. Dumbbell-like bifunctional Au-Fe3O4 nanoparticles. *Nano Lett.*, 5(2):379–82, feb 2005. ISSN 1530-6984. doi: 10.1021/nl047955q.

[10] Kai P. Yuet, Dae Kun Hwang, Ramin Haghgooie, and Patrick S. Doyle. Multifunctional superparamagnetic janus particles. *Langmuir*, 26(6):4281–7, mar 2010. ISSN 07437463. doi: 10.1021/la903348s.

[11] Jason D. Forster, Jin-Gyu Park, Manish Mittal, Heeso Noh, Carl F. Schreck, Corey S. O'Hern, Hui Cao, Eric M. Furst, and Eric R. Dufresne. Assembly of Optical-Scale Dumbbells into Dense Photonic Crystals. *ACS Nano*, 5(8):6695–6700, 2011. ISSN 1936-0851. doi: 10.1021/nn202227f.

[12] J. A. Fan, C. Wu, K. Bao, J. Bao, R. Bardhan, N. J. Halas, V. N. Manoharan, P. Nordlander, G. Shvets, and F. Capasso. Self-Assembled Plasmonic Nanoparticle Clusters_SI. *Science*, 328(5982):1135–1138, 2010. ISSN 0036-8075. doi: 10.1126/science.1187949.

[13] S.J J Oldenburg, R.D D Averitt, S.L L Westcott, and N.J J Halas. Nanoengineering of optical resonances. *Chem. Phys. Lett.*, 288(2-4):243–247, 1998. ISSN 00092614. doi: 10.1016/s0009-2614(98)00277-2.

[14] Rui Hao, Ruijun Xing, Zhichuan Xu, Yanglong Hou, Song Gao, and Shouheng Sun. Synthesis, functionalization, and biomedical applications of multifunctional magnetic nanoparticles. *Adv. Mater.*, 22(25):2729–42, jul 2010. ISSN 1521-4095. doi: 10.1002/adma.201000260.

[15] Bum Jun Park and Daeyeon Lee. Equilibrium orientation of nonspherical Janus particles at fluid–fluid interfaces. *ACS Nano*, 6(1):782–790, 2011. ISSN 1936-086X. doi: 10.1021/nn204261w.

[16] A Nicholls, K A Sharp, and B Honig. Protein folding and association: insights from the interfacial and thermodynamic properties of hydrocarbons. *Proteins*, 11 (4):281–96, jan 1991. ISSN 0887-3585. doi: 10.1002/prot.340110407.

[17] Jacob N. Israelachvili, D. John Mitchell, and Barry W. Ninham. Theory of self-assembly of hydrocarbon amphiphiles into micelles and bilayers. *J. Chem. Soc. Faraday Trans. 2*, 72:1525, 1976. ISSN 0300-9238. doi: 10.1039/f29767201525.

[18] Miho Yanagisawa, Naofumi Shimokawa, Masatoshi Ichikawa, and Kenichi Yoshikawa. Micro-segregation induced by bulky-head lipids: formation of characteristic patterns in a giant vesicle. *Soft Matter*, 8(2):488–495, dec 2012. ISSN 1744-683X. doi: 10.1039/C1SM06381B.

[19] David A Zacharias, Jonathan D Violin, Alexandra C Newton, and Roger Y Tsien. Partitioning of lipid-modified monomeric GFPs into membrane microdomains of live cells. *Science*, 296(5569):913–6, may 2002. ISSN 1095-9203. doi: 10.1126/science.1068539.

[20] C Casagrande, P Fabre, E Raphaël, and M Veyssié. "Janus Beads": Realization and Behaviour at Water/Oil Interfaces. *Europhys. Lett.*, 9(3):251–255, jun 1989. ISSN 0295-5075. doi: 10.1209/0295-5075/9/3/011.

[21] Fuquan Tu, Bum Jun Park, and Daeyeon Lee. Thermodynamically stable emulsions using Janus dumbbells as colloid surfactants. *Langmuir*, 29(41):12679–12687, 2013. ISSN 07437463. doi: 10.1021/la402897d.

[22] Andreas Walther, A H E Muller, Axel H E Müller, and A H E Muller. Janus Particles: Synthesis, Self-Assembly, Physical Properties, and Applications. *Chem. Rev.*, 113(7):5194–5261, jul 2013. ISSN 1520-6890. doi: 10.1021/cr300089t.

[23] Jing Hu, Shuxue Zhou, Yangyi Sun, Xiaosheng Fang, and Limin Wu. Fabrication, properties and applications of Janus particles. *Chem. Soc. Rev.*, 41(11):4356, jun 2012. ISSN 0306-0012. doi: 10.1039/c2cs35032g.

[24] Liang Hong, Angelo Cacciuto, Erik Luijten, and Steve Granick. Clusters of amphiphilic colloidal spheres. *Langmuir*, 24(3):621–625, 2008. ISSN 07437463. doi: 10.1021/la7030818.

[25] Liang Hong, Shan Jiang, and Steve Granick. Simple method to produce Janus colloidal particles in large quantity. *Langmuir*, 22(23):9495–9499, 2006. ISSN 07437463. doi: 10.1021/la062716z.

[26] Shan Jiang and Steve Granick. Controlling the Geometry (Janus Balance) of Amphiphilic Colloidal Particles Controlling the Geometry (Janus Balance) of Amphiphilic Colloidal Particles. *Society*, 24(February):2438–2445, 2008. ISSN 0743-7463. doi: 10.1021/la703274a.

[27] Hong-Ren Ren Jiang, Natsuhiko Yoshinaga, and Masaki Sano. Active Motion of a Janus Particle by Self-Thermophoresis in a Defocused Laser Beam. *Phys. Rev. Lett.*, 105(26):4, 2010. ISSN 00319007. doi: 10.1103/PhysRevLett.105.268302.

[28] Shan Jiang, Qian Chen, Mukta Tripathy, Erik Luijten, Kenneth S. Schweizer, and Steve Granick. Janus Particle Synthesis and Assembly. *Adv. Mater.*, 22(10):1060–1071, 2010. ISSN 09359648. doi: 10.1002/adma.200904094.

[29] Francesco Sciortino, Achille Giacometti, and Giorgio Pastore. Phase Diagram of Janus Particles. *Phys. Rev. Lett.*, 103(23):4, 2009. ISSN 0031-9007. doi: 10.1103/PhysRevLett.103.237801.

[30] Gianmarco Munao, Zdenek Preisler, Teun Vissers, Frank Smallenburg, Francesco Sciortino, Gianmarco Munaò, Zdenek Preisler, Teun Vissers, Frank Smallenburg, and Francesco Sciortino. Cluster formation in one-patch colloids: low

coverage results. *Soft Matter*, 9(9):2652–2661, 2013. ISSN 1744-683X. doi: 10.1039/c2sm27490f.

[31] William L. Miller and Angelo Cacciuto. Hierarchical self-assembly of asymmetric amphiphatic spherical colloidal particles. *Phys. Rev. E.*, 80(2):021404, 2009. ISSN 1539-3755. doi: 10.1103/PhysRevE.80.021404.

[32] Riccardo Fantoni, Achille Giacometti, Francesco Sciortino, and Giorgio Pastore. Cluster theory of Janus particles. *Soft Matter*, 7(6):20, mar 2010. ISSN 1744-683X. doi: 10.1039/c0sm009954.

[33] Achille Giacometti, Christoph Gögelein, Fred Lado, Francesco Sciortino, Silvano Ferrari, and Giorgio Pastore. From square-well to Janus: improved algorithm for integral equation theory and comparison with thermodynamic perturbation theory within the Kern-Frenkel model. *J. Chem. Phys.*, 140(9):094104, mar 2014. ISSN 1089-7690. doi: 10.1063/1.4866899.

[34] Qian Chen, Jonathan K Whitmer, Shan Jiang, Sung Chul Bae, Erik Luijten, and Steve Granick. Supracolloidal reaction kinetics of Janus spheres. *Science*, 331(6014): 199–202, 2011. ISSN 0036-8075. doi: 10.1126/science.1197451.

[35] Francesco Sciortino, Achille Giacometti, and Giorgio Pastore. A numerical study of one-patch colloidal particles: from square-well to Janus. *Phys. Chem. Chem. Phys.*, 12(38):11869–11877, oct 2010. ISSN 1463-9084. doi: 10.1039/c0cp00504e.

[36] Norbert Kern and Daan Frenkel. Fluid–fluid coexistence in colloidal systems with short-ranged strongly directional attraction. *J. Chem. Phys.*, 118(21):9882, may 2003. ISSN 00219606. doi: 10.1063/1.1569473.

[37] P. G. de Gennes. Soft matter. *Rev. Mod. Phys.*, 64(3):645–648, jul 1992. ISSN 0034-6861. doi: 10.1103/RevModPhys.64.645.

[38] Jin Woong Kim, Ryan J Larsen, and David a Weitz. Synthesis of nonspherical colloidal particles with anisotropic properties. *J. Am. Chem. Soc.*, 128(44):14374–14377, 2006. ISSN 00027863. doi: 10.1021/ja065032m.

[39] Eunji Lee, Young-Hwan Hwan Jeong, Jung-Keun Keun Kim, and Myongsoo Lee. Controlled self-assembly of asymmetric dumbbell-shaped rod amphiphiles: Transition from toroids to planar nets. *Macromolecules*, 40(23):8355–8360, 2007. ISSN 00249297. doi: 10.1021/ma071511.

[40] Jin-Woong W Kim, Daeyeon Lee, Ho Cheung Shum, and David A. Weitz. Colloid surfactants for emulsion stabilization. *Adv. Mater.*, 20(17):3239–+, 2008. ISSN 09359648. doi: 10.1002/adma.200800484.

[41] Panagiotis E Theodorakis, Wolfgang Paul, and Kurt Binder. Interplay between Chain Collapse and Microphase Separation in Bottle-Brush Polymers with Two Types of Side Chains. *Macromolecules*, 43(11):5137–5148, 2010. doi: 10.1021/ma100414u.

[42] Qinhui Chen, Qingqin Li, and Jinhuo Lin. Synthesis of Janus composite particles by the template of dumbbell-like silica/polystyrene. *Mater. Chem. Phys.*, 128(3):377–382, 2011. ISSN 02540584. doi: 10.1016/j.matchemphys.2011.03.009.

[43] Daisuke Nagao, Kanako Goto, Haruyuki Ishii, and Mikio Konno. Preparation of Asymmetrically Nanoparticle-Supported, Monodisperse Composite Dumbbells by Protruding a Smooth Polymer Bulge from Rugged Spheres. *Langmuir*, 27(21):13302–13307, 2011. ISSN 1520-5827. doi: 10.1021/la202968f.

[44] Daisuke Nagao, Maki Sugimoto, Ayako Okada, Haruyuki Ishii, Mikio Konno, Arnout Imhof, and Alfons Van Blaaderen. Directed Orientation of Asymmetric Composite Dumbbells by Electric Field Induced Assembly. *Langmuir*, 28(16):6546–6550, 2012. ISSN 07437463. doi: 10.1021/la204493m.

[45] Julien Parvole, Isabelle Chaduc, Komla Ako, Olivier Spalla, Antoine Thill, Serge Ravaine, Etienne Duguet, Muriel Lansalot, and Elodie Bourgeat-Lami. Efficient Synthesis of Snowman- and Dumbbell-like Silica/Polymer Anisotropic Heterodimers through Emulsion Polymerization Using a Surface-Anchored Cationic Initiator. *Macromolecules*, 45(17):7009–7018, 2012. ISSN 00249297. doi: 10.1021/ma301355g.

[46] Gopi Krishnan, Marcel A Verheijen, Gert H ten Brink, George Palasantzas, and Bart J Kooi. Tuning structural motifs and alloying of bulk immiscible Mo-Cu bimetallic nanoparticles by gas-phase synthesis. *Nanoscale*, 5(12):5375–5383, 2013. ISSN 2040-3372. doi: 10.1039/c3nr00565h.

[47] Bas G P van Ravensteijn, Marlous Kamp, Alfons van Blaaderen, and Willem K Kegel. General Route toward Chemically Anisotropic Colloids. *Chem. Mater.*, 25 (21):4348–4353, 2013. doi: 10.1021/cm4025606.

[48] Jingxia Wang, Liang Hu, Yanlin Song, and Michael J Serpe. Non-spherical Janus microgels driven by thiolated DNA interactions. *Polymer (Guildf).*, 55(10):2340–2346, 2014. doi: 10.1016/j.polymer.2014.03.043.

[49] Lucio Isa, Niveditha Samudrala, and Eric R Dufresne. Adsorption of sub-micron amphiphilic dumbbells to fluid interfaces. *Langmuir*, 30(18):5057–5063, 2014. ISSN 1520-5827. doi: 10.1021/la500463m.

[50] Fangfang Chu, Frank Polzer, Nikolai Severin, Yan Lu, Andreas Ott, Juergen P Jürgen P. Rabe, and Matthias Ballauff. Thermosensitive hollow Janus dumbbells. *Colloid Polym. Sci.*, 292(8):1785–1793, 2014. ISSN 14351536. doi: 10.1007/s00396-014-3287-8.

[51] Binh T T Pham, Chris H Such, and Brian S Hawkett. Synthesis of polymeric janus nanoparticles and their application in surfactant-free emulsion polymerizations. *Polym. Chem.*, 6(3):426–435, 2015. ISSN 1759-9954. doi: 10.1039/c4py01125b.

[52] Joost R Wolters, Guido Avvisati, Fabian Hagemans, Teun Vissers, Daniela J Kraft, Marjolein Dijkstra, and Willem K Kegel. Self-assembly of "Mickey Mouse" shaped colloids into tube-like structures: experiments and simulations. *Soft Matter*, 11(6): 1067–1077, 2015. doi: 10.1039/c4sm02375g.

[53] Gianmarco Munao, Dino Costa, Achille Giacometti, Carlo Caccamo, and Francesco Sciortino. Structure and phase behavior of colloidal dumbbells with tunable attractive interactions. *Phys. Chem. Chem. Phys.*, 15(47):20590–20599, 2013. ISSN 1463-9076. doi: 10.1039/c3cp52425f.

[54] Stephen Whitelam and Stefan A F Bon. Self-assembly of amphiphilic peanut-shaped nanoparticles. *J. Chem. Phys.*, 132(7):074901, mar 2010. ISSN 1089-7690. doi: 10.1063/1.3316794.

[55] Guido Avvisati, Teun Vissers, and Marjolein Dijkstra. Self-assembly of patchy colloidal dumbbells. *J. Chem. Phys.*, 142(8):84905, 2015. ISSN 0021-9606. doi: 10.1063/1.4913369.

[56] S Whitelam and P L Geissler. Avoiding unphysical kinetic traps in Monte Carlo simulations of strongly attractive particles. *J. Chem. Phys.*, 127(15):19, 2007. doi: 10.1063/1.2790421.

[57] Gianmarco Munaò, Patrick O'Toole, Toby S Hudson, Dino Costa, Carlo Caccamo, Achille Giacometti, and Francesco Sciortino. Phase separation and self-assembly of colloidal dimers with tunable attractive strength: from symmetrical square-wells to Janus dumbbells. *Soft Matter*, 10(29):5269–79, aug 2014. ISSN 1744-6848. doi: 10.1039/c4sm00544a.

[58] Xuan-Cuong Luu and Alberto Striolo. Ellipsoidal janus nanoparticles assembled at spherical oil/water interfaces. *The Journal of Physical Chemistry B*, 118(47): 13737–13743, 2014. doi: 10.1021/jp5085422. PMID: 25358124.

[59] Teun Vissers, Zdenek Preisler, Frank Smallenburg, Marjolein Dijkstra, and Francesco Sciortino. Predicting crystals of Janus colloids. *J. Chem. Phys.*, 138 (16), 2013. doi: 10.1063/1.4801438.

[60] B. J. Alder and T. E. Wainwright. Phase transition for a hard sphere system. *The Journal of Chemical Physics*, 27(5), 1957.

[61] A. D. Bruce, A. N. Jackson, G. J. Ackland, and N. B. Wilding. Lattice-switch monte carlo method. *Phys. Rev. E*, 61:906–919, Jan 2000. doi: 10.1103/PhysRevE.61.906.

[62] J. L. Finney. Random packings and the structure of simple liquids. i. the geometry of random close packing. *Proceedings of the Royal Society of London A: Mathematical, Physical and Engineering Sciences*, 319(1539):479–493, 1970. ISSN 0080-4630. doi: 10.1098/rspa.1970.0189.

[63] D. M. Heyes and P. J. Aston. Square-well and square-shoulder fluids: Simulation and equations of state. *J. Chem. Phys.*, 97(8):5738, 1992. ISSN 00219606. doi: 10.1063/1.463758.

[64] M Lisal and I Nezbeda. Pure fluids of homonuclear and heteronuclear square-well diatomics I. Computer simulation study. *Mol. Phys.*, 96(3):335, 1999. ISSN 0026-8976. doi: 10.1080/002689799165648.

[65] Fernando Del Río, Edgar Ávalos, Rodolfo Espíndola, Luis F. Rull, George Jackson, and Santiago Lago. Vapour—liquid equilibrium of the square-well fluid of variable range via a hybrid simulation approach. *Mol. Phys.*, 100(15):2531–2546, 2002. ISSN 0026-8976. doi: 10.1080/00268970210132522.

[66] Bin Chen and J. Ilja Siepmann. A Novel Monte Carlo Algorithm for Simulating Strongly Associating Fluids: Applications to Water, Hydrogen Fluoride, and Acetic Acid. *J. Phys. Chem. B*, 104(36):8725–8734, sep 2000. ISSN 1520-6106. doi: 10.1021/jp001952u.

[67] Bin Chen and J. Ilja Siepmann. Improving the Efficiency of the Aggregation-Volume-Bias Monte Carlo Algorithm. *J. Phys. Chem. B*, 105(45):11275–11282, nov 2001. ISSN 1520-6106. doi: 10.1021/jp012209k.

[68] Daan Frenkel and Berend Smit. Understanding Molecular Simulation: From Algorithms to Applications. *Comput. Sci. Ser.*, 1:443, 1996.

[69] Phil Attard. On the density of volume states in the isobaric ensemble. *J. Chem. Phys.*, 103(22), 1995.

[70] Nicholas Metropolis, Arianna W. Rosenbluth, Marshall N. Rosenbluth, Augusta H. Teller, and Edward Teller. Equation of State Calculations by Fast Computing Machines. *J. Chem. Phys.*, 21(6):1087–1092, 1953. ISSN 00219606. doi: doi: 10.1063/1.1699114.

[71] Makoto Matsumoto and Takuji Nishimura. Mersenne twister: a 623-dimensionally equidistributed uniform pseudo-random number generator. *ACM Trans. Model. Comput. Simul.*, 8(1):3–30, jan 1998. ISSN 10493301. doi: 10.1145/272991.272995.

[72] Lorenzo Rovigatti, John Russo, and Francesco Sciortino. Structural properties of the dipolar hard-sphere fluid at low temperatures and densities. *Soft Matter*, 8: 6310–6319, 2012. doi: 10.1039/C2SM25192B.

[73] T D Loeffler, A Sepehri, and B Chen. Improved Monte Carlo Scheme for Efficient Particle Transfer in Heterogeneous Systems in the Grand Canonical Ensemble: Application to Vapor-Liquid Nucleation. *J. Chem. Theory Comput.*, 11(9):4023–4032, 2015.

[74] S Kirkpatrick. Optimization by simulated annealing: Quantitative studies. *J. Stat. Phys.*, 34(5-6):975–986, mar 1984. ISSN 0022-4715. doi: 10.1007/BF01009452.

[75] S Kirkpatrick, C D Gelatt, and M P Vecchi. Optimization by Simulated Annealing. *Science*, 220(4598):pp. 671—-680, 1983. ISSN 00368075. doi: 10.1126/science.220.4598.671.

[76] G.M. Torrie and J.P. Valleau. Nonphysical sampling distributions in Monte Carlo free-energy estimation: Umbrella sampling. *J. Comput. Phys.*, 23(2):187–199, 1977. ISSN 00219991. doi: 10.1016/0021-9991(77)90121-8.

[77] P Virnau and M Mueller. Successive Umbrella Sampling. *Condens. Matter*, page 4, 2003.

[78] P Virnau and M Muller. Calculation of free energy through successive umbrella sampling. *J. Chem. Phys.*, 120(23):10925–10930, 2004. doi: 10.1063/1.1739216.

[79] Linge Bai and David Breen. Calculating Center of Mass in an Unbounded 2D Environment. *J. Graph. GPU, Game Tools*, 13(4):53–60, jan 2008. ISSN 2151-237X. doi: 10.1080/2151237X.2008.10129266.

[80] G Munaò, P O'Toole, T S Hudson, D Costa, C Caccamo, F Sciortino, and A Giacometti. Cluster formation and phase separation in heteronuclear Janus dumbbells. *J. Phys. Condens. Matter*, 27(23):234101, jun 2015. ISSN 0953-8984. doi: 10.1088/0953-8984/27/23/234101.

[81] A Stradner, H Sedgwick, F Cardinaux, W C K Poon, S U Egelhaaf, and P Schurtenberger. Equilibrium cluster formation in concentrated protein solutions and colloids. *Nature*, 432(7016):492–495, 2004. doi: 10.1038/nature03109.

[82] Yun Liu, Emiliano Fratini, Piero Baglioni, Wei Ren Chen, and Sow Hsin Chen. Effective long-range attraction between protein molecules in solutions studied by small angle neutron scattering - art. no. 118402. *Phys. Rev. Lett.*, 95(11):2–5, 2005. ISSN 00319007. doi: 10.1103/PhysRevLett.95.118102.

[83] F Cardinaux, A Stradner, P Schurtenberger, F Sciortino, and E Zaccarelli. Modeling equilibrium clusters in lysozyme solutions. *Europhys. Lett.*, 77(4):48004, 2007. ISSN 0295-5075. doi: 10.1209/0295-5075/77/48004.

[84] Jean-Marc Bomont, Jean-Louis Bretonnet, and Dino Costa. Temperature study of cluster formation in two-Yukawa fluids. *J. Chem. Phys.*, 132(18):184508, may 2010. ISSN 00219606. doi: 10.1063/1.3418609.

[85] Jean-Marc Bomont, Jean-Louis Bretonnet, Dino Costa, and Jean-Pierre Hansen. Communication: thermodynamic signatures of cluster formation in fluids with competing interactions. *J. Chem. Phys.*, 137(1):11101, 2012. ISSN 1089-7690. doi: 10.1063/1.4733390.

[86] A Yethiraj and C K Hall. Square-well diatomics-bulk equation of state, density profiles near wals, virial coefficients and coexistence properties. *Mol. Phys.*, 72(3): 619–641, feb 1991. ISSN 0026-8976. doi: 10.1080/00268979100100471.

[87] Kurt Binder, Benjamin J. Block, Peter Virnau, and Andreas Tröster. Beyond the van der waals loop: What can be learned from simulating lennard-jones fluids inside the region of phase coexistence. *American Journal of Physics*, 80(12), 2012.

[88] J. M. Seddon and R. H. Templer. Cubic Phases of Self-Assembled Amphiphilic Aggregates. *Philos. Trans. R. Soc. A Math. Phys. Eng. Sci.*, 344(1672):377–401, aug 1993. ISSN 1364-503X. doi: 10.1098/rsta.1993.0096.

[89] M. W. Matsen and F. S. Bates. Block copolymer microstructures in the intermediate-segregation regime. *J. Chem. Phys.*, 106(6):2436, feb 1997. ISSN 00219606. doi: 10.1063/1.473153.

[90] Aaron S. Keys, Christopher R. Iacovella, and Sharon C. Glotzer. Characterizing complex particle morphologies through shape matching: Descriptors, applications, and algorithms. *J. Comput. Phys.*, 230(17):6438–6463, 2011. ISSN 00219991. doi: 10.1016/j.jcp.2011.04.017.

[91] F Wurm and A F M Kilbinger. Polymeric Janus Particles. *Angew. Chemie-International Ed.*, 48(45):8412–8421, 2009. doi: 10.1002/anie.200901735.

[92] Andela Šaric, Behnaz Bozorgui, Angelo Cacciuto, Andela Saric, Behnaz Bozorgui, and Angelo Cacciuto. Packing of Soft Asymmetric Dumbbells. *J. Phys. Chem. B*, 115(22):7182–7189, 2011. ISSN 15206106. doi: 10.1021/jp107545w.